

# **Numerical Analysis of High-speed Droplet Impingement on Elastic and Rigid Substrates**

Mason Marzbali

A Thesis

In the Department

of

Mechanical, Industrial and Aerospace Engineering

Presented in Partial Fulfillment of the Requirements

For the Degree of

Doctor of Philosophy (Mechanical Engineering) at

Concordia University

Montreal, Quebec, Canada

August 2017

© Mason Marzbali, 2017

**CONCORDIA UNIVERSITY  
SCHOOL OF GRADUATE STUDIES**

This is to certify that the thesis prepared

By: **Mason Marzbali**

Entitled: **Numerical Analysis of High-speed Droplet Impingement on Elastic and Rigid Substrates**

and submitted in partial fulfillment of the requirements for the degree of

**DOCTOR OF PHILOSOPHY (Mechanical Engineering)**

complies with the regulations of the University and meets the accepted standards with respect to originality and quality.

Signed by the final Examining Committee:

\_\_\_\_\_ Chair  
Dr. Mojtaba Kahrizi

\_\_\_\_\_ External Examiner  
Dr. Nasser Ashgriz

\_\_\_\_\_ External to Program  
Dr. Atila Zsaki

\_\_\_\_\_ Examiner  
Dr. Marius Paraschivoiu

\_\_\_\_\_ Examiner  
Dr. Ramin Sedaghati

\_\_\_\_\_ Thesis Supervisor  
Dr. Ali Dolatabadi

Approved by \_\_\_\_\_  
Dr. Ali Dolatabadi, Graduate Program Director

2017-08-24 \_\_\_\_\_  
Dr. Amir Asif, Dean,  
Faculty of Engineering and Computer Science

# ABSTRACT

## Numerical Analysis of High-speed Droplet Impingement on Elastic and Rigid Substrates

Mason Marzbali, PhD  
Concordia University, 2017

**H**igh-speed droplet impact is of great interest to power generation and aerospace industries due to the accrued cost of maintenance in steam and gas turbines. The repetitive impacts of liquid droplets onto rotor blades, at high relative velocities, result in the blade erosion, which is known as Liquid Impingement Erosion (LIE). Experimental and analytical studies in this field are limited due to the complexity of the droplet impact at such conditions. Hence, numerical analysis is a very powerful and affordable tool to investigate LIE phenomenon. In this regard, it is crucial to understand the hydrodynamics of the impact in order to identify the consequent solid response before addressing the LIE problem. A 3D analysis of the droplet impingement allows to obtain the transient pressure generated in the liquid and resolve the stress field in the solid material. Knowing the transient behavior of the substrate, in response to pressure force exerted due to the impact, would facilitate engineering new types of surface coatings that are more resistant to LIE. To that end, modeling the impact of liquid droplets, at high velocities, on elastic and rigid solid substrates, is the main objective of the present work. In order to model the interfacial flow in the fluid region, which contains liquid and gas phases, Volume of Fluid (VOF) method is utilized. The droplet deformation is precisely captured upon impact with impingement velocities from 50 up to 500 m/s. An incompressible

solver is implemented for impact velocities below 100 m/s and a compressible model is used at higher impingement velocities. In addition, the stress field in the solid substrate is modeled with Finite Element Method (FEM). A novel 3D model for Fluid-Solid Interaction (FSI) that couples the gas-liquid interfacial model with the structural solver is implemented. The coupling between the fluid and solid domains is achieved by imposing the stress continuity and no-slip velocity condition on the fluid-solid interface. The pressure history in the fluid domain and the transient stress field in the solid domain are obtained simultaneously, by solving the coupled fluid and solid equations with a two-way coupling approach. The validation of the two-way-coupled FSI solver is carried out with ANSYS Workbench. Furthermore, the effect of the fluid compressibility on the generated pressure build-up in the liquid and the resulting stress in the solid are investigated. The results obtained from the compressible fluid modeling are validated against the numerical studies and analytical correlations, available in open literature. Finally, the FEM modeling results for an isotropic Titanium alloy, namely Ti-6Al-4V, widely utilized in manufacturing of gas turbine components, are presented and its elastic deformation threshold is examined. The results obtained in the present work reveal that the substrate reaches its tensile yield strength, under an impact scenario that is known to be destructive in LIE applications, which eventually may lead to micro-crack initiation in the solid material.

## Acknowledgements

I would like to express my best gratitude toward my academic advisor and friend, Dr. Ali Dolatabadi for his constant support and guidance during my PhD program. The technical support provided by Dr. Mamoun Medraj in Mechanical and Industrial Engineering Department is greatly acknowledged. I would like to thank Dr. Pawel Jedrzejowski from Siemens Canada and Alexandre Gariépy from École de Technologie Supérieure (ETS) for their useful comments and technical input. The feedback from Reza Attarzadeh and Siavash G. Azar are greatly appreciated.

The present work was funded by *Siemens Canada (formerly Rolls-Royce Canada)*, *Consortium de Recherche et d'Innovation en Aérospatiale au Québec (CRIAQ)*, *Natural Sciences and Engineering Research Council of Canada (NSERC)*, *Le Fonds Québécois de la Recherche sur la Nature et les Technologies (FQRNT)*, *Nano-Quebec* and *Hydro Quebec*.

*- To my eternal love and life partner -*

*“Everything in the universe is within you. Ask all from yourself.”*

*~ Rumi ~*

# Table of Contents

List of Figures .....	xi
List of Tables .....	xvi
Nomenclature .....	xvii
1. Introduction.....	1
1.1 Background .....	2
1.2 Liquid Impingement Erosion (LIE).....	8
1.3 Motivation.....	13
1.4 Literature review.....	18
1.4.1 High-speed droplet impingement.....	19
1.4.2 Fluid-Solid Interaction (FSI).....	23
1.5 Objectives .....	27
1.6 Thesis outline.....	29
2. Incompressible droplet impact.....	30
2.1 Methodology .....	31
2.1.1 Incompressible fluid equations .....	31
2.1.2 Volume of Fluid Model .....	33
2.1.3 Elastic solid equations .....	35

2.1.4	Fluid-Solid Coupling .....	36
2.1.5	Computational domain and material properties .....	39
2.1.6	Boundary and initial conditions .....	40
2.1.7	Numerical schemes and discretization .....	41
2.2	Results and discussion.....	43
2.2.1	Incompressible impact on rigid substrates .....	44
2.2.2	Incompressible impact on elastic substrates .....	53
2.2.3	Validation with ANSYS Workbench .....	54
2.2.4	Solid elasticity effect .....	56
2.2.5	Fluid compressibility effect.....	57
3.	Compressible droplet impact .....	60
3.1	Methodology.....	61
3.1.1	Compressible fluid equations.....	62
3.1.2	Computational domain and material properties .....	64
3.1.3	Boundary and initial conditions .....	66
3.1.4	Numerical schemes and discretization .....	66
3.2	Results and discussion.....	67
3.2.1	Single droplet impingement at a normal angle .....	80
3.2.2	Single droplet impingement at oblique angles .....	84
3.2.3	Droplet impact onto liquid films.....	86

3.3	Finite Element Model of an elastic solid substrate.....	93
4.	Closure .....	101
4.1	Summary .....	101
4.2	Conclusions.....	102
4.3	Challenges and limitations .....	104
4.4	Future work .....	105
	Bibliography.....	106
	Appendices .....	111
I.	Grid sensitivity analysis .....	111
II.	Droplet impact onto liquid films, extension .....	112

# List of Figures

Figure 1-1: Trent 60 Wet Low Emissions (WLE) nominal performance, photo courtesy: Siemens. .....	2
Figure 1-2: Industrial Trent 60 gas turbine with Rolls-Royce aero-engine technology test facility in Montreal, Canada, photo courtesy: Siemens. ....	3
Figure 1-3: Sprint <sup>®</sup> Spray Intercooling system, photo courtesy: GE. ....	4
Figure 1-4: AFM images of (a) original polished surface of TiAl, (b) eroded surface of TiAl after 100,000 impacts of 500- $\mu$ m droplets impinged at 350 m/s, extracted from Mahdipoor <i>et al.</i> [1].	5
Figure 1-5: Erosion of compressor blades due to LIE, photo courtesy: Australian Transport Safety Bureau.....	6
Figure 1-6: Schematic drawing of erosion rate over time, extracted from Zhou <i>et al.</i> [2]. ....	8
Figure 1-7: Schematic presentation of micro-crack initiation due to lateral jetting of a water droplet, extracted from Kirols <i>et al.</i> [5].....	10
Figure 1-8: Formation of water drops in the stator and their impact on the blades in a steam turbine stage, extracted from Li <i>et al.</i> [6].....	11
Figure 1-9: (a) Schematic of the water droplet erosion rig, (b) Droplets generated using single- ray nozzle, (c) Droplets generated using multi-ray nozzle. ....	14
Figure 1-10: Ti-6Al-4V erosion by water droplet impingement, (a) top view, (b) cross-sectional view, extracted from Kamkar <i>et al.</i> [8]. ....	15
Figure 1-11: Cumulative weight/mass loss vs. number of droplet impingements, for (a) rolled, (b) forged Ti-6Al-4V substrates, extracted from Kamkar <i>et al.</i> [8]. ....	16

Figure 1-12: Schematic presentation of a high-speed liquid droplet impact on a rigid solid substrate and possible locations of micro-cracks, extracted from Li <i>et al.</i> [6].	20
Figure 1-13: Schematic presentation of lateral jetting due to shock front overlap with the droplet free surface, extracted from Haller [25].	22
Figure 1-14: Construction of compression wave envelope proposed by Lesser [23], extracted from Haller [25].	22
Figure 2-1: Piecewise Linear Interface Calculation (PLIC) representation of an interface.	34
Figure 2-2: Numerical algorithm for (a) one-way coupling, (b) two-way coupling, approaches.	38
Figure 2-3: Computational domain for 2D axisymmetric FSI model.	39
Figure 2-4: Contours of pressure (left) and velocity (right), $D=500 \mu\text{m}$ , $V_0=100 \text{ m/s}$ , rigid substrate.	45
Figure 2-5: Streamlines (left) and velocity vectors (right), $D=500 \mu\text{m}$ , $V_0=100 \text{ m/s}$ , rigid substrate.	46
Figure 2-6: Dimensionless pressure along r-axis, $D=500 \mu\text{m}$ , $V_0=100 \text{ m/s}$ , rigid substrate.	48
Figure 2-7: Dimensionless pressure along y-axis, $D=500 \mu\text{m}$ , $V_0=100 \text{ m/s}$ , rigid substrate.	48
Figure 2-8: Dimensionless radial velocity along r-axis, $D=500 \mu\text{m}$ , $V_0=100 \text{ m/s}$ , rigid substrate.	49
Figure 2-9: Dimensionless vertical velocity along y-axis, $D=500 \mu\text{m}$ , $V_0=100 \text{ m/s}$ , rigid substrate.	49
Figure 2-10: Liquid volume fraction along r-axis, $D=500 \mu\text{m}$ , $V_0=100 \text{ m/s}$ , rigid substrate.	50
Figure 2-11: Liquid volume fraction along y-axis, $D=500 \mu\text{m}$ , $V_0=100 \text{ m/s}$ , rigid substrate.	50
Figure 2-12: Maximum dimensionless pressure vs. impact velocity, $D=500 \mu\text{m}$ , rigid substrate.	52

Figure 2-13: Maximum pressure and stress profile along the interface over time, $D=500 \mu\text{m}$ , $V_0=100 \text{ m/s}$ .	53
Figure 2-14: Pressure approximation with a triangular pulse for validation with ANSYS.	55
Figure 2-15: Incompressible FSI solver validation with ANSYS, $D=500 \mu\text{m}$ , $V_0=100 \text{ m/s}$ .	55
Figure 2-16: Effect of solid elasticity on maximum pressure, $D=500 \mu\text{m}$ , $V_0=100 \text{ m/s}$ .	56
Figure 2-17: Comparison between compressible and incompressible solvers, $D=500 \mu\text{m}$ , $V_0=100 \text{ m/s}$ , rigid substrate.	58
Figure 2-18: Effect of fluid compressibility on maximum stress in the solid, $D=500 \mu\text{m}$ , $V_0=100 \text{ m/s}$ .	59
Figure 2-19: Effect of fluid compressibility on substrate deformation, $D=500 \mu\text{m}$ , $V_0=100 \text{ m/s}$ .	59
Figure 3-1: Schematic presentation of a compressible liquid droplet impact on a rigid solid substrate.	61
Figure 3-2: Computational domain (quarter) for the 3D model.	64
Figure 3-3: Contours of pressure (left) and velocity (right), $D=200 \mu\text{m}$ , $V_0=500 \text{ m/s}$ , rigid substrate.	68
Figure 3-4: Streamlines (left) and velocity vectors (right), $D=200 \mu\text{m}$ , $V_0=500 \text{ m/s}$ , rigid substrate.	69
Figure 3-5: Contours of density (left) and temperature (right), $D=200 \mu\text{m}$ , $V_0=500 \text{ m/s}$ , rigid substrate.	70
Figure 3-6: Dimensionless pressure along r-axis, $D=200 \mu\text{m}$ , $V_0=500 \text{ m/s}$ , rigid substrate.	74
Figure 3-7: Dimensionless pressure along y-axis, $D=200 \mu\text{m}$ , $V_0=500 \text{ m/s}$ , rigid substrate.	74
Figure 3-8: Dimensionless radial velocity along r-axis, $D=200 \mu\text{m}$ , $V_0=500 \text{ m/s}$ , rigid substrate.	75

Figure 3-9: Dimensionless vertical velocity along y-axis, $D=200 \mu\text{m}$ , $V_0=500 \text{ m/s}$ , rigid substrate.....	75
Figure 3-10: Dimensionless density along r-axis, $D=200 \mu\text{m}$ , $V_0=500 \text{ m/s}$ , rigid substrate. ....	76
Figure 3-11: Dimensionless density along y-axis, $D=200 \mu\text{m}$ , $V_0=500 \text{ m/s}$ , rigid substrate. ....	76
Figure 3-12: Dimensionless temperature along r-axis, $D=200 \mu\text{m}$ , $V_0=500 \text{ m/s}$ , rigid substrate. ....	77
Figure 3-13: Dimensionless temperature along y-axis, $D=200 \mu\text{m}$ , $V_0=500 \text{ m/s}$ , rigid substrate. ....	77
Figure 3-14: Liquid volume fraction along r-axis, $D=200 \mu\text{m}$ , $V_0=500 \text{ m/s}$ , rigid substrate. ....	78
Figure 3-15: Density and radial liquid velocity along r-axis, (a) present work at $t^*=0.07$ , .....	79
Figure 3-16: Maximum dimensionless pressure versus $Ma$ , comparison with Heymann [19]. ....	80
Figure 3-17: Maximum dimensionless pressure versus droplet diameter, comparison with Heymann [19]. ....	83
Figure 3-18: Maximum dimensionless pressure versus impingement angle, comparison with Heymann [19]. ....	85
Figure 3-19: Contours of pressure (left) and velocity (right), $D=500 \mu\text{m}$ , $V_0=350 \text{ m/s}$ , $h/D=0.2$ . ....	88
Figure 3-20: Contours of density (left) and temperature (right), $D=500 \mu\text{m}$ , $V_0=350 \text{ m/s}$ , $h/D=0.2$ .....	89
Figure 3-21: Contours of liquid volume fraction, $D=500 \mu\text{m}$ , $V_0=350 \text{ m/s}$ , $h/D=0.2$ . ....	90
Figure 3-22: Maximum dimensionless pressure versus film thickness to droplet diameter ratio. ....	91
Figure 3-23: Maximum dimensionless pressure versus Mach number, $h/D=0.2$ , $D=500 \mu\text{m}$ . ....	92
Figure 3-24: FEM model computational domain and mesh. ....	93
Figure 3-25: (a) Maximum dimensionless stress magnitude comparison, (b) maximum deformation to droplet diameter ratio, at the impact point.....	96

Figure 3-26: X-Normal stress, (a) magnitude along center axis, (b) contour. ....	97
Figure 3-27: Equivalent stress, (a) magnitude along center axis, (b) contour. ....	98
Figure 3-28: XY shear stress, (a) magnitude along center axis, (b) contour. ....	99
Figure 3-29: Substrate deformation to droplet diameter ratio (a) along center axis, (b) contour. .....	100
Figure 6-1: Dimensionless pressure along r-axis modeled with 3 different grid sizes. ....	111
Figure 6-2: Maximum dimensionless pressure versus droplet diameter, $h/D=0.2$ , $V_0=350$ m/s. ....	113
Figure 6-3: Maximum dimensionless pressure versus Mach number, $h/D=0.02$ , $D=500$ $\mu\text{m}$ . ....	115

# List of Tables

Table 2-1: Fluid properties for air and water at atmospheric condition. ....	40
Table 2-2: Structural properties of isotropic Ti-6Al-4V. ....	40
Table 2-3: Definition of dimensionless variables. ....	43
Table 3-1: Fluid properties for air and water at atmospheric condition. ....	65

# Nomenclature

$D$	= droplet diameter (m)
$R$	= droplet radius (m)
$E$	= Young's modulus (Pa)
$F$	= deformation gradient tensor
$g$	= gravity ( $\text{m/s}^2$ )
$h$	= film thickness (m)
$n$	= normal direction
$p$	= pressure (Pa)
$S$	= St. Venant-Kirchhoff tensor
$t$	= time (s)
$U$	= displacement (m)
$V$	= velocity (m/s)

Greek letters:

$\alpha$	= volume fraction, thermal diffusivity ( $\text{m}^2/\text{s}$ )
$\sigma$	= stress tensor, surface tension (N/m)
$\delta$	= deformation (m)
$\mu$	= liquid viscosity ( $\text{N}\cdot\text{s}/\text{m}^2$ ), Lamé coefficient
$\lambda$	= Lamé coefficient
$\nu$	= Poisson ratio
$\rho$	= density ( $\text{kg}/\text{m}^3$ )
$\Omega$	= computational domain
$\Gamma$	= fluid-solid interface

Subscripts:

$0$	= initial condition
$f$	= fluid
$g$	= gas
$l$	= liquid
$s$	= solid

# 1. Introduction

In this chapter a short background of water injection cooling system in gas turbine engines is presented followed by an introduction to Liquid Impingement Erosion (LIE) phenomenon in power generation and aerospace industries. The impact of LIE on compressor and turbine blades is briefly explained. The motivation behind the current work is outlined and the previous works in the open literature are reviewed. Finally, the objectives of this PhD thesis and the outline are presented.

# 1.1 Background

It is a common practice in power generation industries to inject atomized water into gas turbine engines in order to boost the engine power at high ambient temperatures. The heat removal from the air via vaporization of water droplets increases the engine output significantly. For instance, the increase in the generated power is illustrated in figure 1-1 for Trent 60 engine, fabricated by Siemens Canada (formerly Rolls-Royce Canada). As shown in this figure, at ambient temperatures above 15 °C the generated terminals power (Y axis, left) drops rapidly when there is no inlet conditioning (solid blue line). Contrariwise, when an Inlet Spray Intercooling (dashed blue line) mechanism is employed, the generated power is increased by 10 MW (at ambient temperature of 40 °C) and the nominal performance is improved noticeably.

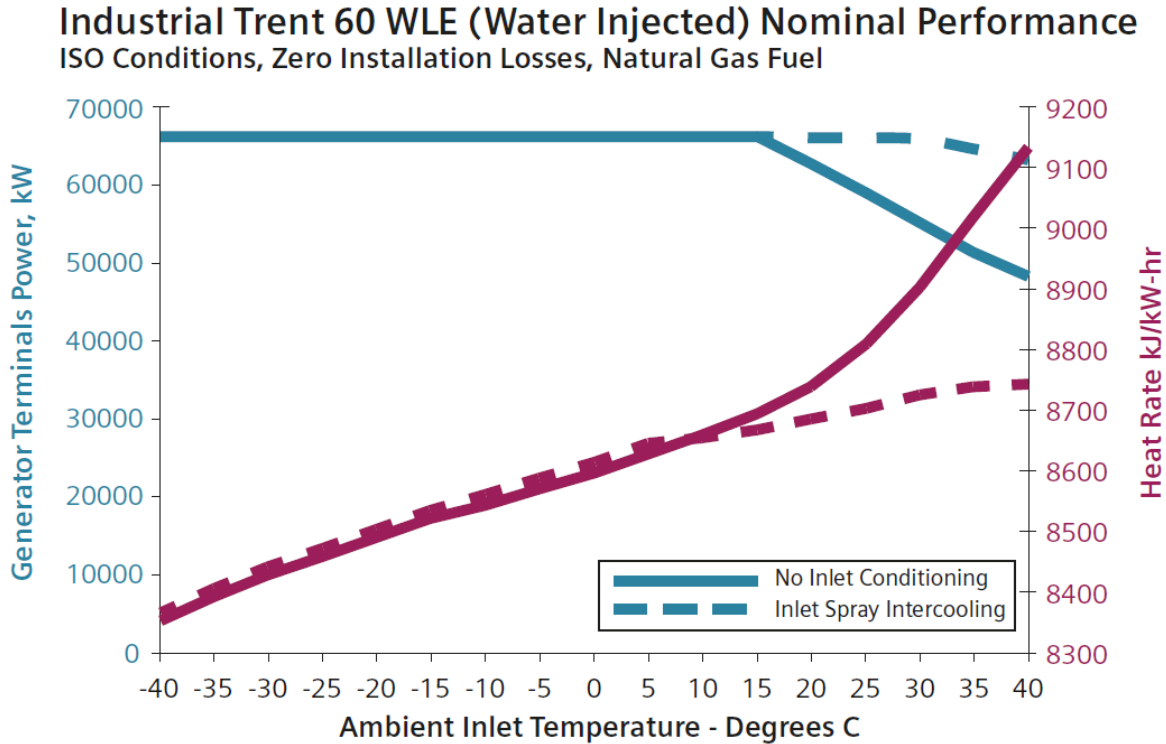
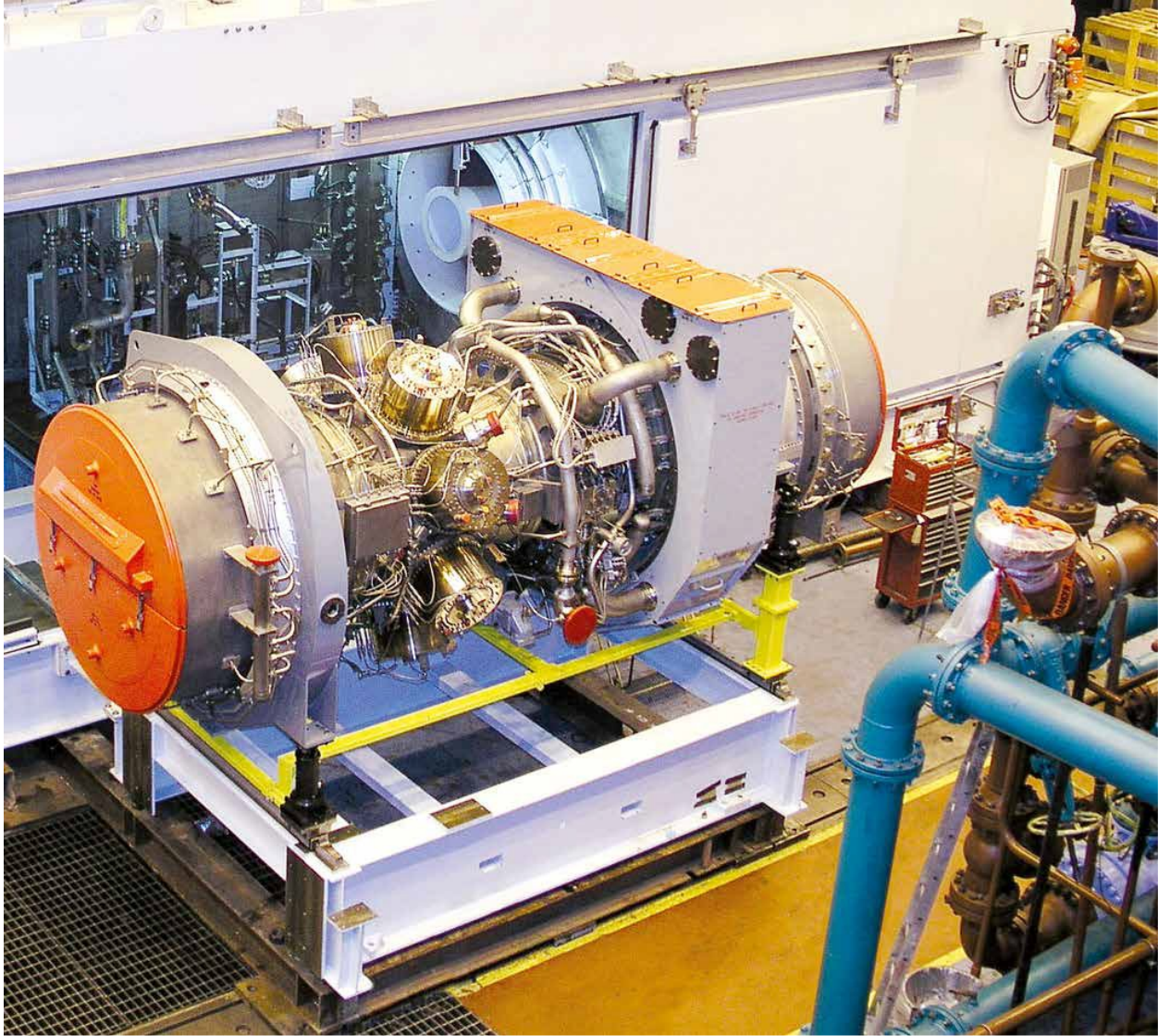


Figure 1-1: Trent 60 Wet Low Emissions (WLE) nominal performance, photo courtesy: Siemens.



**Figure 1-2: Industrial Trent 60 gas turbine with Rolls-Royce aero-engine technology test facility in Montreal, Canada, photo courtesy: Siemens.**

Figure 1-2 illustrates the industrial Trent 60 gas turbine engine in a test facility in Montreal, Canada. This aero-derived gas turbine is designed for both power generation and mechanical drive uses and is considered one of the most powerful and efficient engines in its class, available on the market. In addition, it can be operated with both liquid and gas fuels. Trent 60 engine can generate up to 66 MW of power at ISO conditions, but at higher

temperatures, its output decreases considerably. In order to compensate for this power loss, an Inlet Spray Intercooling (ISI) mechanism is employed to inject water and reduce the energy required for air compression by decreasing the ambient inlet temperature. There are various methods of spraying water to the engine invented by gas turbine manufacturers. An example of such systems, called Sprint® and manufactured by GE, is presented in figure 1-3.

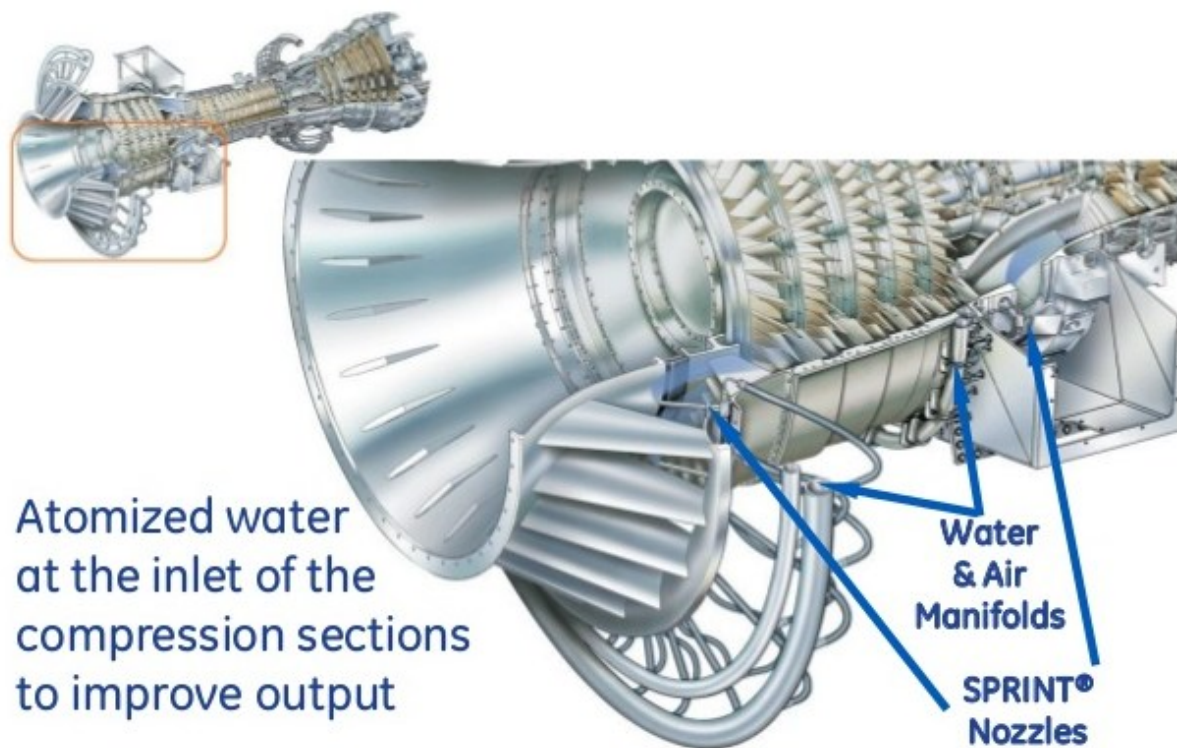


**Figure 1-3: Sprint® Spray Intercooling system, photo courtesy: GE.**

The main drawback of this cooling method is the substantial reduction of the blade life in compressor stages due to Liquid Impingement Erosion, caused by high frequency droplet impacts. Since the mass flow rate of the injected water, and thus the number of sprayed droplets are significant, large droplets are formed from coalescence of smaller droplets on static components. Initially, the mean diameter of droplets injected from the spray nozzle is typically

around 20  $\mu\text{m}$  and larger droplets, up to 500  $\mu\text{m}$  in mean diameter, are formed after coalescence. Further downstream, these large droplets, carried with the air flow, impact the rotary parts in the compressor with high relative velocities, due to the high linear velocity of the rotating blades, particularly at the blade tip (around 350 m/s). The consecutive impacts of water droplets at such high speeds change the surface roughness on the compressor blades and initiate solid erosion.

In order to visually illustrate this phenomenon, Atomic-force Microscopy (AFM) images of a TiAl substrate before and after impacts of 100,000 water droplets with a mean diameter of 500  $\mu\text{m}$  at a velocity of 350 m/s are displayed in figure 1-4. As it can be seen in figure 1-4-b, the surface topography has completely altered, even if there is no material loss yet, indicating the incubation stage (to be discussed in section 1.2). The average roughness of the surface increased from 0.038 to 0.117  $\mu\text{m}$  according to Mahdipoor *et al.* [1], signifying erosion initiation.

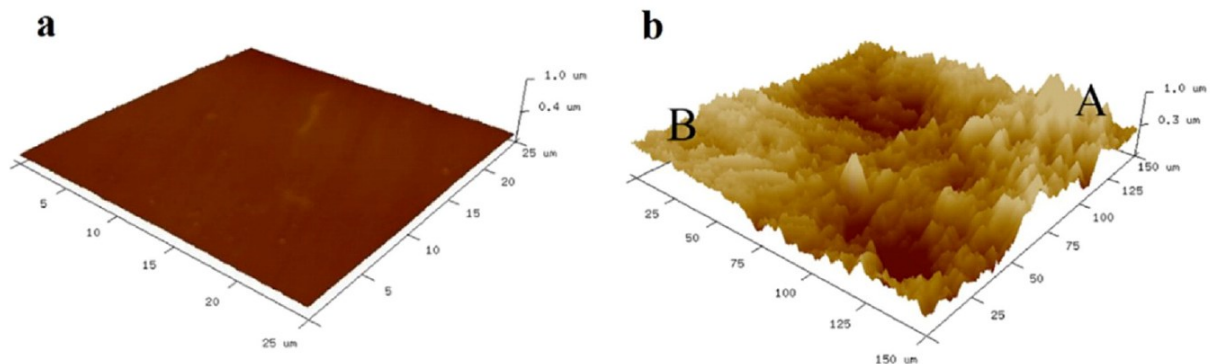


**Figure 1-4: AFM images of (a) original polished surface of TiAl, (b) eroded surface of TiAl after 100,000 impacts of 500- $\mu\text{m}$  droplets impinged at 350 m/s, extracted from Mahdipoor *et al.* [1].**

Although the surface roughness is one of the parameters that affect liquid droplet interaction with the solid surface, throughout most research projects and the current work, the solid surface is assumed to be entirely flat and smooth, since the focus is on the hydrodynamics of the impact and not on the surface topography. Nevertheless, the surface texture and roughness can be simulated with the current model by applying very refined mesh (in nano scale) to the nanostructured columns representing the solid texture.

Once the surface roughness is altered, the repetitive droplet impingements lead to the material spall-off from the blade surface. Continued erosion of the compressor blade results in further material loss and distortion of the blade profile, hence, the blade life and its aerodynamic performance significantly decrease. In addition, the weight loss of the compressor blades affects the vibrational characteristics of the engine. This change can induce large instabilities in the compressor stages, which could have severe consequences, such as engine malfunction or even explosion. An example of LIE effect on compressor blades is displayed in figure 1-5, where one of the blades is eventually chopped off due to extensive erosion.

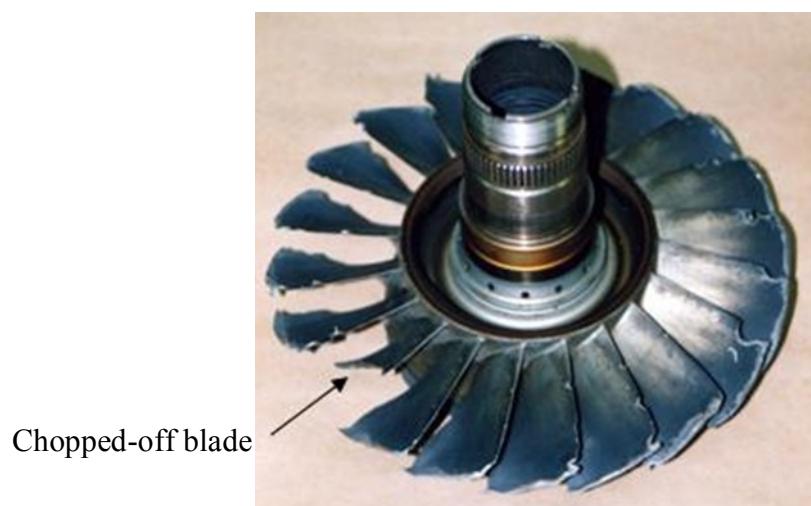


**Figure 1-5: Erosion of compressor blades due to LIE, photo courtesy: Australian Transport Safety Bureau.**

In summary, major consequences of LIE in gas turbine engines are as follows,

- Drop in aerodynamic performance due to geometry change
- Engine instability due to loading change
- Reduction in life time of rotor blades
- Unscheduled maintenance
- Engine shut-off/power loss
- Destruction of engine components
- Engine explosion in severe cases
- High costs

For all of the reasons mentioned above, finding new methods to reduce the blade erosion caused by LIE is of high importance for power generation and aerospace industries. Although LIE has been the focus of many researchers during the past decades, many fundamental issues associated with high speed droplet impingement, e.g. compressibility effects, air entrapment and fluid-solid interaction, are yet to be fully investigated.

## 1.2 Liquid Impingement Erosion (LIE)

Liquid Impingement Erosion is an interdisciplinary phenomenon as it involves both fluid dynamics and solid mechanics. Predicting the potential damage to the solid material is of high interest in various engineering applications and it requires capturing the flow characteristics in the liquid counterpart accurately. Once the fluid flow and solid stress are resolved, the erosion caused by the liquid impact can be determined. In this regard, establishing an erosion curve is beneficial to predict the material loss from the blade over time. An example of an erosion curve for water droplet impingement is illustrated in figure 1-6.

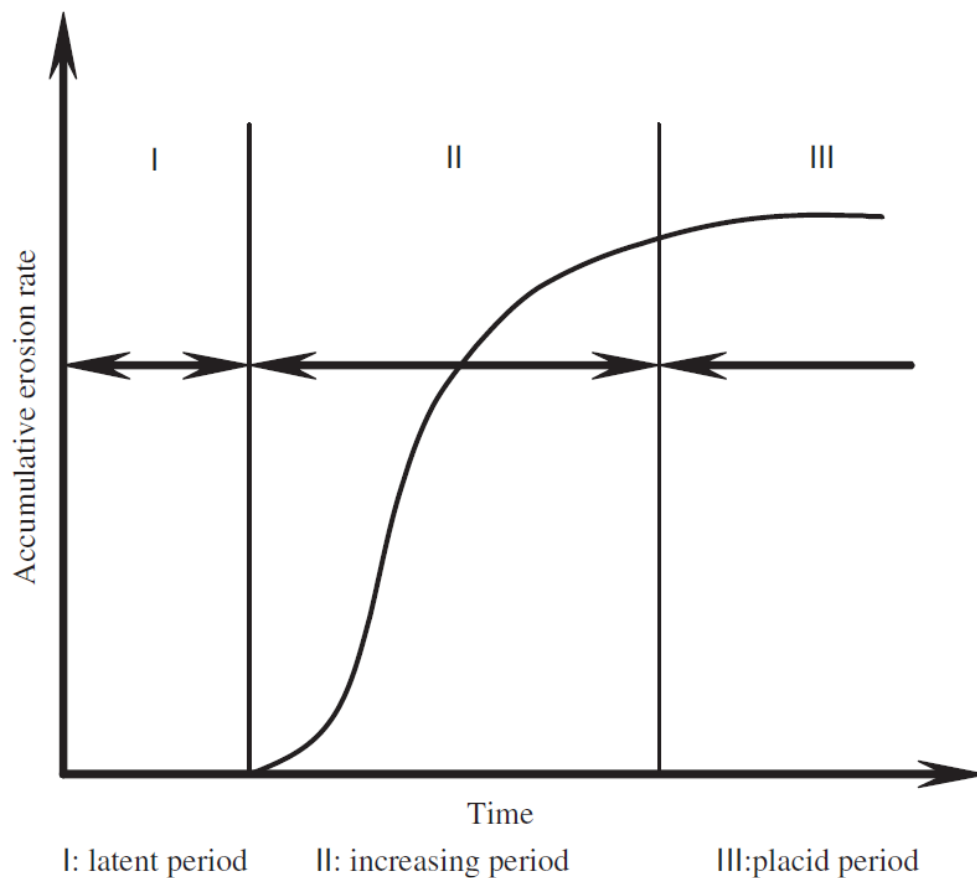


Figure 1-6: Schematic drawing of erosion rate over time, extracted from Zhou *et al.* [2].

In the erosion curve presented in figure 1-6, three distinct regimes are noticeable: latent, increasing and placid periods. The first stage is the latent period, widely known as the incubation time. During this period, the material experiences plastic deformation and its surface roughness alters, nevertheless, no part of the material spalls off. The second stage, known as the increasing period, starts right at the end of the latent period during which, the erosion rate increases rapidly and causes the material removal from the solid. Finally, following a rapid increase and the formation of a considerable depth in the solid, the placid period occurs when the erosion rate reaches a steady state value.

In 1927, Honegger [3] shed light on the mechanisms of LIE with a series of experiments. He argued that no erosion is observed prior to the formation of roughness on the surface. After the incubation stage, the erosion rate grows rapidly as the droplets penetrate the uneven surfaces due to the high impingement velocity. The droplets impact the rotor blades at a considerable relative velocity (up to 500 m/s) which results in high transient stresses in the solid material. Since the impingements are consecutive, fatigue causes the material to spall off from the blade surface. At the end of this period, a layer of liquid film forms on the surface and fills the gaps in the solid. As a result, the impinged droplets do not impact the solid directly, due to the liquid film cushion, and the damage on the solid surface is reduced. Therefore, modeling droplet impact onto a liquid film is also of high importance in studying LIE and will be addressed in the current work.

The high speed droplet impact is associated with high compressive stresses beneath the solid surface. Since the impingements onto the blade surface are repeated, the stress build up in the blade material generates micro-cracks on the solid surface. As a result, the main mechanism that governs liquid impingement erosion is considered to be similar to fatigue. Upon

impingements of liquid droplets onto the solid surface, pressure pulses are generated inside the fluid. The loading and unloading of the pressure force produced by the impact lead to the development of craters on the surface and the material loss occurs at these craters via ductile rupturing according to Bargmann [4]. The craters alter the surface topography, hence, the hydrodynamic loading on the surface varies during frequent droplet impingements as the impact angle changes. Thus, the impingement angle is another parameter that has to be examined separately in studying LIE and will be discussed in chapter 3. Consequently, the material behavior alters in response to the repetitive impact loading and the work of hardening on the surface. The periodic roughening and polishing caused by the water droplet on the craters have been shown to govern the progress of the damage. In advanced stages of LIE, the main causes of the damage to the solid surface are identified as water hammering and penetration on the surface and stress wave propagation inside the solid according to Kirols *et al.* [5]. The liquid-solid interaction during lateral jetting (will be thoroughly explained in section 1.4.1) of the water droplet after the impact is schematically represented in figure 1-7.

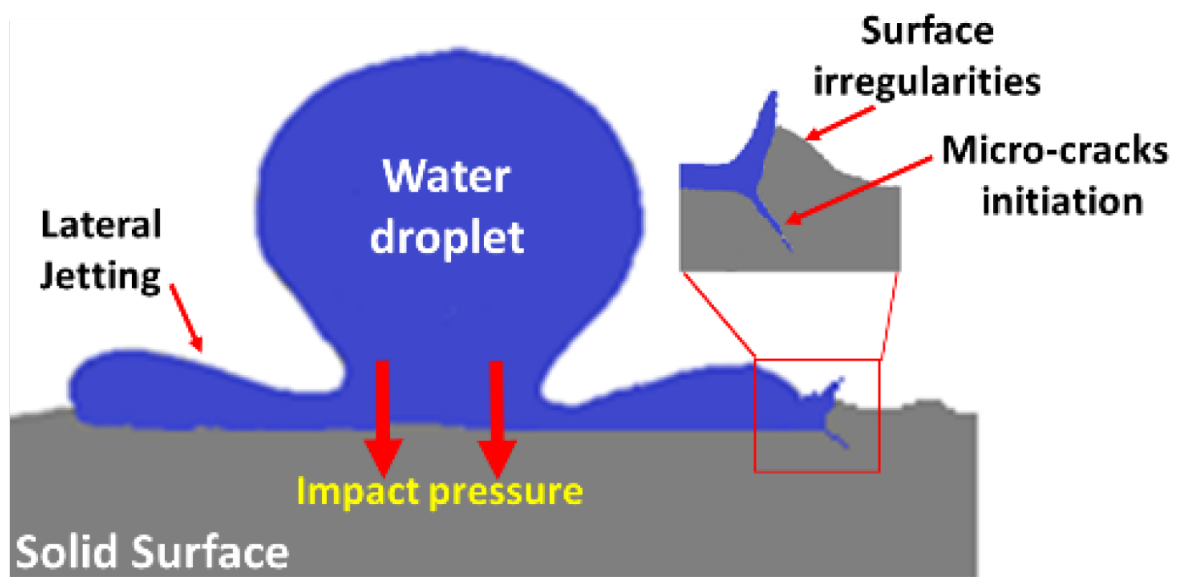
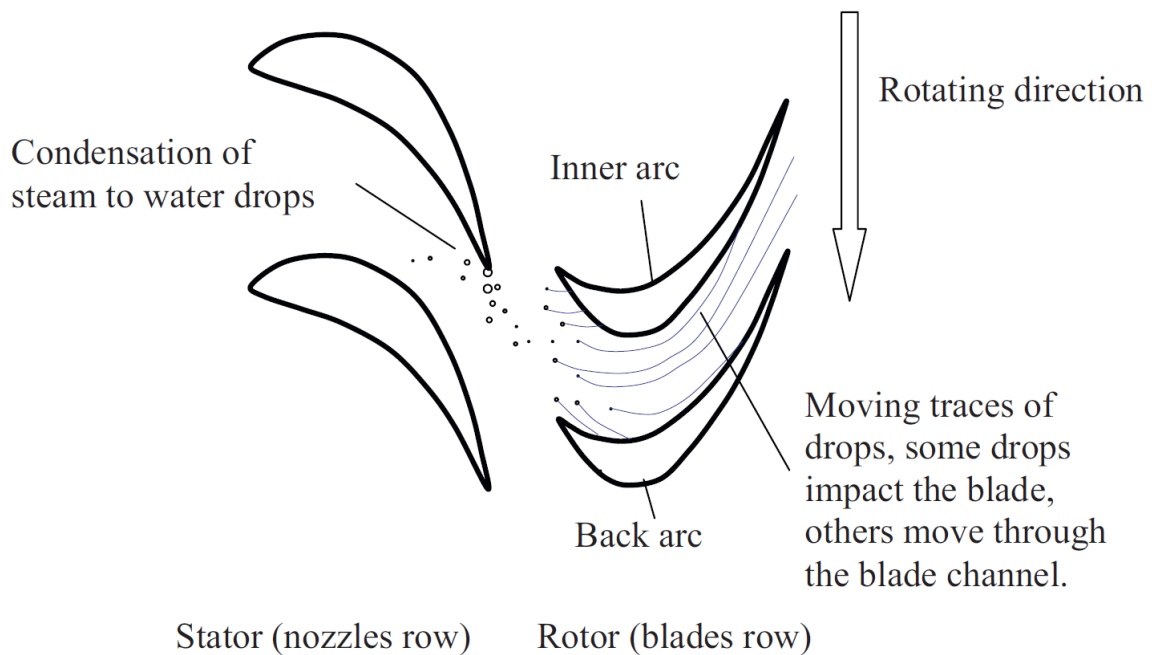


Figure 1-7: Schematic presentation of micro-crack initiation due to lateral jetting of a water droplet, extracted from Kirols *et al.* [5].

In general, LIE occurs in industrial gas turbines or aero engines when a compressor or turbine blade rotating at a high speed is exposed to the liquid droplets carried with the air stream. Similarly, in steam turbines, a comparable phenomenon exists due to the condensation of water droplets, as illustrated in figure 1-8. As the air flow mixed with vapor loses its kinetic energy during energy transfer in the turbine stage (nozzles row), water droplets are formed. The droplets, carried with the gas flow, impact the rotor blades at high velocities (blades row). The high relative velocity between the blade surface and the droplets results in generation of significant stresses in the solid material. Since the impacts are repetitive, they can cause severe damage to the blade and reduce its life considerably.



**Figure 1-8: Formation of water drops in the stator and their impact on the blades in a steam turbine stage, extracted from Li *et al.* [6].**

Replacing the compressor or turbine blades is very costly and it requires the whole engine to be shut down during the overhaul. Hence, it is essential to understand the fundamentals of LIE in order to improve the material resistance to erosion and increase its life span. Bargmann [4] stated that liquid impingement erosion is dependent on space and time, hence, it can be expressed as a stochastic process. Therefore, the droplet size distribution, the impact velocity, the frequency of impingements, and the location of impacts are needed to solve the fluid-solid problem simultaneously.

Once the spatial time history of the pressure field in the liquid and the stress field in solid are obtained from a single impact, the total damage can be predicted by carrying out the fatigue analysis on the solid as explained by Springer [7]. Since experimental measurements and optical data acquisitions inside the engine compartments are impractical and rather very expensive, numerical tools and analytical models become imperative in studying LIE. In this regard, developing a robust numerical tool that is capable of predicting the pressure force and the stresses generated by high speed droplet impingements is very beneficial to various industries and the main motivation behind this thesis.

## 1.3 Motivation

The current work is part of a collaborative research project funded by *Siemens Canada* (formerly *Rolls-Royce Canada*) and two governmental agencies, namely, *Consortium de Recherche et d'Innovation en Aérospatiale au Québec (CRIAQ)* and *Nano-Quebec*. The main project, titled "Water Erosion Resistant Surface Treatments", involved three academic institutions, namely, Concordia University, École Polytechnique de Montréal and École de Technologie Supérieure (ÉTS). The ultimate objective was to find new surface treatments that are more resistant to Water Droplet Impingement Erosion (WDIE). Therefore, both experimental and numerical analyses were conducted, in parallel, to investigate the erosion of Titanium alloys, in particular Ti-6Al-4V (widely referred to as Ti64), subject to droplet impingements at high speeds. It is worth mentioning that the alloy under investigation, i.e. rolled Ti-6Al-4V, is commonly used in manufacturing of compressor and turbine blades.

The experimental analyses were performed using a state of the art erosion rig, specifically designed to study WDIE. Figure 1-9 (a) schematically displays the experimental rig installed in Thermodynamics of Materials Group (TMG) lab at Concordia University, used to carry out the experiments. The turbine shaft can rotate the disk at speeds up to 20,000 RPM in a vacuum chamber, corresponding to a linear impact velocity of 500 m/s. The material samples, called erosion coupons, are installed at the tip of the disk and located below the droplet generator nozzle. The test rig allows controlling the impingement parameters, including impact speed, impact angle, droplet size, and number of impacting droplets. Furthermore, various nozzle types, such as single-ray (figure 1-9 (b)), multi-ray (figure 1-9 (c)) and shower-head (not shown in the figure), can be used to inject a single streak, multiple streaks and a water spray, respectively.

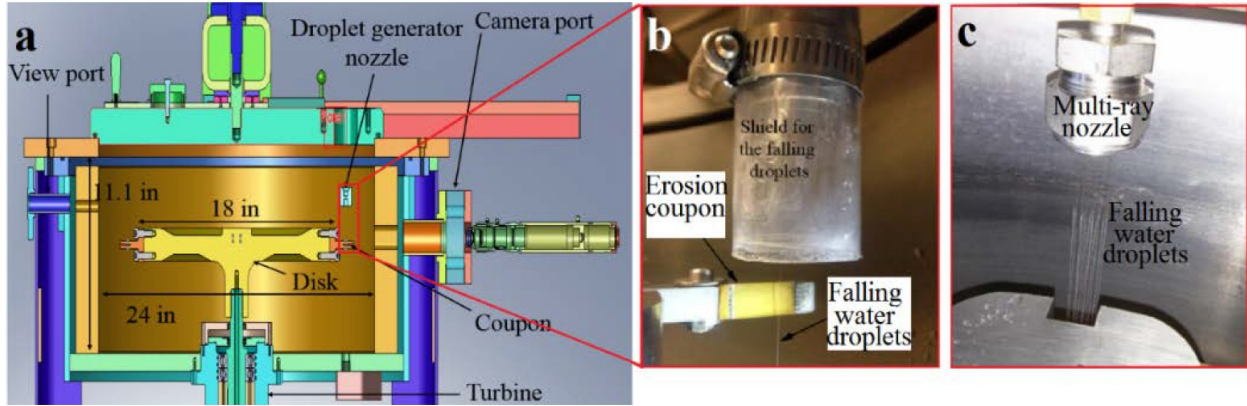


**Figure 1-9: (a) Schematic of the water droplet erosion rig, (b) Droplets generated using single-ray nozzle, (c) Droplets generated using multi-ray nozzle.**

Figure 1-10 illustrates a Ti-6Al-4V sample, exposed to continuous impingements of water droplets with a multi-ray nozzle (three injectors), from (a) top and (b) cross-section. The mean droplet diameter and impact velocity were reported to be 600  $\mu\text{m}$  and 350 m/s, respectively. According to Kamkar *et al.* [8], the average diameters of the craters were measured to be 1.27 mm which is about twice the initial diameter of the impinging droplets. This observation demonstrates the destructive effect of liquid droplet impingement on the surface erosion of the material. In order to quantify the material loss versus the number of droplets impinged on the substrate, the sample was weighted several times during the experiment. The cumulative mass loss, normalized with the total mass removed from the sample, is presented in figure 1-11 (a) and (b) for rolled and forged Ti-6Al-4V alloy, respectively. As discussed earlier, in the early stage or incubation period, the surface roughness is changed dramatically but no apparent material removal occurs. The erosion rate increases rapidly in the next stage, during which most of the mass loss happens. The mass removal from the solid decreases over time once the erosion reaches a steady state stage, as shown in figure 1-11.

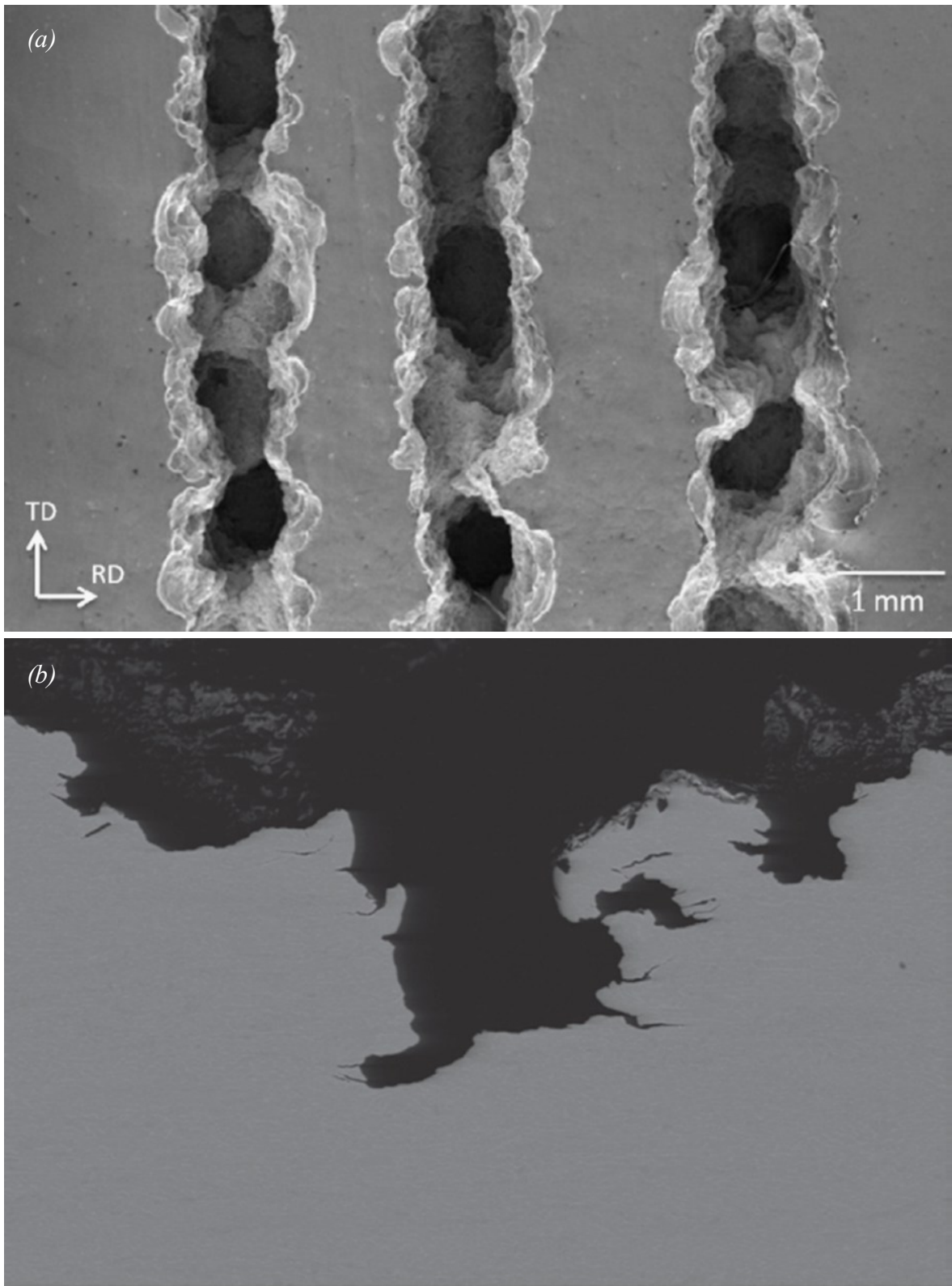
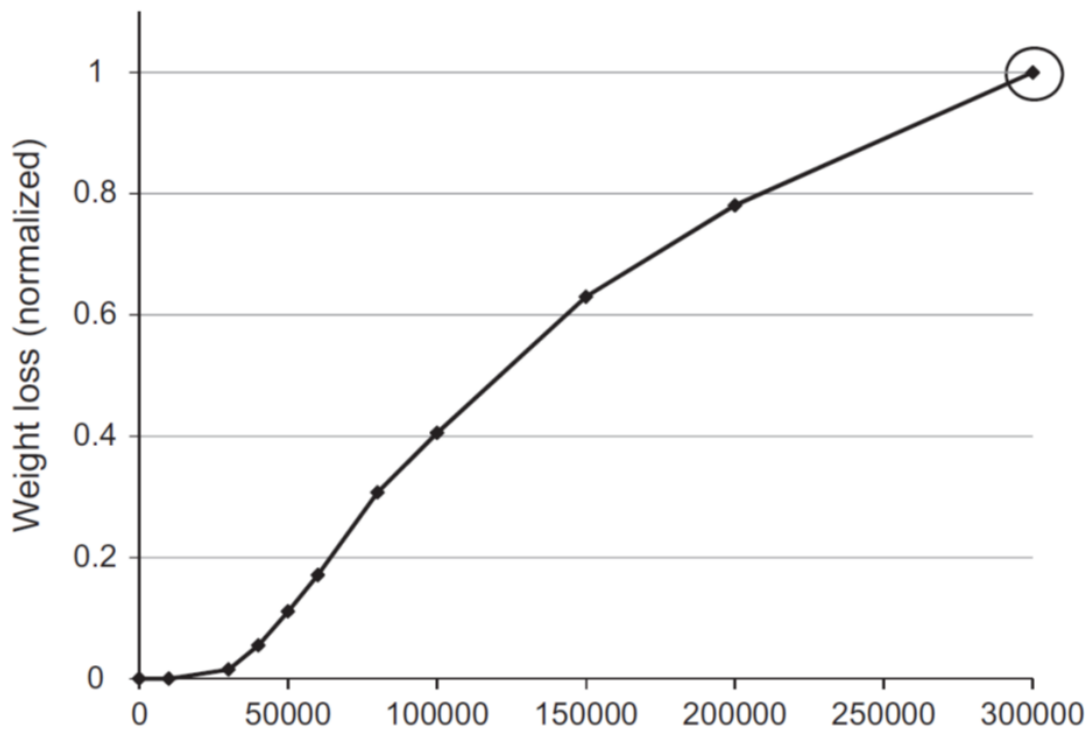


Figure 1-10: Ti-6Al-4V erosion by water droplet impingement, (a) top view, (b) cross-sectional view, extracted from Kamkar *et al.* [8].

(a)



(b)

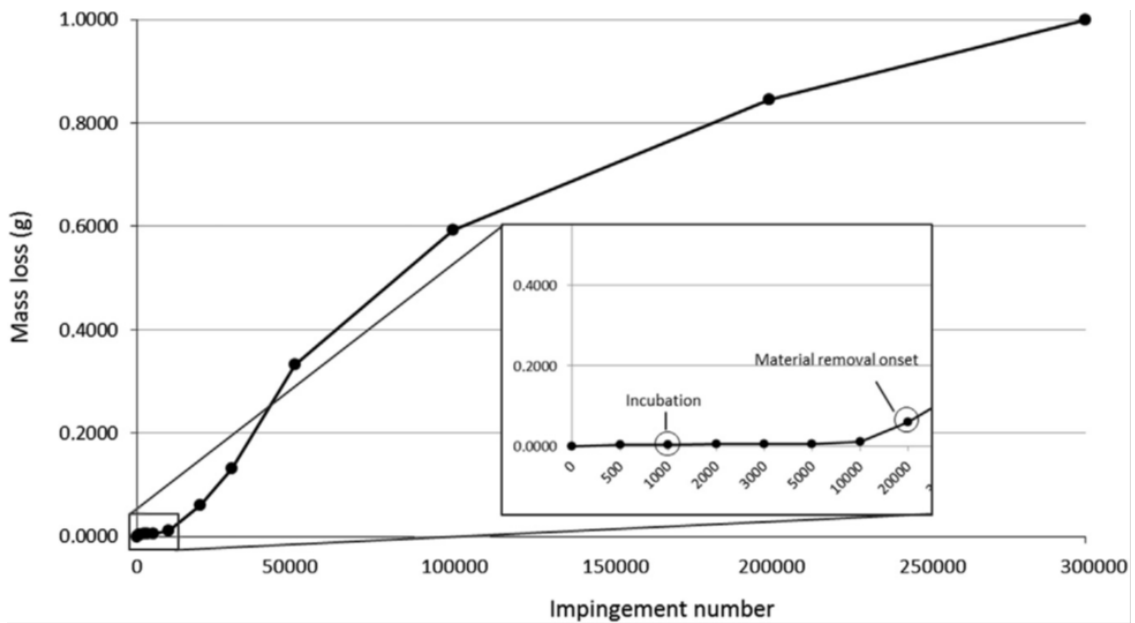


Figure 1-11: Cumulative weight/mass loss vs. number of droplet impingements, for (a) rolled, (b) forged Ti-6Al-4V substrates, extracted from Kamkar *et al.* [8].

In order to gain in-depth knowledge of the droplet impingement at such high speeds (up to 500 m/s), the current PhD thesis was proposed and dedicated to the numerical analysis of droplet impingements at incompressible and compressible flow regimes. For the most part in this work, the emphasis was placed on the fluid dynamics of the impact to understand the physics behind the droplet impingement. In addition, a Fluid-Solid Interaction (FSI) model was utilized to quantify the outcome of droplet impacts and predict the consequent stress in the solid material. Such a model facilitates finding new ways to reduce the blade erosion and based on these results, modifications can be proposed for future designs.

The 3-D FSI solver implemented in the current study is capable of modeling the impacts of liquid droplets onto compressor blades or condensed water droplets onto steam turbine blades. The direct application of this model is in industrial gas turbines and steam turbines, however, the current model can also be applied to all liquid impingement erosion problems in general. Other areas where such a model can be valuable are thermal and plasma spray coatings. In these types of coatings, the melted metal particles impact the solid wall at a very high velocity and spread on the substrate, forming a coating layer. The impact of the molten metal particles can be simulated with the current model. Afterwards, the stress field generated inside the substrate can be calculated. In the case of coating a thin substrate, its deformation can be captured numerically. In order to achieve a uniform coating, the deformation of the coated substrate is of importance. Hence, the current FSI model can be a powerful tool to predict the coating uniformity and improve its quality.

## **1.4 Literature review**

Although the experimental study of droplet impacts dates back to 1876 by great scientists such as Worthington [9], it still remains an area of extensive study today. The advancement of high speed imaging techniques in addition to computational power have allowed researchers to obtain much higher temporal and spatial resolutions in capturing the hydrodynamics of droplet impingement. There are various physical phenomena that occur upon the impact of a liquid droplet on a solid substrate, such as spreading, fingering, air entrapment, bouncing and splashing, that drew the attention of various industries and academia.

For instance, the spreading of a droplet at low impingement velocities has been studied in details by Fukai *et al.* [10], Chandra and Avedisian [11], Pasandideh-Fard *et al.* [12] and more recently by Roisman *et al.* [13]. The entrapment of an air bubble underneath the droplet has been simulated by Mehdi-Nejad *et al.* [14]. Moreover, the formation of fingers upon impact of water drops was experimentally investigated by Mehdizadeh *et al.* [15]. Blake and De Conick [16] have extended the molecular-kinetic theory of dynamic wetting by considering the effect of fluid-solid interaction.

In an interesting study of droplet bounce-off, published in Nature, Bird *et al.* [17] have demonstrated that the contact time can be reduced below the theoretical limit by altering the surface morphology on superhydrophobic surfaces. However, in some applications such as agricultural sprays, it is advantageous to increase the droplet deposition. Damak *et al.* [18] proposed an alternative to traditional methods, by producing hydrophilic defects that change the surface properties in-situ. Most of the studies in droplet impingement are concerned with low impact velocities, hence, do not take into account the fluid compressibility, which becomes critical at higher impingement velocities in problems such as LIE.

### 1.4.1 High-speed droplet impingement

Commonly in practice, a spray composed of liquid droplets is impinged on the surface; nevertheless, the interaction between the droplets and their coalescence makes the spray impingement a complex phenomenon. For that reason, single droplets are studied in almost all analytical and numerical works and a spray effect is assumed to be approximately represented by the superimposition of a finite number of droplets.

To explore the details of a single droplet impingement at early stages, a schematic of a spherical droplet impacting a rigid solid substrate at a high speed is illustrated in figure 1-12. Upon the impact of a liquid droplet on a solid substrate at a high velocity, compression waves begin to propagate in the water droplet due to the fluid compressibility. These compression waves create a high density region in the liquid close to the solid surface and break away from the droplet periphery, giving rise to the formation of lateral jets, as reported by Heymann [19] and confirmed by the experiments of Dear *et al.* [20] and Field *et al.* [21].

The pressure waves generated in the liquid accumulate over time and form a high pressure front since the speed of sound changes in the compressed region, as displayed in figure 1-12. Compression waves travel through the compressed region at the speed of sound for liquid, hence, the rest of the droplet, outside the disturbed region, is not affected by the impact yet. The pressure and density inside the undisturbed region remain unchanged since it is completely unaware of the impact. As the liquid droplet continues its downward motion toward the solid, the high pressure front penetrates further into the liquid bulk and the compressed region increases in size. At the same time, the droplet contact line is moving outward, starting from the center axis, right after the droplet touches down on the surface.

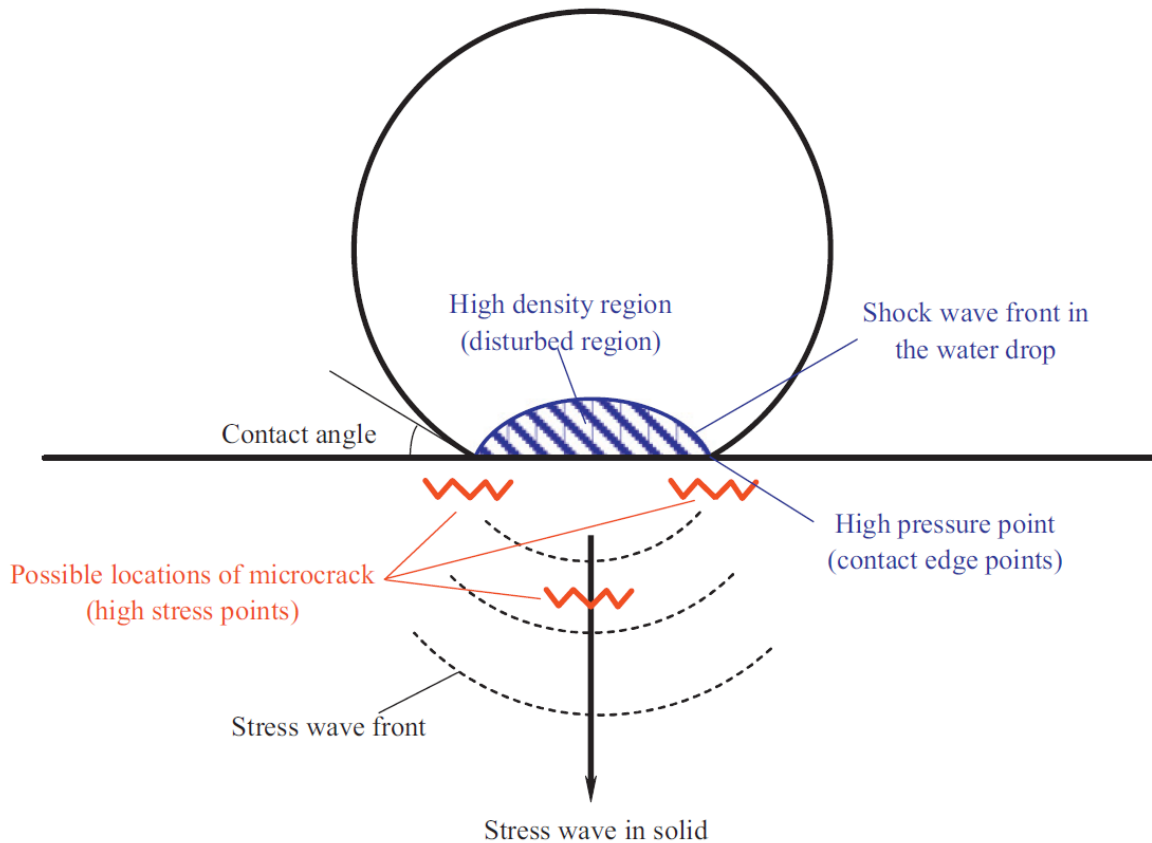


**Figure 1-12: Schematic presentation of a high-speed liquid droplet impact on a rigid solid substrate and possible locations of micro-cracks, extracted from Li *et al.* [6].**

Initially, the contact periphery spreads out much faster than the high pressure front. As the contact line starts to decelerate due to viscous dissipation, it is finally overtaken by the high pressure front that is spreading outward. At this exact instant, the high pressure front detaches and starts to travel along the free surface leading to the formation of lateral jets, as depicted in figure 1-13. This jetting eruption is the result of a very large difference between the pressure and density across the free surface of the droplet in contact line region. When lateral jetting occurs, the impact pressure reaches its temporal maximum value, as experimentally measured for the first time by Rochester and Brunton [22]. It has been shown, by Heymann [19] and Lesser [23],

that the pressure in the compressed area is not uniform and the location where the highest pressure appears is behind the contact line, as reported by Lesser and Field [24].

Lesser [23] has studied droplet impacts at low velocities analytically and in order to determine the exact position of the high pressure front, he proposed an envelope of individual wavelets emitted by the expanding contact edge as shown in figure 1-14. In his model, he assumed that the compression wave velocity is equal to the speed of sound in ambient condition. Although this assumption is valid for the acoustic limit, Haller [25] demonstrated that it is invalid for high impact velocities where the liquid compressibility effect is considerable. He has shown, both computationally and analytically, that the compression wave velocity during the first stage of the impact, at an impingement velocity of 500 m/s, is in the range of 2600-3000 m/s, which is significantly higher than the ambient speed of sound in water, i.e. 1430 m/s. Therefore, in modeling the compressible droplet impact, it is essential to account for the changes in the speed of sound, via the variation of liquid density, with an equation of state.

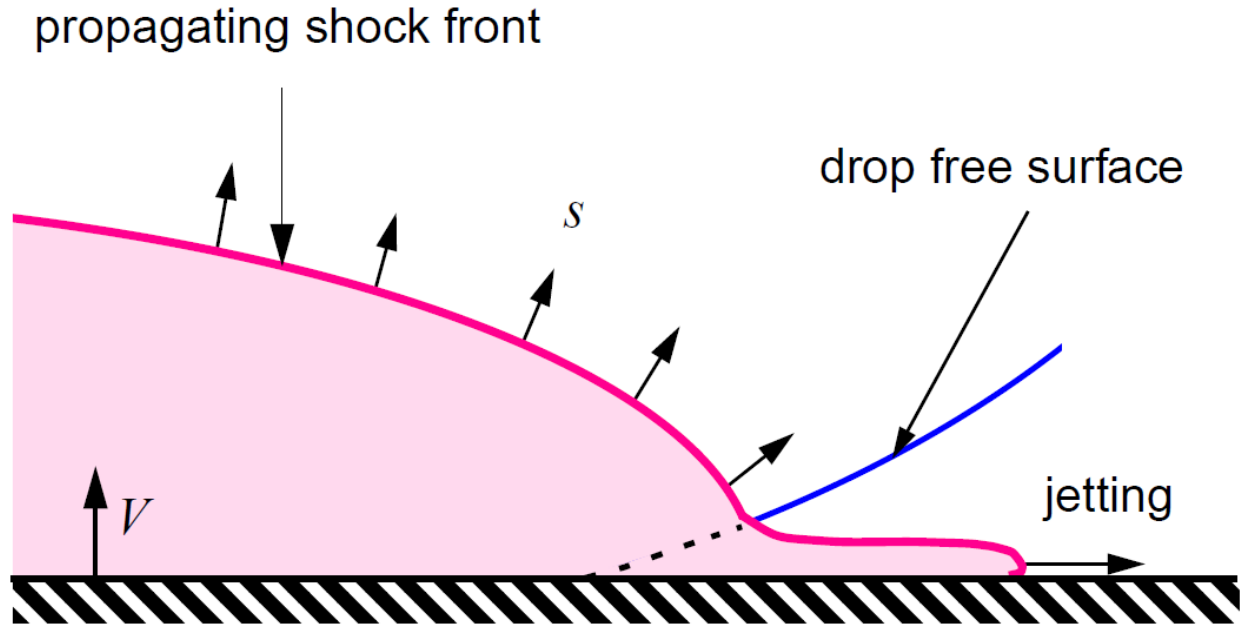


Figure 1-13: Schematic presentation of lateral jetting due to high pressure front overlap with the droplet free surface, extracted from Haller [25].

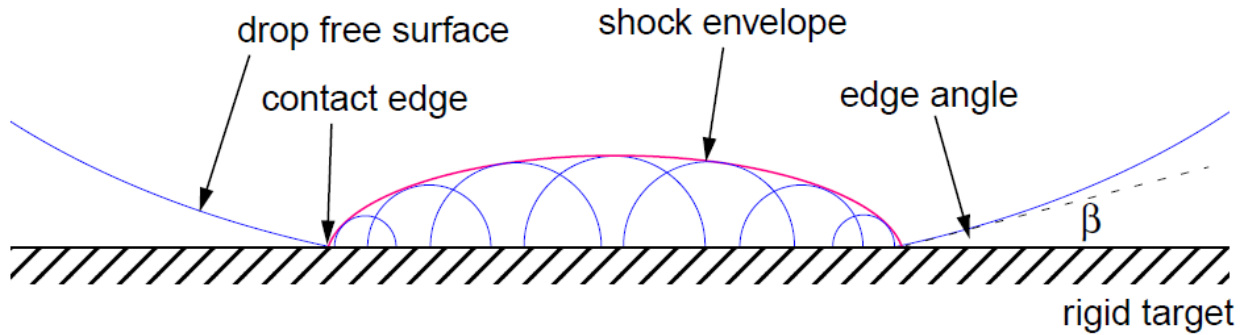


Figure 1-14: Construction of compression wave envelope proposed by Lesser [23], extracted from Haller [25].

## 1.4.2 Fluid-Solid Interaction (FSI)

Overall, modeling FSI can be divided into two main categories: one-way and two-way coupling of liquid and solid equations. In the first approach, the pressure field in the liquid is solved via analytical or numerical tools and then used as a boundary condition on the solid to obtain the stress field, e.g. the work reported by Shih [26]. It is believed that the first FSI model with one-way coupling was proposed by Honegger [3], in which, a liquid jet impacts a solid wall creating a constant pressure, commonly known as the water hammer pressure, defined as,

$$p_{wh} = \rho_0 V_0 C_0 \quad (1-1)$$

where  $\rho_0$  and  $C_0$  are density and the speed of sound in undisturbed liquid, respectively.  $V_0$  is the initial impact velocity or relative velocity between the liquid and solid. After Honegger, Cook [27] and Engel [28] reported the 1D steady-state solution for the water hammer pressure. Blowers [29] proposed another pressure model to obtain the stress field in rigid solids, which was decoupled from the pressure field in the liquid.

In addition to analytical methods, numerical simulations of droplet impacts on solid substrates at high velocities have been carried out. For instance, Adler and Mihora [30] utilized Finite Element Method to study water droplet impact onto a solid substrate at a high velocity. Moreover, several detailed analyses were performed to simulate high speed impact of droplets on rigid solids such as Haller *et al.* [31] and Huang *et al.* [32]. However, they only focused on the fluid dynamics of the phenomenon and did not study the stress field in the solid which is critical for liquid erosion problem.

It should be mentioned that the peak transient stress is much higher than its steady state value. This peak stress magnitude is responsible for the solid erosion according to Chen *et al.* [33]. Their approach was later improved by researchers such as Kim *et al.* [34] and Lee *et al.*

[35]. They replaced the pressure distribution on the solid surface with point loads which produce longitudinal and transverse waves that transmit normal and shear stresses, respectively. They reported the stress wave propagation generated by the droplet impact onto a coated elastic material by superimposing the longitudinal and transverse waves at each point in the solid. Although more accurate, their approach does not reflect the effect of dynamic pressure variation of the liquid droplet on the stress in the solid since the fluid and solid equations were segregated in their model.

More recently, Li *et al.* [20] numerically studied the Liquid Droplet Impingement (LDI) onto rigid solids. They reported two main issues that should be addressed in modeling LDI, the sound velocity change due to liquid compressibility and resolving the interfacial flow. Resolving these issues require a refined grid system and a time-accurate solution. They integrated the equation of state and sound speed function, to account for the liquid compressibility, into a 2D FLUENT model utilizing user-defined functions. They managed to achieve a good agreement in comparison with the existing theoretical work and proposed a correlation based on the impact angle.

In the two-way coupling approach, the space and time variation of the stress in the solid is directly coupled with the spatial pressure history in the fluid. This method allows to simultaneously predict the transient stresses and the pressure force imposed on the liquid-solid interface due to the impact. In 2008, a fully coupled FSI model in 1D was reported by Li *et al.* [6] for linear and nonlinear cases using Finite Difference Method. The Navier-Stokes equations were transformed into a single wave equation, assuming that the droplet deformation and displacement at the acoustic stage of the impact are negligible. Thus, the fluid compressibility plays the main role and the momentum term in Navier-Stokes equation can be ignored.

Moreover, the viscous and surface tension forces were assumed to be negligible since they are orders of magnitude smaller than the pressure force term. These simplifications reduce the computational cost enormously, however, they are only valid at early stages of the impact before the formation of lateral jets and droplet breakup on the surface. Haller *et al.* [36] have analytically proven that the single wave structure leads to an anomaly in the compressed region attached to the contact line and a multiple wave structure is required to capture jetting eruption. Furthermore, their numerical simulations [31] demonstrated that the maximum pressure occurs during lateral jetting and its magnitude at the droplet edge is much higher than the center.

In the analysis carried out by Li *et al.* [6], the 1D linear case of liquid impact on a rigid solid was solved both analytically and numerically for validation of their model, as a first step. Next, the nonlinear equation was solved numerically which predicted peak pressure values higher than the linear equation. They found out that the maximum stress is much larger than its steady state value, thus, it is responsible for the damage to the material. Moreover, at higher impact velocities, the impact pressure is increased due to the liquid compressibility and the maximum pressure is observed at the high pressure front. On the other hand, the solid elasticity acts against liquid compressibility and reduces the impact pressure.

The 1D numerical model developed by Li *et al.* [6] was further extended to a 2D axisymmetric model by Zhou *et al.* [2] since the compression wave propagation cannot be described precisely in one dimension. They utilized the elastodynamic equation to solve the solid displacement and cell marking method to separate the gas, liquid, and solid phases in the computational domain. They have shown that the maximum pressure and stress are independent of the droplet size and the dimensionless location where maximum stress appears in the solid does not vary with droplet diameter. Furthermore, the peak stress and pressure appear at the edge

of the droplet and move outward during the impact, as the high pressure front inside the liquid region travels from the contact center toward the droplet edge. It should be mentioned that the stress wave surpasses the pressure wave in a few nano seconds after the impact since the acoustic speed in the solid is much higher than the acoustic speed in the liquid, e.g. the speed of sound in stainless steel is 5096 m/s as opposed to 1430 m/s in water.

As mentioned earlier, stress waves are generated in the solid material due to the pressure pulses imposed by the droplet on the surface. At certain locations in the solid the stress magnitude becomes significant, where initiation of micro-cracks takes place. Two points are found close to the droplet edges where maximum pressure and stress appear and the third location is below the droplet axis due to the axisymmetric shapes of the stress waves as explained by Zhou *et al.* [2]. The generated micro-cracks below the surface contribute to the material spall-off from the surface as discussed earlier. It should be mentioned that the pressure field in the liquid droplet and the stress field in the solid are interdependent only if the solid deformation is not negligible. In such cases, the coupling between the fluid and solid equations is essential to calculate the exact displacement of the solid.

## **1.5 Objectives**

Investigating LIE problems requires understanding the physics behind the high speed droplet impact. To that end, it is crucial to capture the pressure force generated by the impact in order to resolve the transient stresses inside the solid substrate. At low impingement velocities, the fluid can be treated as incompressible without compromising too much accuracy. However, at high impingement velocities, the compressibility effects play an essential role and can no longer be ignored. At such impact conditions, the compressed region in the fluid developed after the impact can only be captured with a compressible solver.

Analytical analysis of high speed droplet impact in 1D and 2D in addition to the numerical modeling with a 2D axisymmetric domain were completed in the past. Although, these models have various limitations and shortcomings, they provide valuable insights to the physics behind the droplet impingement and will be used as benchmarks to validate the current model. 1D and 2D models can only represent liquid columns and cylindrical liquid jets, respectively, instead of a spherical droplet. Furthermore, simulating oblique impacts is not possible with a 2D axisymmetric model. In addition, 2D axisymmetric models are not capable of capturing finger formation after the impact, and would result in a liquid rim. It is important to mention that Liquid Droplet Impingement (LDI) is a three-dimensional phenomenon and a comprehensive 3D model of the droplet impingement at high velocities is still missing in the literature.

Therefore, the main objectives of the present work can be summarized as follows,

- for low impingement velocities in the incompressible regime ( $V_0 < 100$  m/s):
  1. implementing a two-way coupled FSI solver for elastic substrates
  2. validating the two-way coupled FSI solver with ANSYS Workbench
  
- for high impingement velocities in the compressible regime ( $V_0 > 100$  m/s):
  1. modeling single droplet impacts on rigid substrates at normal and oblique angles
  2. modeling droplet impacts onto liquid films
  
- modeling the transient stress in Ti-6Al-4V substrate, under an impact scenario responsible for LIE, with Finite Element Method (FEM), using the pressure history obtained from 3D modeling of compressible droplet impact.

## ***1.6 Thesis outline***

In the following two chapters, the methodology and results are divided into two separate sections, i.e. incompressible and compressible droplet impact. Chapter 2 includes both incompressible fluid and elastic solid equations in addition to their coupling methods. In chapter 3, the compressible fluid equations are presented and the results obtained from 2D axisymmetric and 3D models are discussed. The elastic solid equations are omitted in this chapter to avoid duplication. In the second part of chapter 3, one case has been selected for stress modeling of Ti-6Al-4V substrate that is known to cause LIE. Chapter 4 includes closure, challenges and limitations of this study followed by recommendations for future works. Bibliography, lists all the references cited in this thesis. Finally, the grid sensitivity analysis and additional discussion on the droplet impact onto liquid films are presented in the appendices.

## 2. Incompressible droplet impact

In this chapter the governing equations are presented in detail for an incompressible fluid and elastic solid along with the fluid-solid coupling. The computational domain used for numerical modeling is presented followed by the initial and boundary conditions needed to solve the equations. In addition, the numerical schemes and discretization of the equations are outlined. The results are reported for impact velocities in the incompressible regime over rigid and elastic substrates. The effect of solid elasticity and its importance regarding one-way or two-way coupling between fluid and solid equations is investigated. Finally, the role of compressibility in modeling droplet impingement is studied and the transition to compressible regime is discussed.

## 2.1 Methodology

This section outlines the methodology utilized for solving Navier-Stokes equations in their incompressible form by Finite Volume Method (FVM) and the structural equation by Finite Element Method (FEM).

### 2.1.1 Incompressible fluid equations

Navier-Stokes equations are solved for two incompressible, isothermal and immiscible fluids. The conservation of mass and momentum equations in their transient and incompressible forms are as follows,

$$\nabla \cdot V_f = 0 \text{ in } \Omega_f \quad (2-1)$$

$$\frac{\partial V_f}{\partial t} + \nabla \cdot (V_f \otimes V_f) = \frac{1}{\rho_f} \nabla \cdot \sigma_f + g + F_b \text{ in } \Omega_f \quad (2-2)$$

where  $V_f$  is the fluid velocity vector,  $\rho_f$  is the fluid density,  $g$  and  $F_b$  are the gravitational and other body forces (per unit mass) acting on the fluid.  $\sigma_f$  is the Cauchy stress tensor for a Newtonian fluid, including pressure and viscous terms, defined as,

$$\sigma_f = -p_f I + \mu_f (\nabla V_f + \nabla V_f^T) \quad (2-3)$$

where  $p_f$  is the fluid pressure,  $I$  is the 3 x 3 identity matrix and  $\mu_f$  is the fluid dynamic viscosity.

A single momentum equation is solved for both gas and liquid phases and fluid properties, namely density and viscosity, are calculated for the mixture. The fluid flow is assumed to be laminar, hence, no turbulence model is employed in the solver. The energy equation is not considered in the incompressible model since the temperature variation and the heat conduction during the impact are negligible according to reference [37].

The surface tension force is treated as a pressure gradient across the liquid-gas interface and is calculated per unit volume based on the Continuum Surface Force (CSF) model proposed by Brackbill *et al.* [38]. In CSF model surface tension force is defined as follows.

$$\vec{F}_{ST}(\vec{x}) = \sigma \int_S \kappa(\vec{y}) \hat{n}(\vec{y}) \delta(\vec{x} - \vec{y}) dS \quad (2-4)$$

where  $\sigma$  is the liquid surface tension at the interface,  $\kappa$  is the local curvature,  $\hat{n}$  is the local unit normal to the interface, and  $\delta$  is the Dirac delta function. In equation (2-4),  $S$  corresponds to the area of the free surface.  $\vec{x}$  and  $\vec{y}$  are vectors indicating the location in which the force is calculated and the location of the free surface, respectively. The local curvature,  $\kappa$ , is defined as divergence of the unit normal vector,

$$\kappa = -\nabla \cdot \hat{n} \quad (2-5)$$

The unit normal vector is calculated as follows,

$$\hat{n} = \frac{n}{|n|} \quad (2-6)$$

where  $n$  is the surface normal defined as the gradient of the volume fraction (to be discussed in section 2.1.2),

$$n = \nabla \alpha \quad (2-7)$$

where  $\alpha$  is the liquid volume fraction.

The surface tension force can be expressed as a source term using the divergence theorem and added to the momentum equation,

$$F_{ST} = \sigma \frac{\rho \kappa \nabla \alpha}{\frac{1}{2}(\rho_l + \rho_g)} \quad (2-8)$$

where  $\rho$  is the volume-averaged density computed from equation (2-9),

$$\rho = \alpha\rho_l + (1 - \alpha)\rho_g \quad (2-9)$$

In order to model multi-phase flows, there are currently two general approaches available, namely, Eulerian and Lagrangian methods. In Eulerian methods, the grid is fixed, hence does not move with the interface. On the contrary, in Lagrangian methods the grid moves with the interface velocity. In both approaches the grid may be structured or unstructured. Since the interface between the two phases with different densities is a discontinuity in the computational cells, special resolution is required at the free surface to capture this discontinuity. Eulerian methods have been shown to be more rigorous in resolving the interface between two phases. To that end, there are various Eulerian methods available, e.g. Height Functions, Line Segments, and Marker method. One of the widely used Eulerian methods, which has been shown to be very promising in front-tracking, is Volume of Fluid (VOF) model. VOF is extensively used in capturing the free surface in two-phase flows and is utilized in the current work.

### 2.1.2 Volume of Fluid Model

The VOF model developed by Hirt and Nichols [39] is employed to resolve the droplet interface. In VOF method, a scalar field is defined for volume fraction of the liquid phase and its value depends on the fraction of the cell volume occupied by this phase, indicated by  $\alpha$ ,

$$\begin{cases} \alpha = 0 & \text{Gas phase} \\ 0 < \alpha < 1 & \text{Gas - liquid Interface} \\ \alpha = 1 & \text{Liquid phase} \end{cases} \quad (2-10)$$

The values between zero and one denote the interface between gas and liquid phases. Since the volume fraction represents the volume occupied by the liquid, it should be advected by the flow field at each time step. The following equation governs the liquid advection,

$$\frac{\partial \alpha}{\partial t} + \nabla \cdot (\alpha V_f) = 0 \quad (2-11)$$

Following the advection, the interface is reconstructed using the Piecewise Linear Interface Calculation (PLIC) proposed by Youngs [40]. In PLIC method, the interface is defined at each computational cell by a slope and an intercept as illustrated in figure 2-1. The slope of the interface is calculated based on the volume fractions of the neighboring cells.

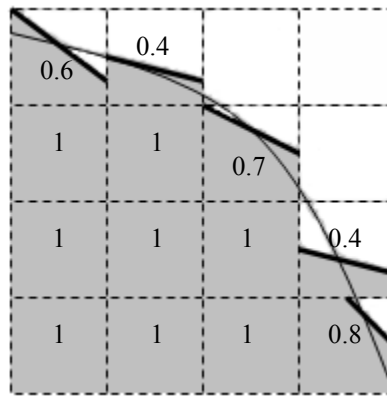


**Figure 2-1: Piecewise Linear Interface Calculation (PLIC) representation of an interface.**

It should be mentioned that the accuracy of the interface reconstruction depends on the mesh resolution in free surface region, which renders VOF method grid dependent. Therefore, a grid sensitivity analysis needs to be carried out to evaluate the dependency of the results on the mesh size.

### 2.1.3 Elastic solid equations

The structural equation to be solved for an elastic and deformable solid is as follows,

$$\frac{\partial V_s}{\partial t} + \nabla \cdot (V_s \otimes V_s) = \frac{1}{\rho_s} \nabla \cdot \sigma_s + g \text{ in } \Omega_s \quad (2-12)$$

where  $\rho_s$  is the solid density,  $V_s$  is the solid velocity, equal to  $V_s = \frac{\partial U_s}{\partial t}$ , and  $U_s$  is the solid displacement.

$\sigma_s$  is Cauchy stress tensor described below,

$$\sigma_s = \frac{1}{J} F (\lambda_s (tr S) I + 2\mu_s S) F^T \quad (2-13)$$

where  $J$  is determinant of  $F$  and  $F$  is the deformation gradient tensor defined as,

$$F = I + \nabla U_s \quad (2-14)$$

$S$  is obtained from St. Venant-Kirchhoff law,

$$S = \frac{1}{2} (F^T F - I) \quad (2-15)$$

$\lambda_s$  and  $\mu_s$  are Lamé coefficients defined below,

$$\mu_s = \frac{E}{2(1+\nu_s)} \quad (2-16)$$

$$\lambda_s = \frac{\nu_s E}{(1+\nu_s)(1-2\nu_s)} \quad (2-17)$$

where  $\nu_s$  and  $E$  are Poisson ratio and Young's modulus, respectively.

### 2.1.4 Fluid-Solid Coupling

In FSI models, the spatial distribution of variables, e.g. stress tensor, needs to be communicated through the interface that is in common between the fluid and solid domains. In addition, the mesh displacement has to be calculated at each time step to determine if there is any deformation in the interface. Two fluid-solid coupling approaches are implemented in this methodology, namely, one-way and two-way coupling methods. The algorithm for both methods is illustrated in figure 2-2.

In the one-way coupling approach, the calculations start with an estimation of the structure displacement and then the fluid mesh is moved accordingly. Next, the fluid equations are solved followed by the structural equation. The solid displacement is determined and used in the next time step to move the fluid mesh. The one-way coupling approach is more time efficient when the solid displacement is very small. In this case, one can assume that the fluid mesh is fixed since the solid is not displaced. In other words, the fluid and solid equations can be decoupled and solved separately. This allows for a much faster calculation and a better mesh resolution in the fluid part, in the cases that grid refinement is necessary.

On the other hand, in the two-way coupling approach, the fluid equations are solved first to obtain the stress tensor at the fluid-solid interface. Then, the structural equation is solved to estimate the solid displacement. This estimation is compared with the displacement from the previous time step, along the interface, with respect to a convergence criterion, set to  $10^{-7}$  in this model, and the global number of time steps. If an internal convergence is achieved for the displacement along the interface, the calculations proceed to the next time step. Otherwise, the displacement is under-relaxed, followed by adjusting the fluid mesh movement, and fed back to the fluid solver to repeat the fixed-point iteration loop until the displacement convergence is

satisfied. In general, this approach is more accurate when solid deflection is considerable. However, it is much more demanding in terms of computational time since both sets of equations need to be solved together and an internal convergence should be reached during all time steps.

The coupling between the fluid and solid domains is enabled with the stress and velocity constraints at their interface,  $\Gamma_0 = \Omega_s \cap \Omega_f$ , over all time steps. The force balance and no-slip condition on the interface ( $\Gamma_0$ ) imply,

$$\sigma_s n = \sigma_f n \text{ on } \Gamma_0 \quad (2-18)$$

and,

$$V_s = V_f \text{ on } \Gamma_0 \quad (2-19)$$

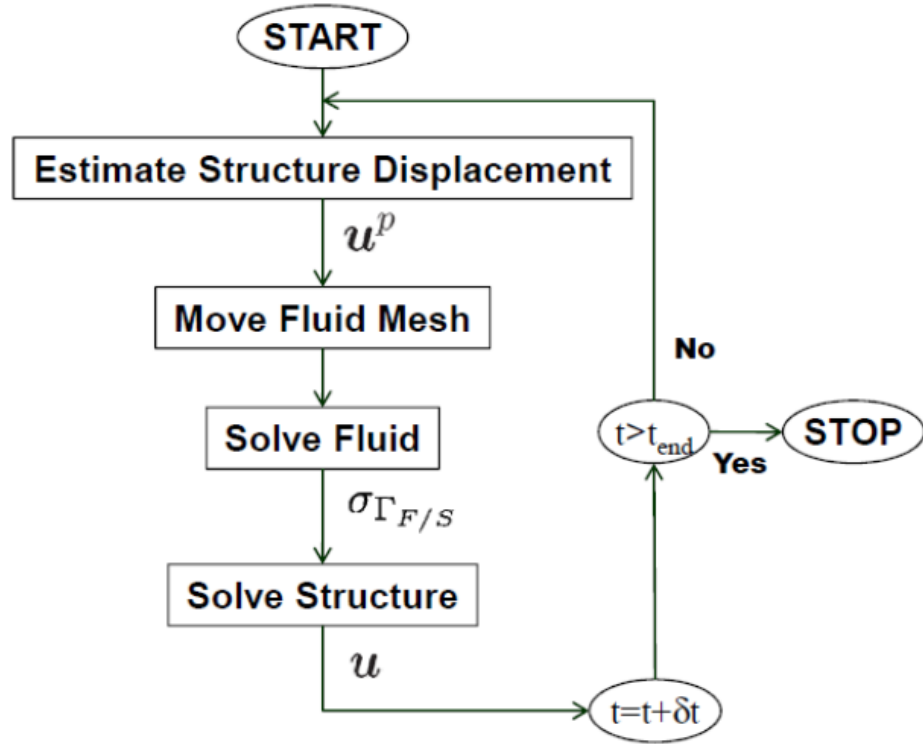
where  $n$  is the unit vector normal to the interface,  $\Gamma_0$ . The detailed coupling formulation can be found in reference [41].

To present the stress results, the equivalent stress will be utilized, which is defined based on von Mises criterion in 3D, as follows,

$$\sigma_{Eq.} = \sqrt{\frac{1}{2} \left[ (\sigma_{11} - \sigma_{22})^2 + (\sigma_{11} - \sigma_{33})^2 + (\sigma_{22} - \sigma_{33})^2 + 6(\sigma_{12}^2 + \sigma_{23}^2 + \sigma_{13}^2) \right]} \quad (2-20)$$

where  $\sigma_{ij}$  is the component of the stress tensor defined in equation (2-13). For convenience, the equivalent stress will be simply referred to as stress ( $\sigma$ ) in some of the figures.

(a)



(b)

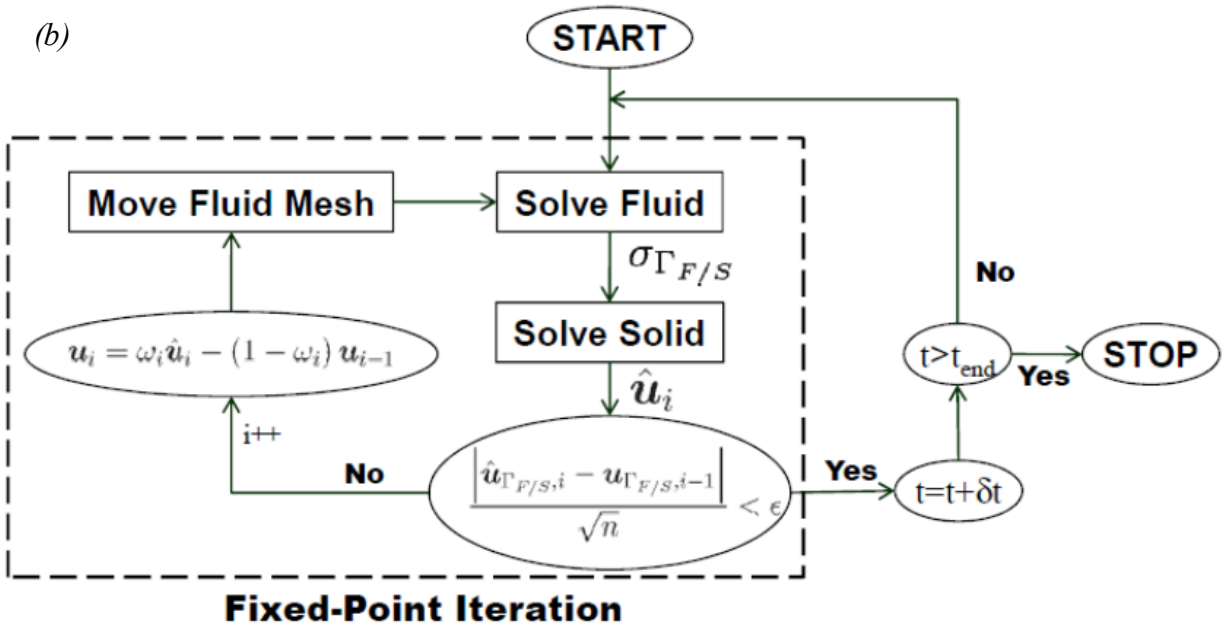


Figure 2-2: Numerical algorithm for (a) one-way coupling, (b) two-way coupling approaches.

### 2.1.5 Computational domain and material properties

The computational domain for the 2D axisymmetric model is illustrated in figure 2-3. The width of both domains is eight times the droplet radius and the heights of fluid and solid domains are  $4R$  and  $10R$ , respectively. The gravitational force is exerted in the direction of droplet impingement. The fluid domain consists of air and water phases and the fluid properties at ambient conditions are summarized in table 2-1.

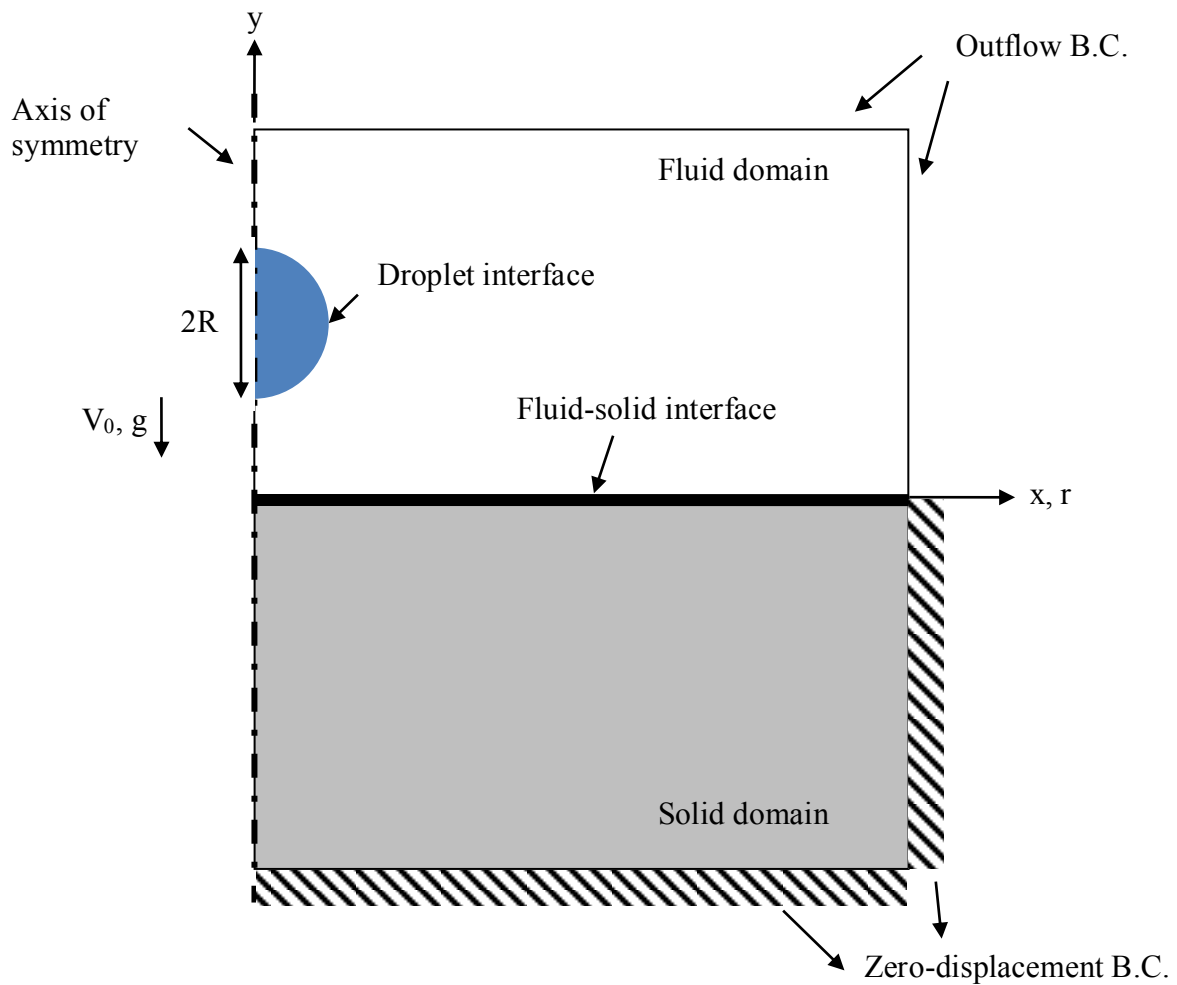


Figure 2-3: Computational domain for 2D axisymmetric FSI model.

<b>Fluid properties</b>		
Phase	Air	Water
Density (kg/m <sup>3</sup> )	1.2	1000
Kinematic viscosity (m <sup>2</sup> /s)	1.48e-05	1e-06
Surface tension (N/m)	0.073	

**Table 2-1: Fluid properties for air and water at atmospheric condition.**

The solid material is a Titanium alloy, namely isotropic Ti-6Al-4V, which is widely utilized in gas turbine manufacturing, and its properties are tabulated in table 2-2.

<b>Substrate material: isotropic Ti-6AL-4V</b>		
<b>Young's Modulus</b>	<b>Poisson's Ratio</b>	<b>Bulk Modulus</b>
113.8 GPa	0.342	120.04 GPa
<b>Tensile Yield Strength</b>	<b>Tensile Ultimate Strength</b>	<b>Shear Modulus</b>
0.88 GPa	0.95 GPa	42.4 GPa

**Table 2-2: Structural properties of isotropic Ti-6Al-4V.**

### **2.1.6 Boundary and initial conditions**

As presented in figure 2-3, the fluid and solid domains share the same base, identified as the fluid-solid interface, with boundary conditions governed by equations (2-18) and (2-19). Therefore, no-slip condition is imposed on the interface between the fluid and solid. Outflow boundary condition is applied to all the fluid boundaries that are not in contact with the solid. The solid is free to move except at its edges which are fixed to a wall. Hence, zero displacement and stress free boundary conditions are used for the solid boundaries at the edges and fluid-solid

interfaces, respectively. Initially, the fluid domain is filled with air. At the beginning of each computation, the droplet is patched in the fluid domain with the desired size and velocity. The computation for the rest of the fluid cells starts with zero for all the variables.

### 2.1.7 Numerical schemes and discretization

The Pressure-Implicit with Splitting of Operators (PISO) method is used for pressure-velocity coupling in transient calculations. The integral forms of fluid equations are discretized over each control volume and solved for a fixed system of grids in a segregated manner. The solution is then obtained by using a time marching scheme based on the given initial condition. The Gaussian integration method is used for summation of the values on cell faces interpolated linearly from cell centers. The time scheme is first-order implicit based on Euler and is bounded. The gradient schemes are Gauss linear with central differencing. The divergence schemes are also Gaussian with an upwind discretization for all the transport equations except for volume fraction flux which is second-order accurate in space and unbounded. Finally, the uncorrected Gauss linear scheme is utilized in discretizing the Laplacian equation.

The mesh is uniformly distributed in both domains with the same grid size of  $0.04R$ . The time step during for all the advective fluxes in transport equations is different from the one used in VOF calculations. The time step in VOF is adaptive and depends on the Courant–Friedrichs–Lewy (CFL) condition defined as,

$$CFL = \frac{\Delta t V_f}{\Delta x} \quad (2-21)$$

The maximum CFL is set to 0.1 during the computations to constrain the adaptive time step. This requirement ensures that the liquid advection through one cell is less than 10% at every time step

and the initial time step is determined based on the impact velocity and grid size, depending on the impact condition.

OpenFoam, an open-source computational code, is used for programming the solver. The fluid and solid parts are solved with `interFoam` and `stressedFoam`, respectively. The default individual solvers are adapted to communicate with each other along the fluid-solid interface. The IDs of the nodes where the fluid and solid cells overlap are stored in a new file and used to deform the computational mesh when the solid displacement occurs. The convergence threshold for the internal fixed-point iteration in the two-way coupling algorithm is set to  $10^{-7}$ . In OpenFoam, all the equations are always solved in three dimensions and a 2D axisymmetric mesh is simply a  $5^\circ$  section of a full cylinder with flat sides and one cell in lateral direction, which results in a wedge. In addition, a commercial FEM solver, namely ANSYS Workbench, is used to validate the two-way-coupled FSI solver and resolve the stresses in the substrate for the one-way coupling approach.

## 2.2 Results and discussion

The impact of incompressible droplets on rigid substrates is discussed first. To that end, only fluid domain is considered and the solid domain is not modeled, since it is assumed to be rigid. Afterwards, the results obtained from incompressible FSI model, composed of incompressible fluid model and elastic solid solver with two-way coupling, for impact velocities in incompressible regime are presented. The effect of substrate elasticity, as the basis for one-way or two-way coupling approach, is discussed. The pressure and stress history in fluid and solid domains, respectively, are presented. Finally, the threshold for incompressibility and the transition to compressible flow regime based on the impingement velocity is quantified.

In presenting some of the results, the variables are normalized with respect to some reference values, outlined in table 2-3.  $R$  is the droplet radius,  $V_0$  is the impact velocity and  $p_{wh}$  is the water hammer pressure defined in equation (1-1).  $\rho_0$  is the density of undisturbed water ( $1000 \text{ kg/m}^3$ ) and  $T_0$  is the initial or ambient temperature equal to  $300\text{K}$ . As a convention in this thesis, “\*” denotes a dimensionless variable.

Dimensionless variable (*)	Notation	Definition
Dimensionless length (x, r, y, z)	$l^*$	$l^*=l/R$
Dimensionless time	$t^*$	$t^*=tV_0/2R$
Dimensionless velocity	$V^*$	$V^*=V/V_0$
Dimensionless pressure	$p^*$	$p^*=p/p_{wh}$
Dimensionless density	$\rho^*$	$\rho^*=\rho/\rho_0$
Dimensionless temperature	$T^*$	$T^*=T/T_0$
Dimensionless stress	$\sigma^*$	$\sigma^*=\sigma/p_{wh}$

Table 2-3: Definition of dimensionless variables.

### 2.2.1 Incompressible impact on rigid substrates

Figure 2-4 presents the contours of pressure (left) and velocity (right), cropped with the droplet interface, for an impact of a 500- $\mu\text{m}$  droplet and velocity of 100 m/s over various times. The flow streamlines and velocity vectors, colored by the velocity magnitude with the same scale as figure 2-4, are illustrated in figure 2-5 over the same time steps but in an area closer to the substrate. It should be noted that the size of all the velocity vectors are uniform and their magnitude is indicated by their coloring and not their sizes.

As it can be seen in the pressure and velocity contours at  $t^*=0$ , figure 2-4 (a), the pressure starts to rise when the droplet touches down on the surface and a stagnation flow develops in the liquid upon the impact. As the droplet moves downward, the air is pushed outward from beneath, as shown by the streamline and the velocity vectors in figure 2-5(a), with the maximum velocity close to the impact point. As the droplet begins to spread over the surface, the high pressure region penetrates further into the droplet and the stagnation region grows in size, illustrated in figure 2-5 (b). At  $t^*=0.01$ , a high velocity region is observed in the droplet periphery in addition to the radial flow around the stagnation area inside the droplet (figure 2-4 (b)).

At  $t^*=0.02$ , the high pressure concentration starts to move outward, toward the contact line, as shown in figure 2-4 (c). The formation of a lateral jet begins since there is a large difference between the pressure inside the droplet behind the contact line and the surrounding air, attached to the solid substrate. At this instant, a vortex is generated in the air next to the droplet edge due to the radial motion of fluid particles toward the still air (figure 2-5 (c)). As it can be seen in figure 2-4 (d), the lateral jetting becomes more apparent at  $t^*=0.03$  and the rotational flow in the air causes an upward motion in the liquid particles, where the maximum velocity is observed right behind the jet (figure 2-5 (d)).

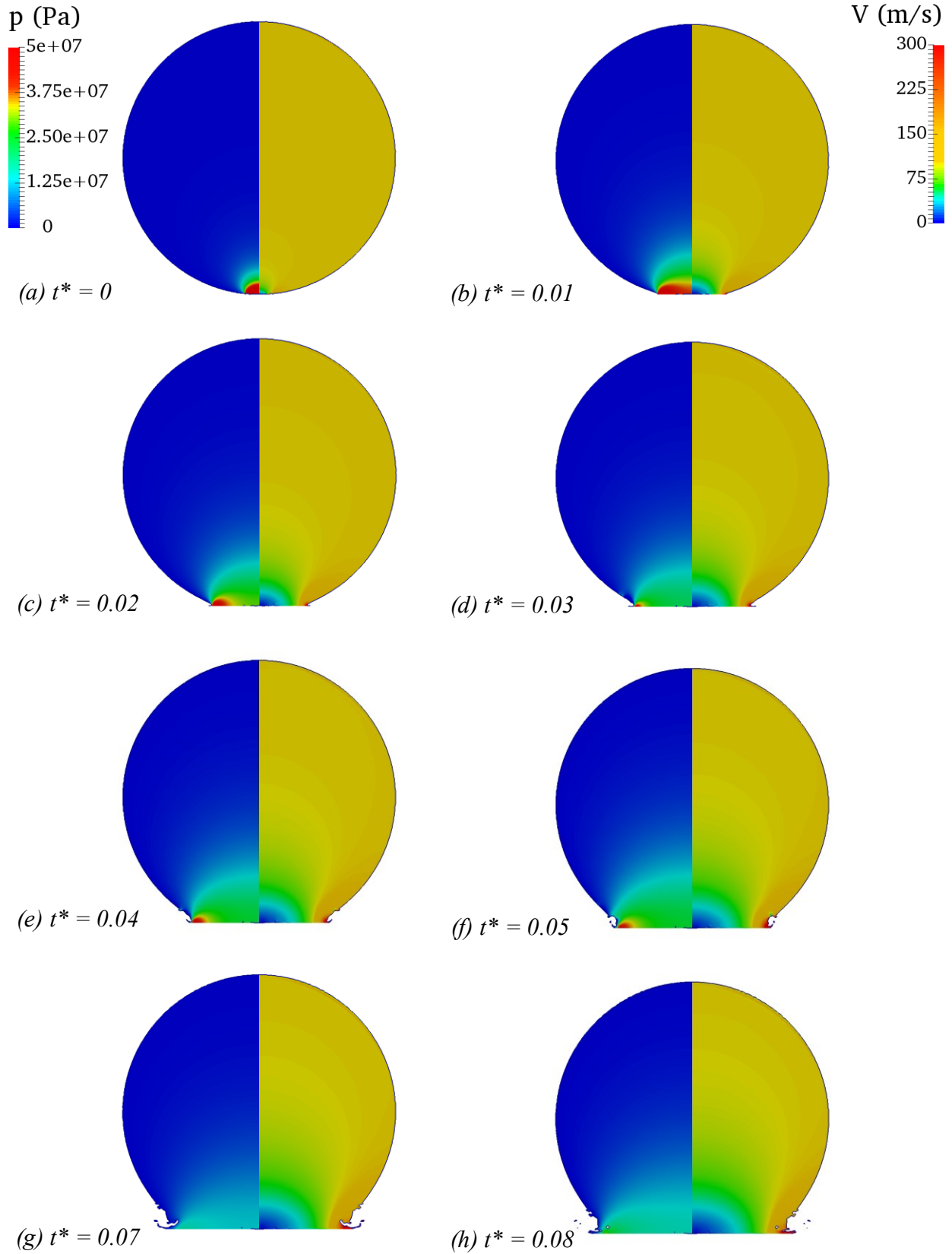
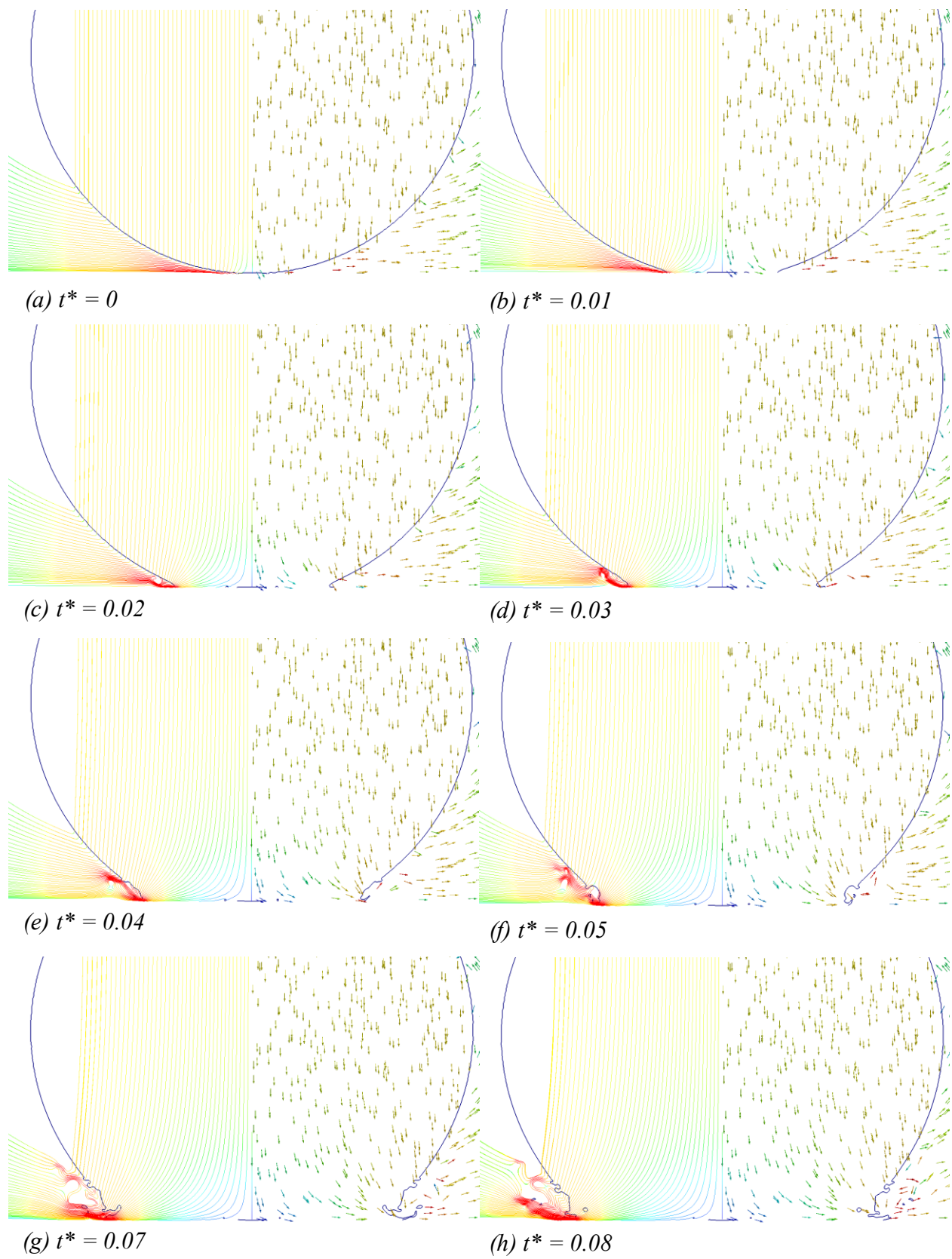


Figure 2-4: Contours of pressure (left) and velocity (right),  $D=500 \mu\text{m}$ ,  $V_0=100 \text{ m/s}$ , rigid substrate.



**Figure 2-5: Streamlines (left) and velocity vectors (right),  $D=500 \mu\text{m}$ ,  $V_0=100 \text{ m/s}$ , rigid substrate.**

At  $t^*=0.04$ , a rim is formed around the droplet periphery and a secondary vortex starts to form in the surrounding air leading to the formation of a dent above the rim, as shown in figures 2-4 and 2-5 (e). As it can be seen in figures 2-4 and 2-5 (f), the depth of the hollow in the droplet increases and a ligament is detached from the rim due to the surface tension energy. After  $t^*=0.07$ , the high pressure region starts to dissipate inside the droplet (figures 2-5 (g) and (h)) and the remaining ligament continues to elongate (figure 2-5 (g)), until it experiences further breakup forming smaller particles, as illustrated in figure 2-5 (h).

In order to quantify the exact pressure and velocity magnitude over these time steps, the dimensionless pressure is plotted along the radial (r-axis) and axial (y-axis) directions in figures 2-6 and 2-7, respectively. Figures 2-8 and 2-9 display the variation of the dimensionless radial velocity ( $V_r^*$ ) over the r-axis and dimensionless vertical velocity ( $V_y^*$ ) over the y-axis, respectively. Finally, the liquid volume fraction is plotted along the r-axis over the solid surface and droplet center axis ( $r^*=0$ ) in figures 2-10 and 2-11, respectively. It should be mentioned that the water hammer pressure calculated from equation (1-1) for this impact condition is equal to 143 MPa.

As it is shown in figure 2-6, the dimensionless pressure at  $t^*=0$  is equal to 0.586 (83.8 MPa) which is lower than the peak pressure,  $p^*=0.714$  (102.1 MPa), located at a radial distance of  $r^*=0.064$  (16  $\mu\text{m}$ ) from the axis. A close examination of the volume fraction at this time step in figures 2-10 and 2-11, reveals that only 25% of the computational cells underneath the droplet are filled with liquid. This observation conveys the entrapment of an air layer with a height of  $y^*=0.016$  corresponding to 4  $\mu\text{m}$ , right at the impact point. It should be mentioned that the grid size for this case is 1  $\mu\text{m}$ , which has enough resolution to capture the air bubble formation. However, further grid refinement in this region is required to calculate the exact air layer height.

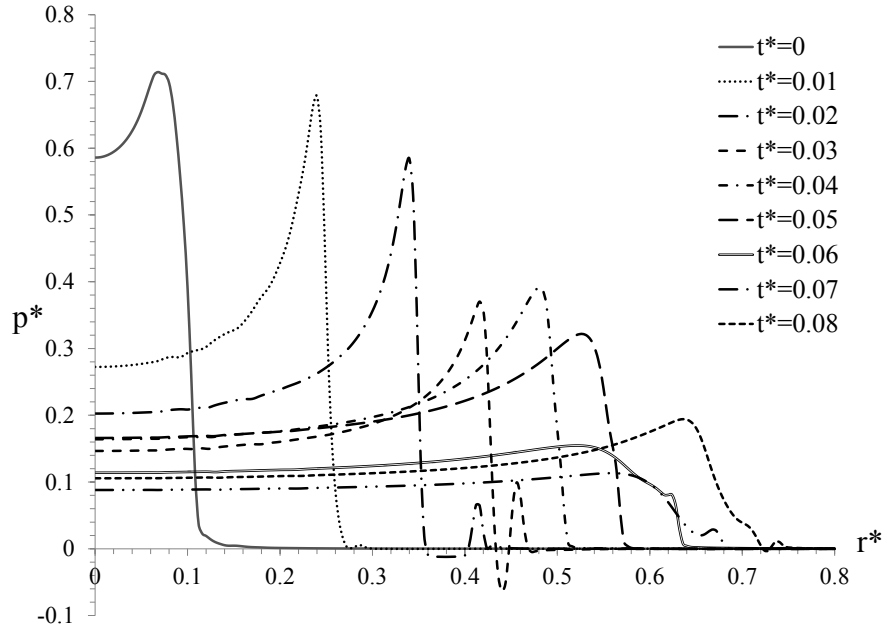


Figure 2-6: Dimensionless pressure along r-axis,  $D=500 \mu\text{m}$ ,  $V_0=100 \text{ m/s}$ , rigid substrate.

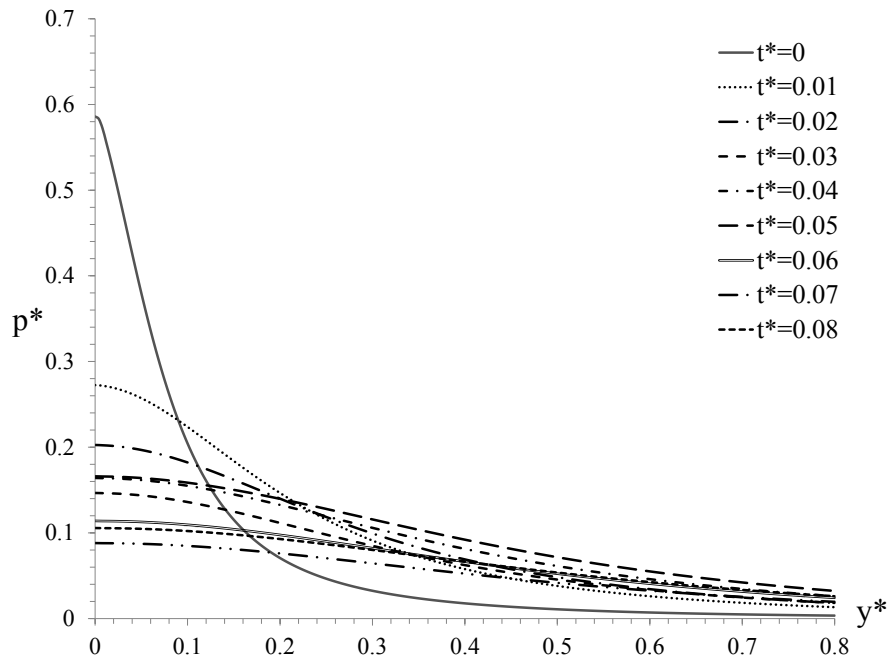


Figure 2-7: Dimensionless pressure along y-axis,  $D=500 \mu\text{m}$ ,  $V_0=100 \text{ m/s}$ , rigid substrate.

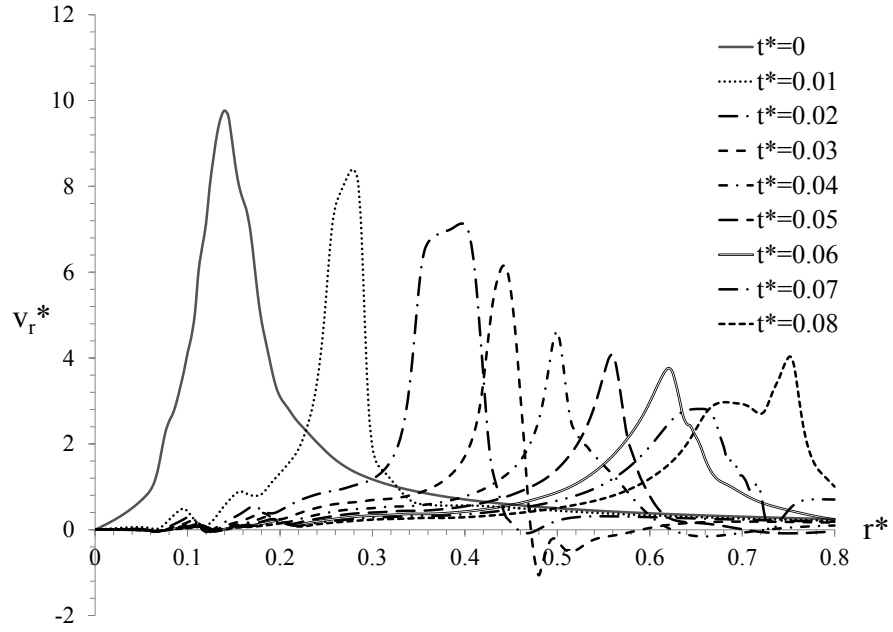


Figure 2-8: Dimensionless radial velocity along  $r$ -axis,  $D=500 \mu\text{m}$ ,  $V_0=100 \text{ m/s}$ , rigid substrate.

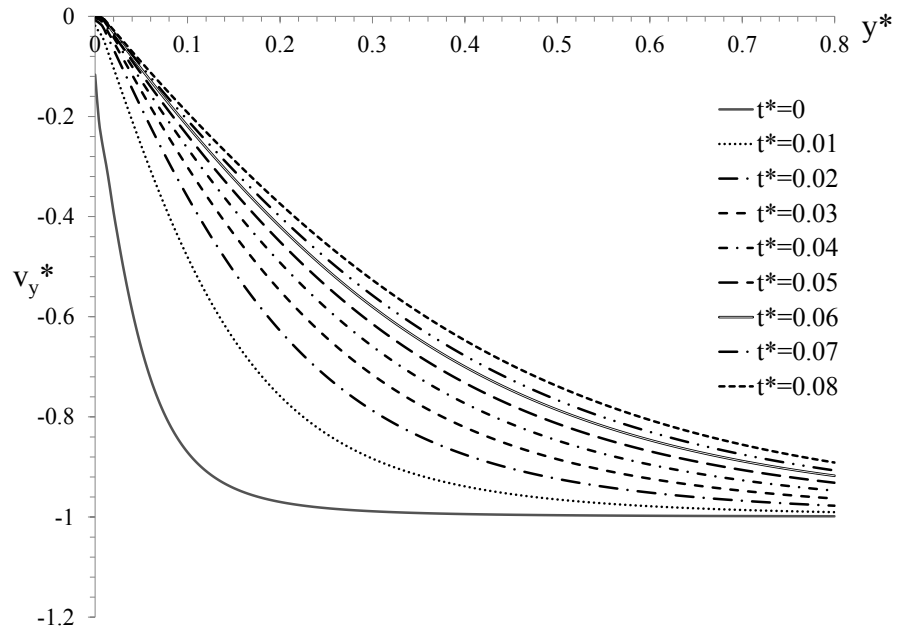


Figure 2-9: Dimensionless vertical velocity along  $y$ -axis,  $D=500 \mu\text{m}$ ,  $V_0=100 \text{ m/s}$ , rigid substrate.

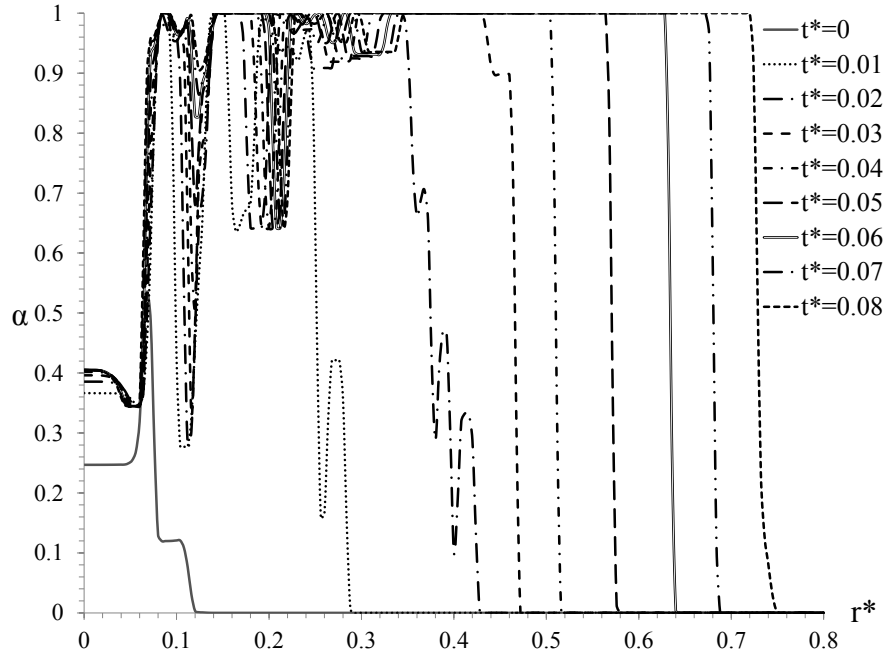


Figure 2-10: Liquid volume fraction along r-axis,  $D=500 \mu\text{m}$ ,  $V_0=100 \text{ m/s}$ , rigid substrate.

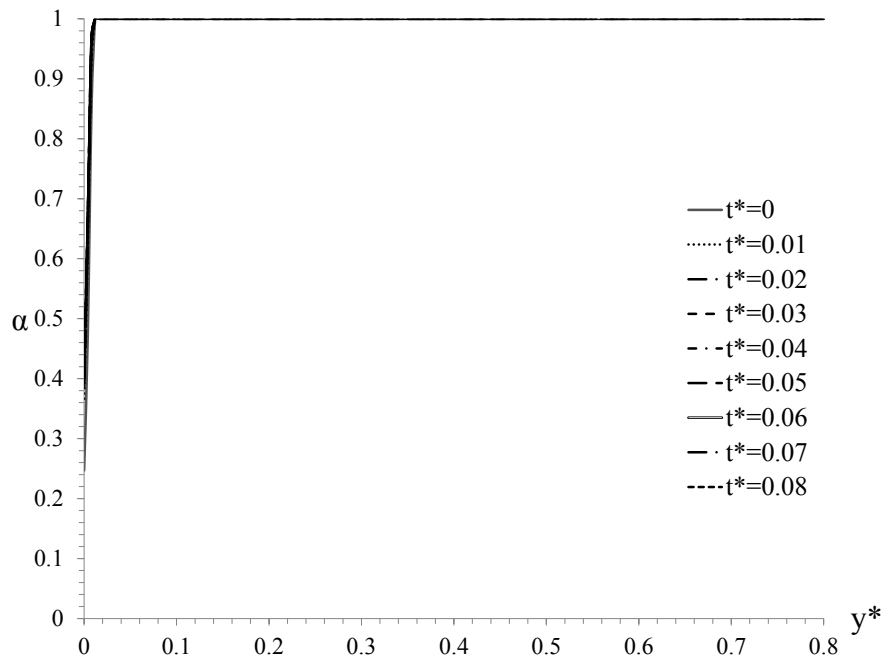


Figure 2-11: Liquid volume fraction along y-axis,  $D=500 \mu\text{m}$ ,  $V_0=100 \text{ m/s}$ , rigid substrate.

Figures 2-8 and 2-9 indicate that the radial and vertical velocities around the impact point are equal to zero, which confirm the formation of a stagnation region mentioned earlier. In addition, as illustrated by the volume fraction graphs, figures 2-10 and 2-11, the air cushion formed upon the impact, which remains stationary at later time steps, has a height of  $y^*=0.016$  (4  $\mu\text{m}$ ) and a radius of  $r^*=0.06$  (15  $\mu\text{m}$ ). Furthermore, at the droplet periphery, the air escaping the impact point reaches a radial velocity of  $V_r^*=9.65$  (965 m/s) at  $r^*=0.144$  (36  $\mu\text{m}$ ), which is significantly higher than the initial impingement velocity of 100 m/s. It should be noted that the volume fraction graph along r-axis, figure 2-10, shows that there is no liquid at  $r^*=0.144$ , confirming the presence of 100% air at  $t^*=0$ .

At  $t^*=0.01$ , the pressure is still high close to the droplet edge ( $p^*=0.678$  at  $r^*=0.24$ ), but its magnitude is reduced by half at the center ( $p^*=0.272$ ). Moreover, the radial velocity is still high behind the droplet edge at  $r^*=0.276$  with a magnitude of  $V_r^*=8.35$ . The vertical velocity remains zero at the impact point and its value decreases over time as the droplet continues its downward motion toward the surface, where its maximum magnitude occurs at liquid particles farther from the surface ( $y^* > 0.8$ ).

At  $t^*=0.02$  and  $0.03$ , a negative pressure and radial velocity can be noticed in figures 2-6 and 2-8, respectively. This is due to the formation of a vortex discussed earlier and displayed in figures 2-4 and 2-5. A rotational flow is generated at these time steps since the high velocity air behind the droplet, that is spreading outward, meets the still air in the surrounding. As a result, a reverse flow is formed with the air moving toward the droplet axis with a velocity of  $V_r^*=-1.06$  at  $r^*=0.48$ , leading to the upward motion of the lateral jet at  $t^*=0.04$ . As the droplet continues to spread over the surface, the peak pressure and maximum radial velocity move outward from the center axis and their magnitudes degrade over time and eventually the pressure curve flattens.

As a parametric study, the same analysis is carried out for a 500- $\mu\text{m}$  droplet with impingement velocities between 50 and 100 m/s in increments of 10 m/s. The pressure is extracted over the solid surface along the r-axis and the maximum pressure is calculated at each time step. The maximum dimensionless pressure, between all the time steps, is plotted for various impact velocities in figure 2-12 with a linear fit as follows,

$$p_{\max}^* = 0.008V_0 + 0.0024 \quad (2-22)$$

Equation (2-22) is consistent with Bernoulli's equation in a sense that, for an incompressible flow, the pressure is proportional to the square of velocity. It should be noted that  $p_{\max}^*$  is defined as the maximum pressure divided by water hammer pressure ( $p_{wh} = \rho_0 V_0 C_0$ ).

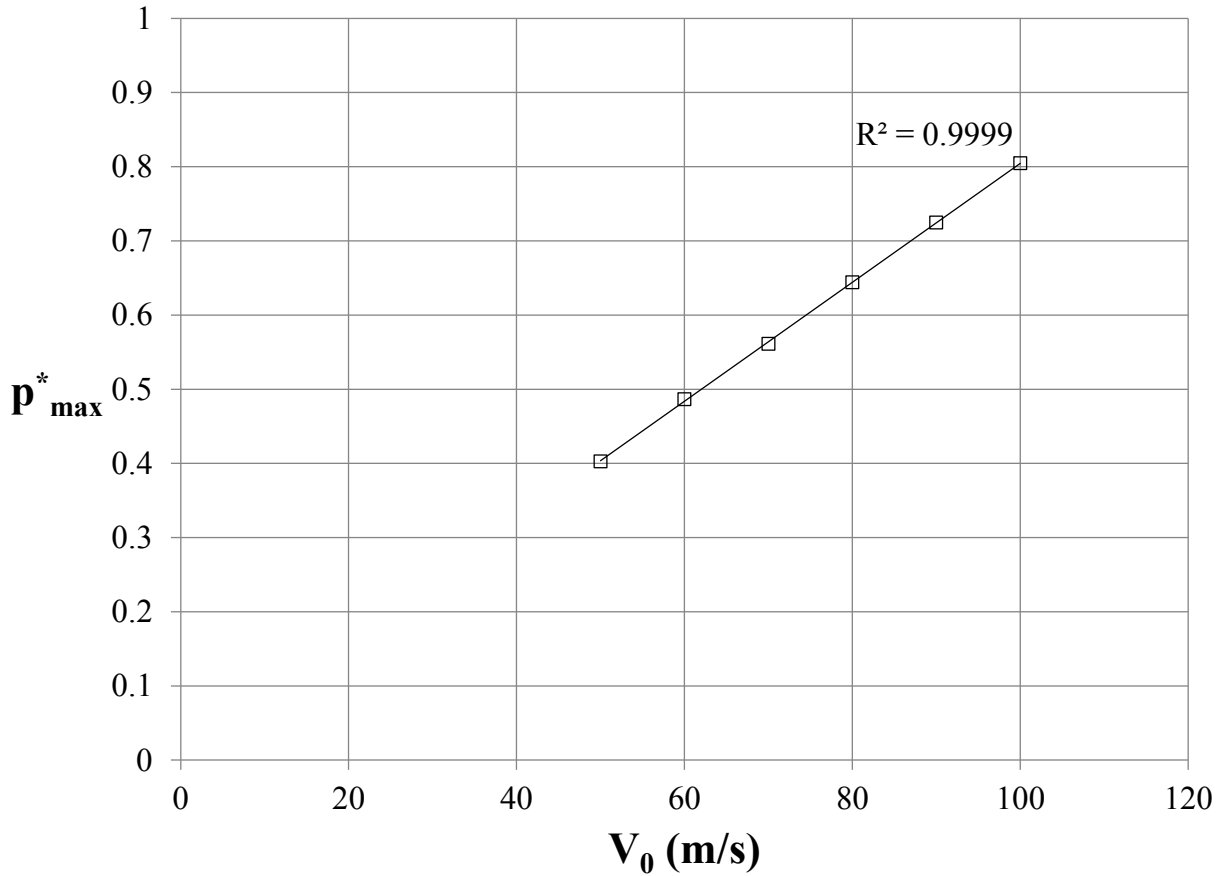


Figure 2-12: Maximum dimensionless pressure vs. impact velocity, D=500  $\mu\text{m}$ , rigid substrate.

## 2.2.2 Incompressible impact on elastic substrates

The results obtained from incompressible fluid solver coupled with the elastic structural model using a two-way coupling scheme for the same impact scenario ( $D=500 \mu\text{m}$ ,  $V_0=100 \text{ m/s}$ ) are reported in this section. This requires that both fluid and solid domains to be solved simultaneously and the variables on the fluid-solid interface to be exchanged at each time step until internal convergence is achieved. The variation of the maximum pressure in the fluid and maximum stress in the solid along the interface (r-axis) are illustrated in figure 2-13. As it can be seen in the graph, the dimensionless pressure and stress display a similar behavior and reach a maximum value of 0.75 and 0.62, respectively.

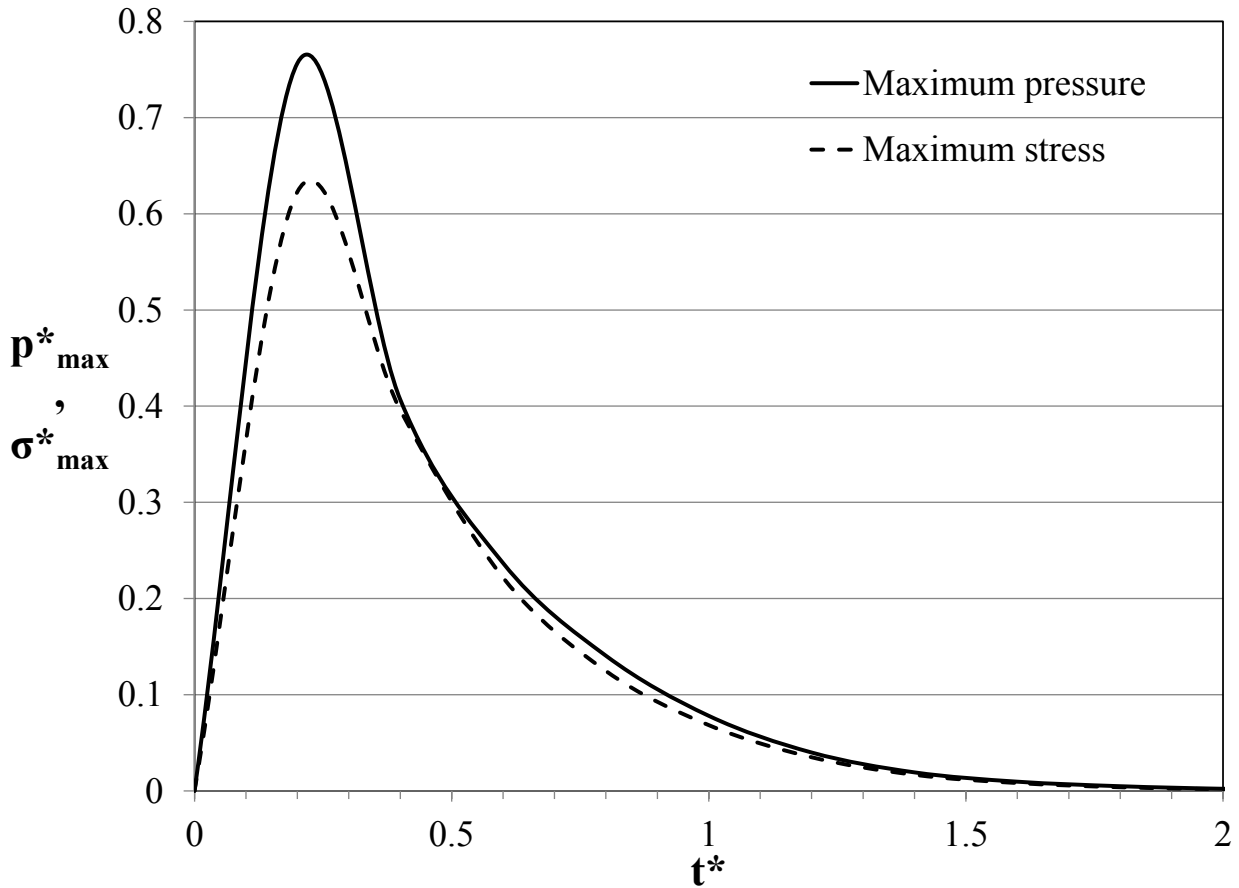


Figure 2-13: Maximum pressure and stress profile along the interface over time,  $D=500 \mu\text{m}$ ,  $V_0=100 \text{ m/s}$ .

### 2.2.3 Validation with ANSYS Workbench

The incompressible fluid solver is used to model the droplet assuming that the solid is rigid. Hence, the fluid solver is decoupled from the solid solver. The generated pressure is then extracted from the fluid simulation results and imposed as a boundary condition on the solid plate. The transient structural equation for an elastic solid is then solved in ANSYS workbench using the Johnson-Cook material behavior model for Ti64. This approach is used in order to validate the FSI results and compare the two cases for one-way and two-way coupling methods. The predicted pressure upon impact onto the rigid solid is approximated by a triangular pulse, shown in figure 2-14. Afterwards, the triangular pressure pulse is imposed on a square flat substrate with dimensions of 2 mm by 2 mm and a thickness equal to 2.5 mm. The transient structural equations for an elastic substrate are solved using the approximated pressure distribution as the boundary condition.

Figure 2-15 illustrates the comparison between two-way coupling modeling in FSI solver and one-way coupling method done in ANSYS. It can be inferred that the stress field in the solid shows a similar behavior compared to the pressure distribution presented in figure 2-13. The peak stress predicted by using one-way coupling is slightly lower compared to two-way coupling approach, which is the side effect of decoupling the two solvers. Moreover, a stress residual is observed after  $t^*=2$  for the case of one-way coupling, which is due to the triangular approximation of the imposed pressure. In general, the one-way coupling method is capable of predicting the transient stress with acceptable accuracy. Furthermore, it confirms that the modeling results obtained from the two-way coupled FSI solver agree well with ANSYS modeling for an elastic substrate.

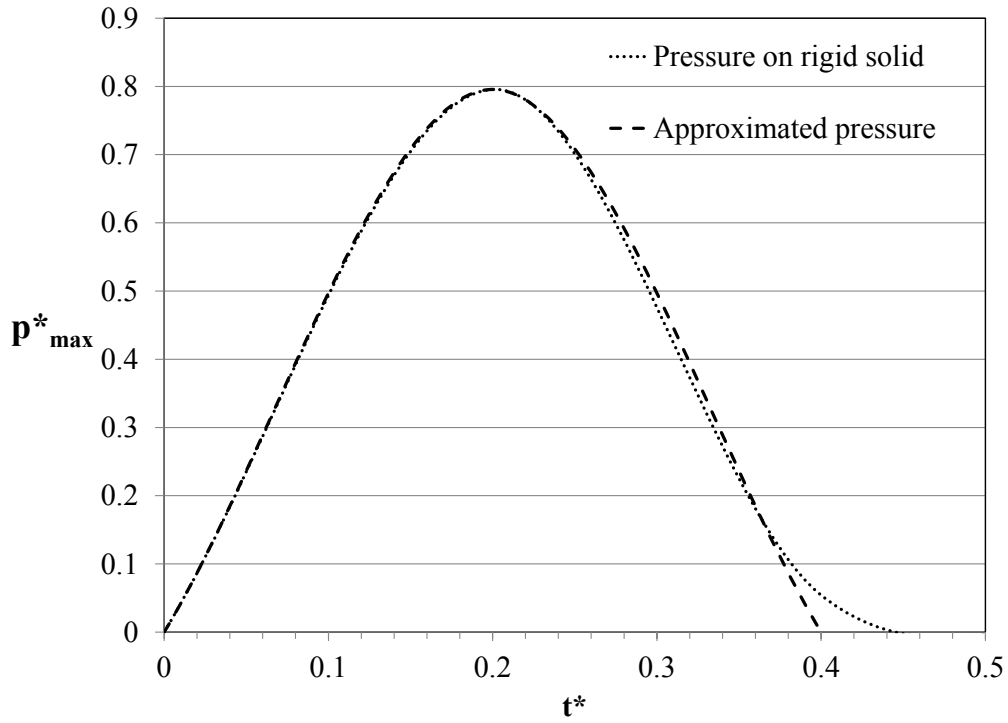


Figure 2-14: Pressure approximation with a triangular pulse for validation with ANSYS.

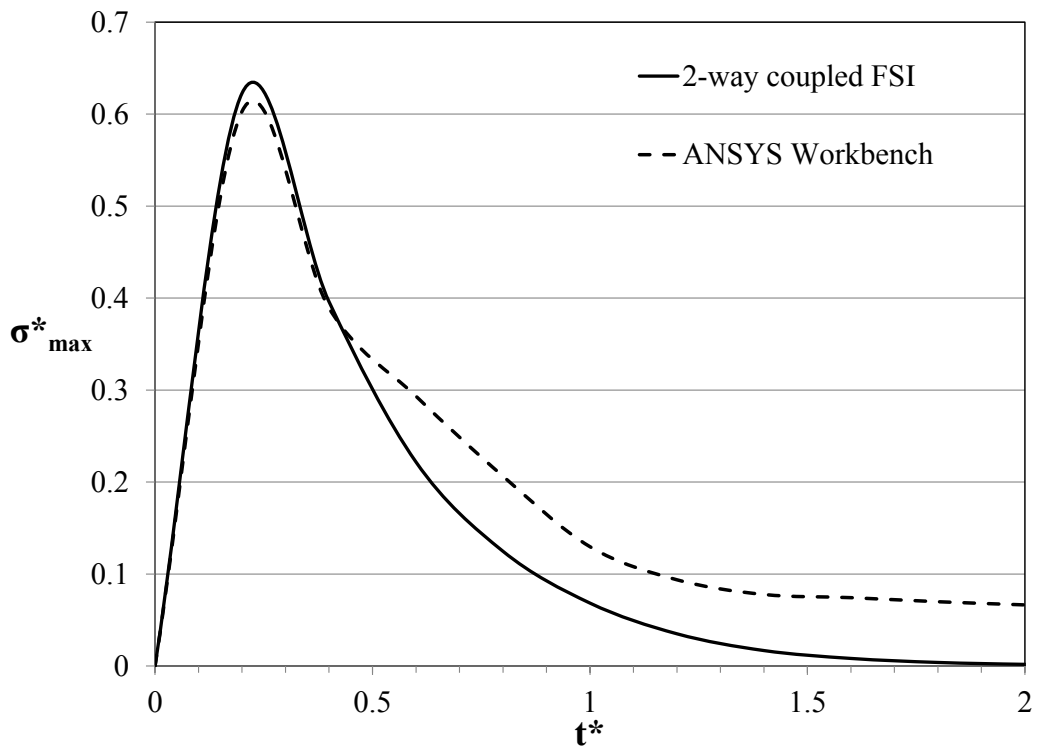


Figure 2-15: Incompressible FSI solver validation with ANSYS,  $D=500 \mu\text{m}$ ,  $V_0=100 \text{ m/s}$ .

## 2.2.4 Solid elasticity effect

In order to investigate the effect of solid elasticity on the results, two cases are considered with the same impact conditions, one on a rigid substrate and the other one on an elastic plate. The maximum dimensionless pressure generated on the fluid-solid interface is compared against each other over dimensionless time, displayed in figure 2-16. It can be inferred from this comparison that the maximum pressure generated upon impact is slightly higher on a rigid solid, with less than 6% variation. Therefore, it would be a reasonable assumption that the solid elasticity has very little influence on the pressure build-up in the fluid and the consequent stress in the solid, since the two are closely connected. As a result, the fluid and solid equations can be decoupled and solved in a segregated manner to reduce the computational time significantly without losing much accuracy.

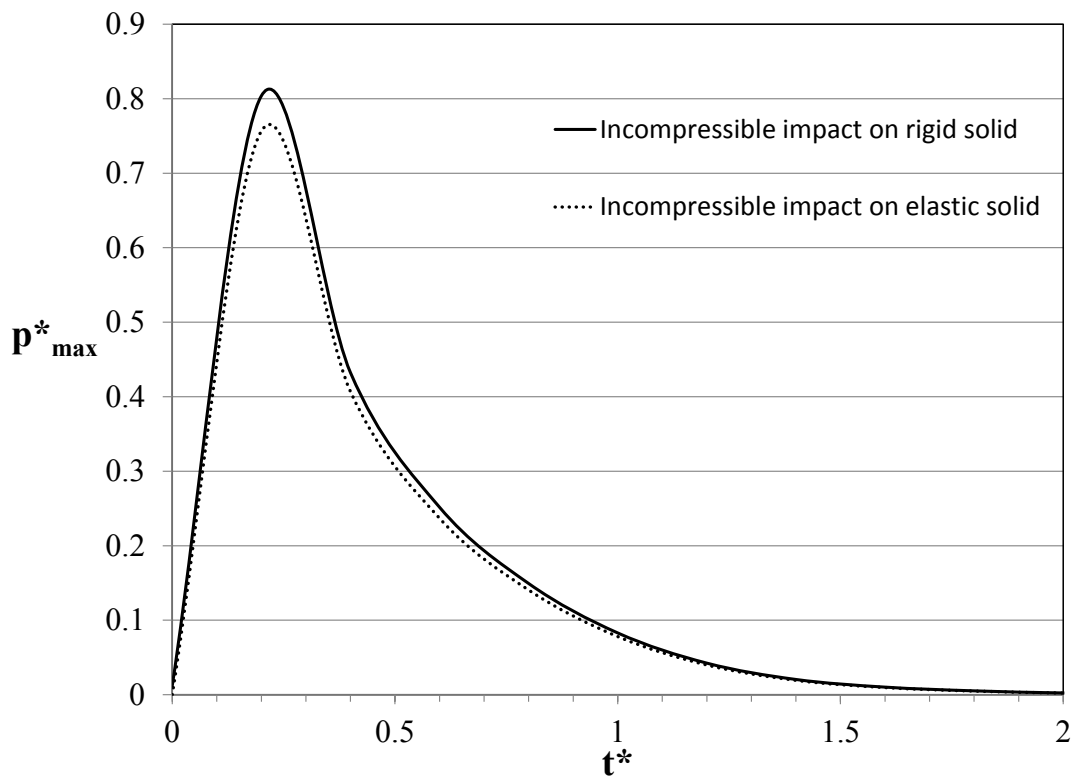


Figure 2-16: Effect of solid elasticity on maximum pressure,  $D=500 \mu\text{m}$ ,  $V_0=100 \text{ m/s}$ .

### 2.2.5 Fluid compressibility effect

It has been shown in the literature [6] that the compressibility effects become important around an impact velocity of 50 m/s and can no longer be ignored for impingement velocities above 100 m/s. Therefore, the impact velocities below this threshold can be modeled with an incompressible solver with an acceptable accuracy. To further validate this assumption with the current model, a one-to-one comparison between an incompressible and compressible solver is carried out for the same impingement velocity of 100 m/s over a rigid solid with a droplet size of 500  $\mu\text{m}$  (the formulation for the compressible solver is outlined in the next chapter).

The dimensionless pressure is plotted over the r-axis at the time step when the peak pressure occurs for the two solvers in figure 2-17. It should be mentioned that the peak pressure occurs at different computational times in the two models. Hence, the presented graphs do not correspond to the same time step. As it can be seen, the peak pressure calculated by the compressible solver is more than twice larger than the one obtained from the incompressible solver, with a value of  $p^*=1.63$  as opposed to  $p^*=0.805$ , respectively. Thus, it is crucial to take into account the fluid compressibility when studying LIE problems, particularly for the velocities above 100 m/s.

Figures 2-18 and 2-19 present the maximum dimensionless stress and solid deflection normalized with respect to the droplet diameter ( $\delta/D$ ) over dimensionless time, respectively. These results suggest that the peak transient stress in the solid predicted by the compressible solver is 45% higher than the one calculated by the incompressible solver with  $\sigma^*_{\text{max}}$  equal to 1.09 and 0.6, respectively. In addition, the maximum stress in the solid is observed at a later time in the case of a compressible impact due to the formation of a compressed region and lateral jetting (to be discussed in chapter 3). The maximum normalized deformation ( $\delta/D$ ) of the

substrate computed from the compressible and incompressible solvers is equal to 0.00056 and 0.00031, respectively, corresponding to 0.28  $\mu\text{m}$  and 0.15  $\mu\text{m}$ , respectively. The sub-micron values for the deformation indicate that the solid deflection with respect to the droplet size is negligible at this impingement velocity, i.e. 100 m/s, and would not affect the stress history in the solid if it were to be ignored. In other words, this observation supports the assumption of a rigid solid due to zero deformation. Therefore, there is no need to compute the mesh movement in the solid domain and feed it back to the fluid domain at each iteration. This reduces the two-way coupling to the one-way coupling mechanism and the overall computational time. It should be mentioned that this assumption will be revisited for higher impingement velocities, e.g. 350 m/s, and the solid deformation scale will be discussed in section 3.3 for such velocities.

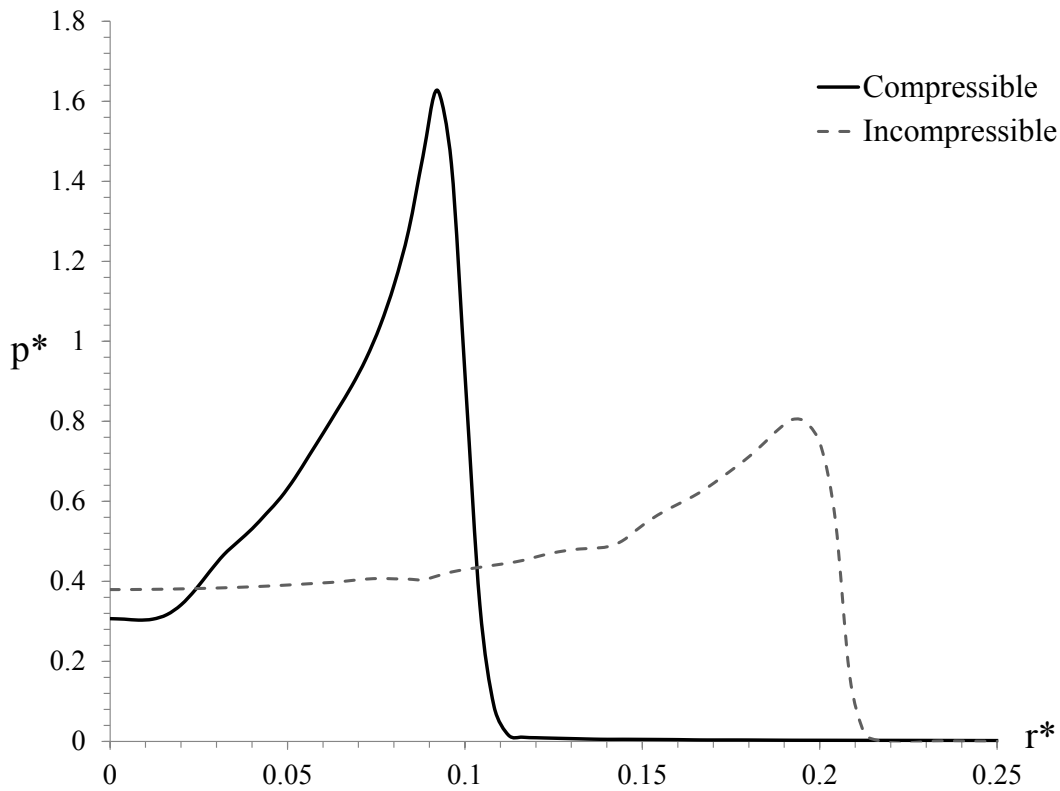


**Figure 2-17: Comparison between compressible and incompressible solvers,  $D=500 \mu\text{m}$ ,  $V_0=100 \text{ m/s}$ , rigid substrate.**

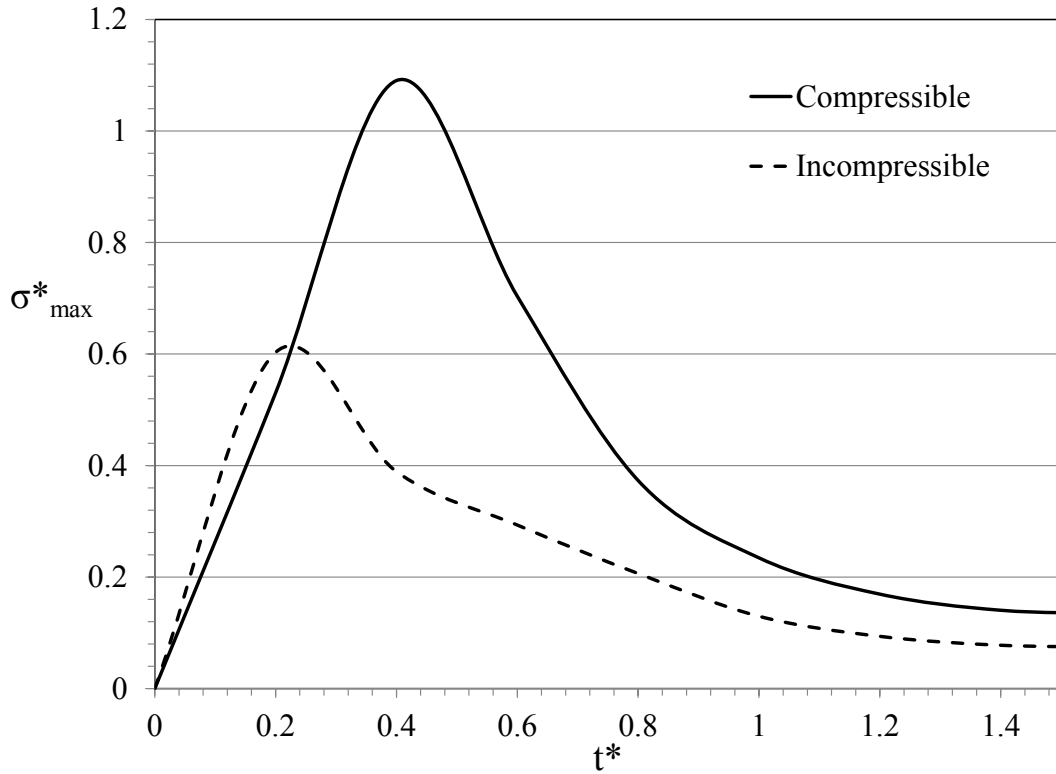


Figure 2-18: Effect of fluid compressibility on maximum stress in the solid,  $D=500 \mu\text{m}$ ,  $V_0=100 \text{ m/s}$ .

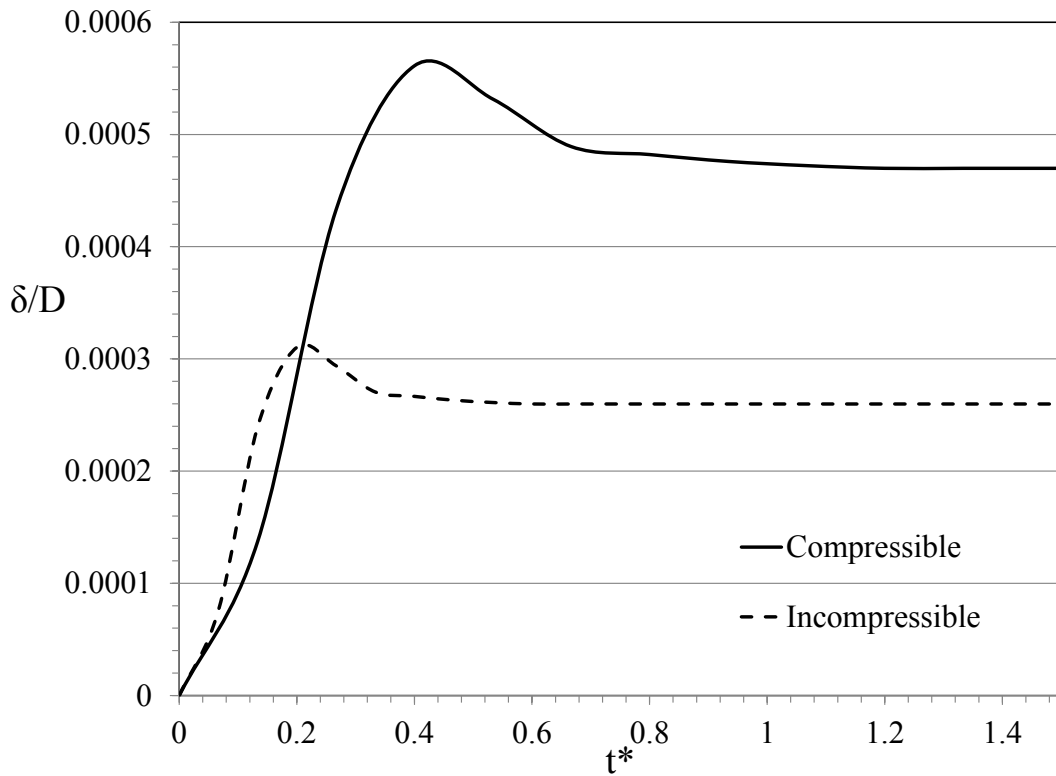


Figure 2-19: Effect of fluid compressibility on substrate deformation,  $D=500 \mu\text{m}$ ,  $V_0=100 \text{ m/s}$ .

# 3. Compressible droplet impact

This chapter outlines the methodology utilized for solving Navier-Stokes equations in addition to the energy equation in their compressible forms. One equation of state per phase, one for gas and one for liquid, is presented. The one-way coupling approach is used to model the droplet at high impingement velocities. In this regard, since the solid deformation is negligible (will be discussed later in section 3.3), the fluid and solid solvers are decoupled, i.e., the compressible fluid results are obtained first and then used as the boundary condition to model the solid stress. FEM modeling is carried out for a LIE case scenario and the transient stresses in the solid in addition to the deformation of the substrate are reported and discussed.

### 3.1 Methodology

As discussed in chapter 2, the fluid compressibility plays an important role at impingement velocities above 100 m/s and can no longer be ignored in pressure calculations. Therefore, a compressible fluid solver is implemented in this chapter to account for the density variation in the fluid. In addition, the energy equation is solved to capture the exact temperature during impact. The relationship between pressure, density and temperature for the two phases is determined by an appropriate equation of state for each phase.

As explained in section 1.4.1, a compressed region is formed inside the droplet which is encapsulated between the high pressure front and solid surface, illustrated in figure 3-1. However, the rest of the droplet, which is unaware of the impact, remains undisturbed. The density and pressure rise in the compressed region is quantified in this chapter. Moreover, the formation of a thin air layer at the impact point in addition to lateral jetting and jet breakup are studied. Finally, FEM modeling results for a Ti-6Al-4V substrate for LIE application is presented.

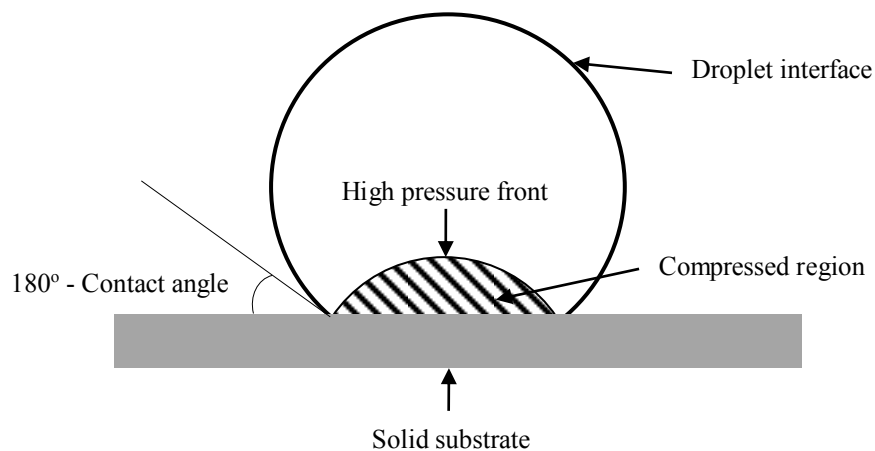


**Figure 3-1: Schematic presentation of a compressible liquid droplet impact on a rigid solid substrate.**

### 3.1.1 Compressible fluid equations

Navier-Stokes equations are solved for two compressible and immiscible fluids using VOF interface capturing approach. The conservation of mass and momentum equations in their transient and compressible forms are as follows,

$$\frac{\partial \rho_f}{\partial t} + \nabla \cdot (\rho_f V_f) = 0 \text{ in } \Omega_f \quad (3-1)$$

$$\frac{\partial (\rho_f V_f)}{\partial t} + \nabla \cdot (\rho_f V_f \otimes V_f) = \nabla \cdot \sigma_f + \rho_f g + \rho_f F_b \text{ in } \Omega_f \quad (3-2)$$

where  $V_f$  is the fluid velocity vector,  $\rho_f$  is the fluid density,  $g$  and  $F_b$  are the gravitational and other body forces (per unit mass) acting on the fluid.  $\sigma_f$  is the Cauchy stress tensor defined as,

$$\sigma_f = -p_f I + \tau_f \quad (3-3)$$

where  $p_f$  is the fluid pressure and  $\tau_f$  is the viscous stress tensor,

$$\tau_f = \mu_f (\nabla V_f + \nabla V_f^T) \quad (3-4)$$

where  $\mu_f$  is the fluid dynamic viscosity.

A single momentum equation is solved for both gas and liquid phases and fluid properties are calculated for the mixture of them. The coupling between the pressure and velocity is achieved by Pressure Implicit with Splitting of Operators (PISO) scheme.

The energy equation for a compressible flow is as follows,

$$\frac{\partial (\rho_f e)}{\partial t} + \nabla \cdot (\rho_f V_f e) + \frac{\partial (\rho_f K)}{\partial t} + \nabla \cdot (\rho_f V_f K) + \nabla \cdot (V_f p) = -\nabla \cdot q + \nabla \cdot (\tau_f \cdot V_f) + \rho_f g \cdot V_f \quad (3-5)$$

where  $e$  is the internal energy and  $K$  is the specific kinetic energy (kinetic energy per unit mass) defined as,

$$K = \frac{|V_f^2|}{2} \quad (3-6)$$

$q$  is the heat flux vector, calculated based on the gradient of the internal energy,

$$q = -\alpha \nabla e \quad (3-7)$$

where  $\alpha$  is the thermal diffusivity.

In addition, in order to close the system of equations, an equation of state for gas and liquid phases is needed. The ideal gas law is applied to account for the air compressibility as follows,

$$p_g = \rho_g R T_g \quad (3-8)$$

where  $R$  is the specific gas constant equal to 287 J/kgK for air.

For the liquid phase, the power law equation of state proposed by Tait [42], commonly used for water, is utilized and defined below,

$$\frac{p_l + B}{p_a + B} = \left( \frac{\rho_l}{\rho_{l_0}} \right)^N \quad (3-9)$$

where  $B$ ,  $p_a$  and  $N$  are three constants from Tait's equation [42] as follows,

$$B = 300MPa, p_a = 0.1MPa, N = 7.415 \quad (3-10)$$

and  $\rho_{l_0}$  is the density of water at ambient conditions equal to 1000 kg/m<sup>3</sup>.

### 3.1.2 Computational domain and material properties

The computational mesh for the 2D axisymmetric domain is the same as the incompressible model displayed in Figure 2-3. In addition, a 3D model for a quarter and half of the domain is utilized depending on the symmetry of the problem under study, illustrated in figure 3-2. In order to reduce the computational time, only the region where the impact occurs is refined and the rest of the domain is coarsely meshed. This technique allows to start with an initial grid size of  $8\ \mu\text{m}$  and reach a finer grid of size  $0.5\ \mu\text{m}$  after four levels of refinement while avoiding the creation of hanging nodes to connect the refined and coarse regions.

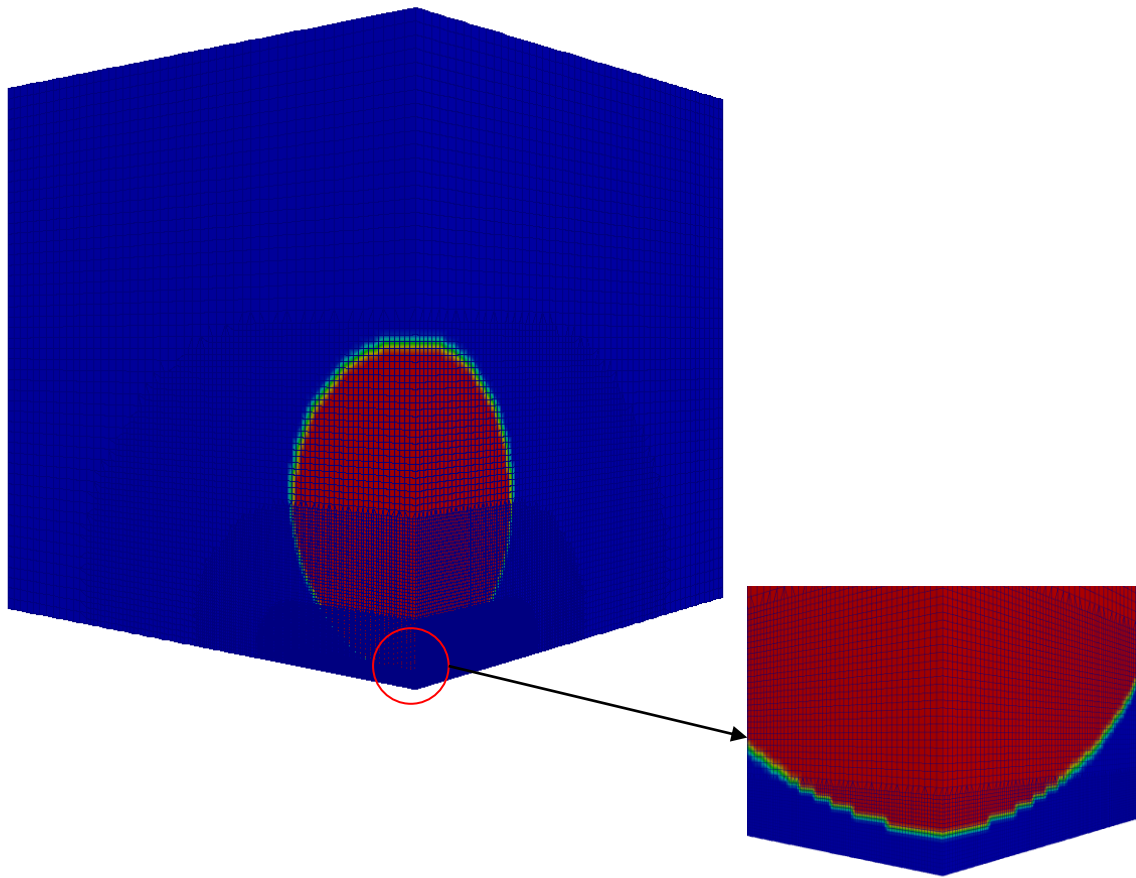


Figure 3-2: Computational domain (quarter) for the 3D model.

For instance, the total number of cells is initially 125,000 and reaches 1.9 million after four refinement levels. The local refinement is achieved by specifying a rectangular box where the finest grid should be applied. In addition, the number of refinement levels and number of buffer layers between different levels are needed as inputs. The OpenFoam mesh refinement dictionary, called `snappyHexMeshDict`, is utilized to locally refine the grid around the impact point. The refinement begins with the cells located in the specified box and moves toward the outer layers. The number of cells between two adjacent layers are set to 30 to ensure uniformity and gradual grid size growth. Finally, a maximum local and global number of cells is specified to limit the cell refinements, set to 100,000 and 20,000,000, respectively.

Since the energy equation is integrated for the compressible solver, thermal properties are required, in addition to hydrodynamic properties, for air and water at ambient conditions, as summarized in table 3-1.

<b>Fluid properties</b>		
Fluid	Air	Water
<b>Density (kg/m<sup>3</sup>)</b>	1.2	1000
<b>Prandtl</b>	0.7296	2.289
<b>Thermal diffusivity (m<sup>2</sup>/s)</b>	1.9e-05	1.43e-07
<b>Kinematic viscosity (m<sup>2</sup>/s)</b>	1.48e-05	1e-06
<b>Surface tension (N/m)</b>	0.073	

**Table 3-1: Fluid properties for air and water at atmospheric condition.**

### **3.1.3 Boundary and initial conditions**

Outflow boundary condition is applied to all fluid boundaries except for the substrate surface. No-slip condition is imposed on the fluid-solid interface. In the 2D axisymmetric model, the droplet center axis has asymmetric boundary condition. In the 3D model, symmetric boundary condition is applied to the plane(s) of symmetry. Initially, the fluid domain is filled with air. At the beginning of each computation the droplet is patched in the fluid domain with the desired size and velocity. The computation for the rest of the cells starts with zero for the velocity and liquid volume fraction. The initial temperature and pressure in all the computational cells including the boundaries are set to the ambient conditions, i.e. 300 K and 100 kPa, respectively.

### **3.1.4 Numerical schemes and discretization**

The numerical schemes and discretization methods used in the incompressible solver are employed again when possible. For other variables, such as temperature, density and kinetic energy, an upwind method, which is first order and bounded, is used to discretize the equations. The second derivative of temperature is discretized with a linear scheme, which is second order and unbounded. The linear Gaussian scheme is utilized for interpolation from the cell centers to the faces.

### **3.2 Results and discussion**

In this section, the results obtained from the present work will be compared against the numerical results for a droplet with a diameter of 200  $\mu\text{m}$  and an impact velocity of 500 m/s, reported by Haller [25], using a 2D axisymmetric model. It should be mentioned that there are two main differences between Haller's model and the present model. First, the flow was assumed to be driven by inertia due to the high Reynolds number ( $10^5$ ), hence, the viscous force was neglected in his model. Second, the stiffened gas equation of state was used for the liquid phase in Haller's study. Whereas, in the present model, the viscous force is taken into account in the momentum equation since it could affect the entrapment of air underneath the droplet. In addition, Tait's equation of state [42], which has a better accuracy for compressible liquids, is utilized in this study.

The contours of pressure (left) and velocity magnitude (right) are presented in figure 3-3 over eight time steps along with the corresponding streamlines (left) and velocity vectors (right) in figure 3-4, in addition to the density (left) and temperature (right) in figure 3-5. Furthermore, the dimensionless values over nine time steps for pressure along r and y axes, radial velocity along r-axis and vertical velocity along y-axis, density and temperature along r and y axes are plotted in figures 3-6 and 3-7, figures 3-8 and 3-9, figures 3-10 and 3-11, figures 3-12 and 3-13, respectively. As it can be seen in figures 3-3 and 3-5, the pressure starts to build up right after the droplet touches down on the solid surface and the density rises. In addition, a distinct region is observed where the pressure is orders of magnitude higher than the rest of the droplet, indicating the compressed region, which is separated from the undisturbed area with the high pressure front mentioned earlier. Moreover, a stagnation region is formed upon the impact as discussed in section 2.2.1.

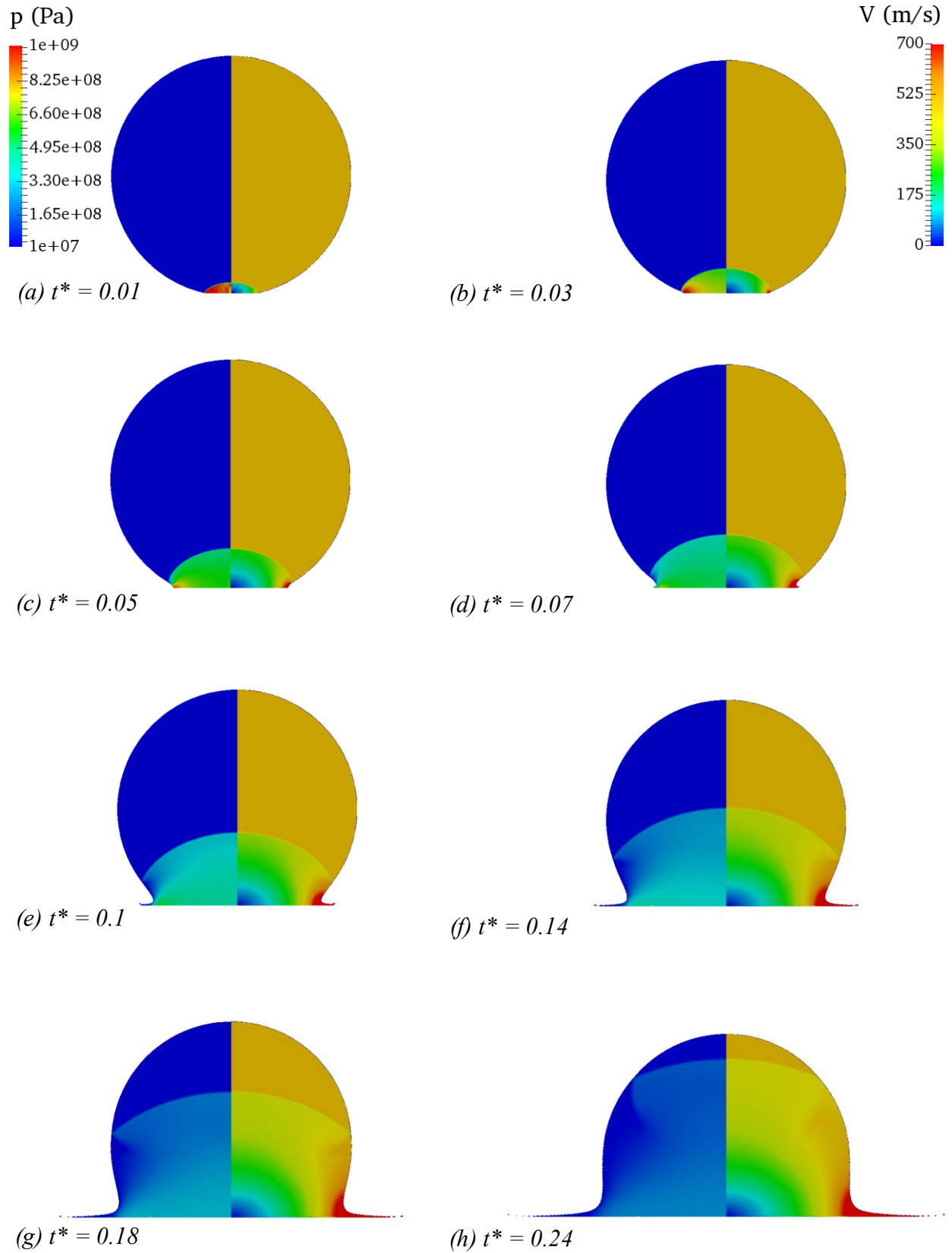
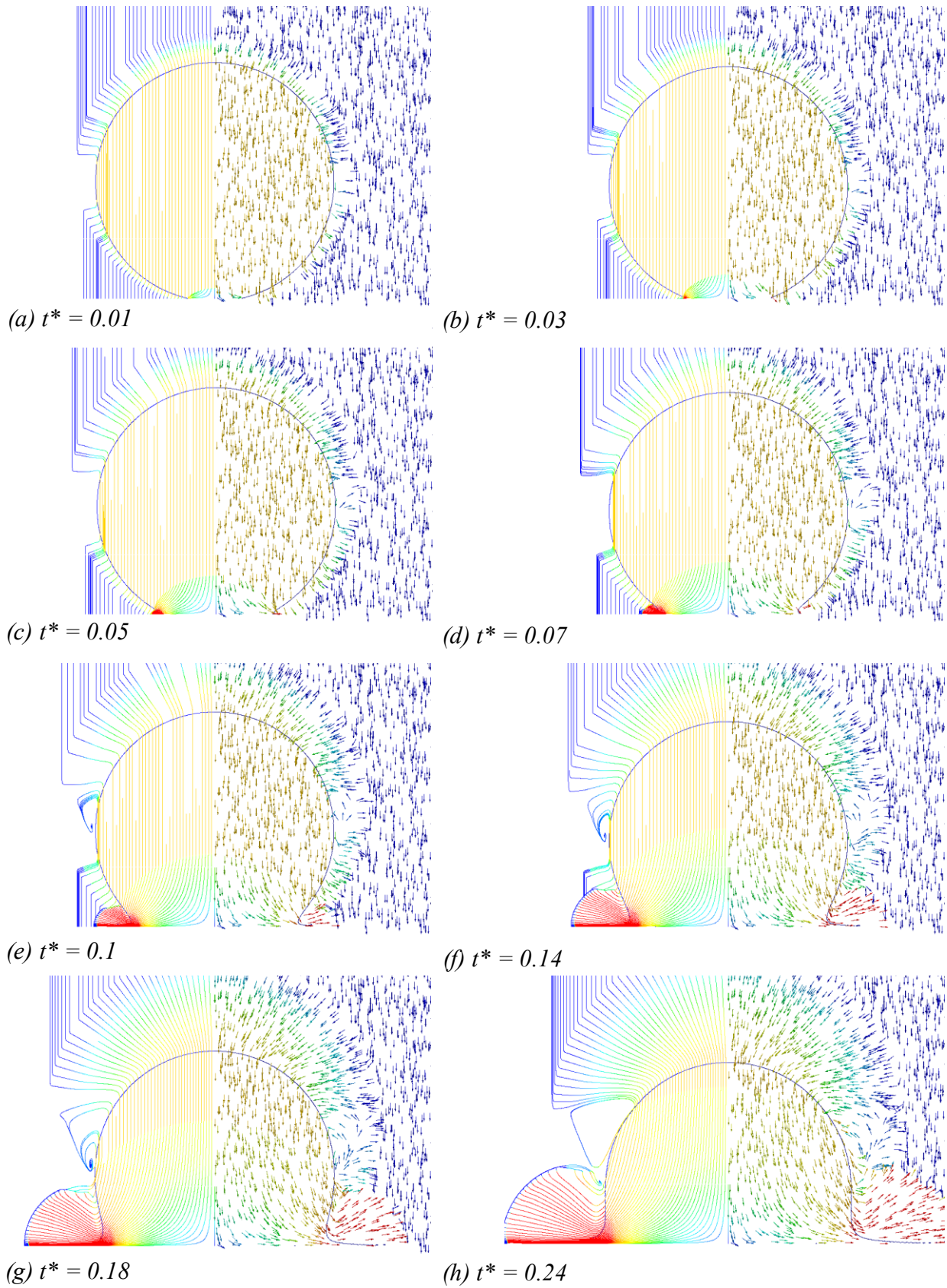


Figure 3-3: Contours of pressure (left) and velocity (right),  $D=200 \mu\text{m}$ ,  $V_0=500 \text{ m/s}$ , rigid substrate.



**Figure 3-4: Streamlines (left) and velocity vectors (right),  $D=200 \mu\text{m}$ ,  $V_0=500 \text{ m/s}$ , rigid substrate.**

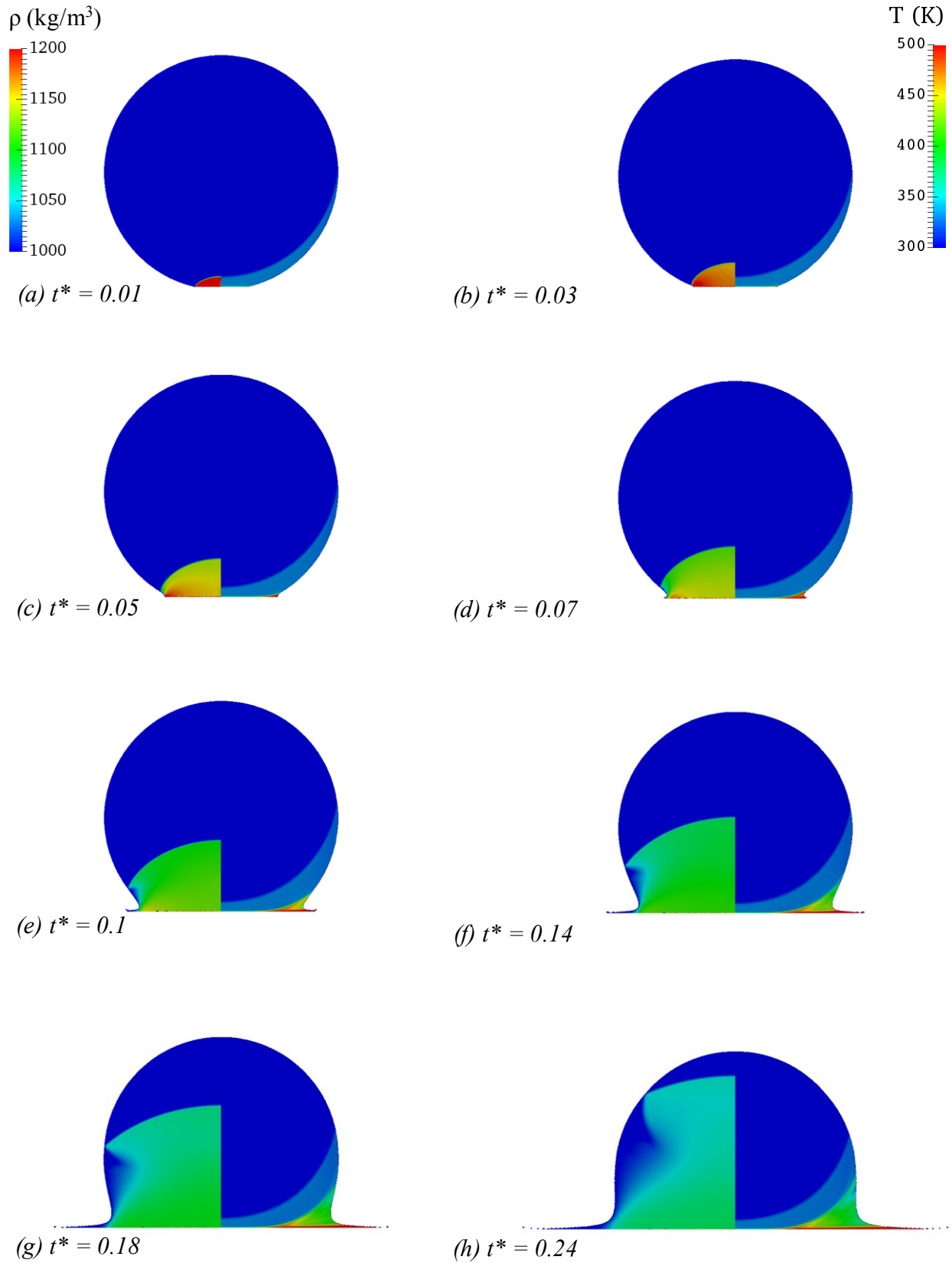


Figure 3-5: Contours of density (left) and temperature (right),  $D=200 \mu\text{m}$ ,  $V_0=500 \text{ m/s}$ , rigid substrate.

At  $t^*=0.005$  after the impact (not shown in the contours above), the pressure reaches the water hammer value ( $p^*=1$ ) at the center ( $r^*=0$ ), displayed in figure 3-6. However, at  $r^*=0.114$  from the center,  $p^*$  reaches a value of 2.2, suggesting that the maximum pressure occurs off the droplet axis with a magnitude more than twice the water hammer pressure. As it can be seen in figure 3-7, the pressure is not maximum on the surface but slightly above it along the y-axis at  $y^*=0.0267$ . This is to be expected, as the liquid region closer to the high pressure front experiences a higher pressure compared to the rest of the compressed region.

The main reason behind this phenomenon is the fact that each fluid particle that comes in contact with the solid surface emits a compression wave that moves in the opposite direction of the impact. Since the liquid density increases after the passage of each compression wave, hence, the speed of sound is higher in this region, the consequent compression wave, emitted due to the impact of another fluid particle on the surface, would travel faster through the disturbed region. As a result, the compression waves that have been generated lately would eventually overtake the previously emitted waves, forming a strong pressure front where the gradients of fluid variable are very sharp. This can be seen in figure 3-9, where the vertical component of the fluid velocity is close to zero in a narrow depth, the compressed region, and jumps to the impact velocity with a steep slope. In fact, the fluid properties for the liquid outside the compressed region remain unchanged, which means that the rest of the droplet is completely unaware of the impact.

Theoretically, the contact line moves with an infinite velocity, however, the fluid particle velocity has a finite value and its radial component ( $V_r^*$ ) is plotted for various time steps in figure 3-8. The droplet edge velocity increases as the droplet spreads over the solid surface up to  $t^*=0.07$  and then start to decelerate due to the viscous dissipation. Around this time step, the air

is expelled from the droplet periphery after the eruption of the lateral jet, which explains the appearance of a double hump in the radial velocity in figure 3-8. During the acceleration period, the high pressure front moves behind the contact line and it remains attached to the interface. After the deceleration of the contact line begins, the high pressure front overtakes the contact line. At this moment, the pressure front detaches from the droplet edge and lateral jetting begins. Figure 3-15 (a) illustrates the density and radial velocity along the r-axis after lateral jetting occurs, at  $t^*=0.07$ . It suggests that the droplet edge reaches a velocity of 2325 m/s ( $V_r^*=4.65$ ), which is considerably higher than the impact velocity (500 m/s). Furthermore, the velocity vectors, displayed in figure 3-4, confirm the development of a strong radial flow in the fluid.

When the high pressure front reaches the droplet edge, it starts to move along the free surface. The reflection of the compression wave from the droplet interface creates an expansion wave normal to the free surface, which can be seen in the light blue area in figure 3-3 (d)-(h) (left). The generated expansion waves rapidly reduce the pressure in the fluid particles located between the free surface and the high pressure front. In other words, they neutralize the influence of the compression waves close to the free surface. As a result, this region undergoes a lower pressure. The low pressure region caused by this rarefaction could lead to cavitation inside the droplet as observed experimentally by Field *et al.* [21]. These rarefaction waves also prevent the lateral jetting from the droplet free surface by rapid pressure reduction. Therefore, lateral jetting only occurs on the droplet edge attached the fluid-solid interface, where the expansion waves are absent due to the presence of the solid surface.

A close look at the density, plotted in figure 3-10, reveals that, at  $t^*=0.03$ ,  $\rho^*=9.61$  at a radial location of  $r^*=0.357$ . Examining the volume fraction graph, figure 3-14, the cells located at  $r^*=0.357$  are mostly filled with the air. Since the pressure at this point reaches a value of

$p^*=2.75$  (1.96 GPa) and the temperature is equal to  $T^*=1.7$  (510K), the ideal gas law would result in a similar value for the air density. It should be mentioned that the pressure reaches its peak,  $p^*=3.93$  (2.8 GPa), at  $t^*=0.01$ , which occurs before the high pressure front overtakes the free surface, around  $t^*=0.03$ , followed by its detachment at  $t^*=0.05$ , presented in figure 3-3 (a)-(c).

The graphs of dimensionless temperature, presented in figures 3-12 and 3-13, demonstrate that the temperature in the compressed region is around  $T^*=1.1$  along the droplet center axis with the maximum of  $T^*=1.25$  on the solid surface ( $y^*=0$ ). More importantly, the temperature is much higher at the droplet periphery with a maximum of  $T^*=2.57$  at  $t^*=0.1$ , which is right after the eruption of lateral jets. As it can be seen from the temperature contours, displayed in figure 3-5 (right), the droplet edge has the highest temperature compared to the rest of the liquid bulk since it has the highest kinetic energy (due to its velocity). The viscous dissipation in the fluid that is in contact with the solid surface, partially converts this kinetic energy to thermal energy, hence, the heat transfer in this region is enhanced. As a result, the lateral jet that is erupted from the droplet periphery reaches a temperature as high as 771 K ( $T^*=2.57$ ). This is well above the boiling temperature of water (373 K), provided that the pressure at this radial location, i.e.  $r^*=0.9$ , is atmospheric. Therefore, the water that is attached to the solid surface close to the droplet edge would evaporate when jet eruption occurs. This would lead to strong cavitation and a vapor rim would be created underneath the impinging droplet. It should be noted that the equations for the phase change are not integrated in the current model, hence, such a cavitation due to the water evaporation cannot be captured here. As a continuation of the present work, the phase change model can be added to the solver to study the cavitation in details.

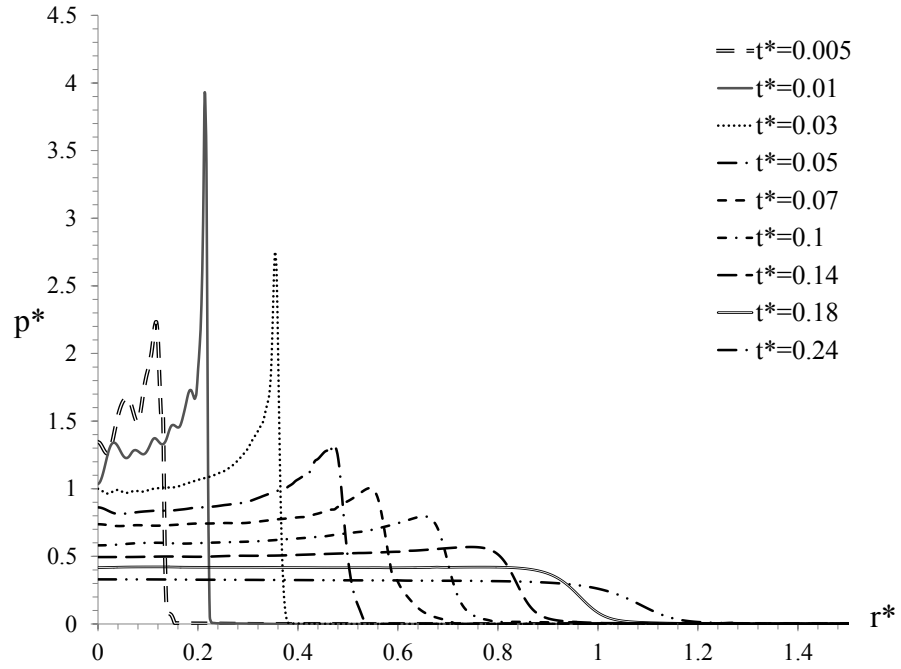


Figure 3-6: Dimensionless pressure along r-axis,  $D=200 \mu\text{m}$ ,  $V_0=500 \text{ m/s}$ , rigid substrate.

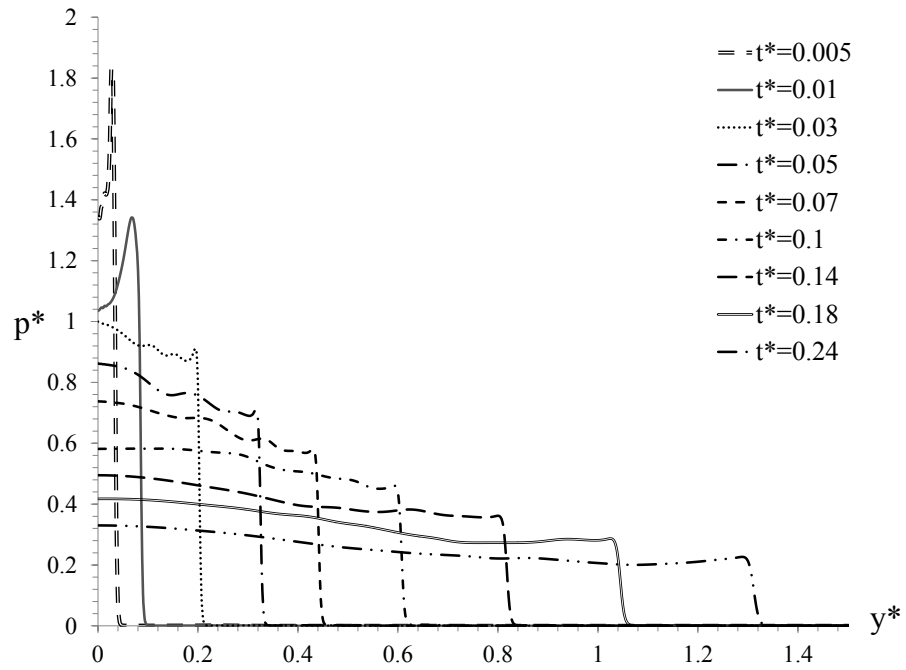


Figure 3-7: Dimensionless pressure along y-axis,  $D=200 \mu\text{m}$ ,  $V_0=500 \text{ m/s}$ , rigid substrate.

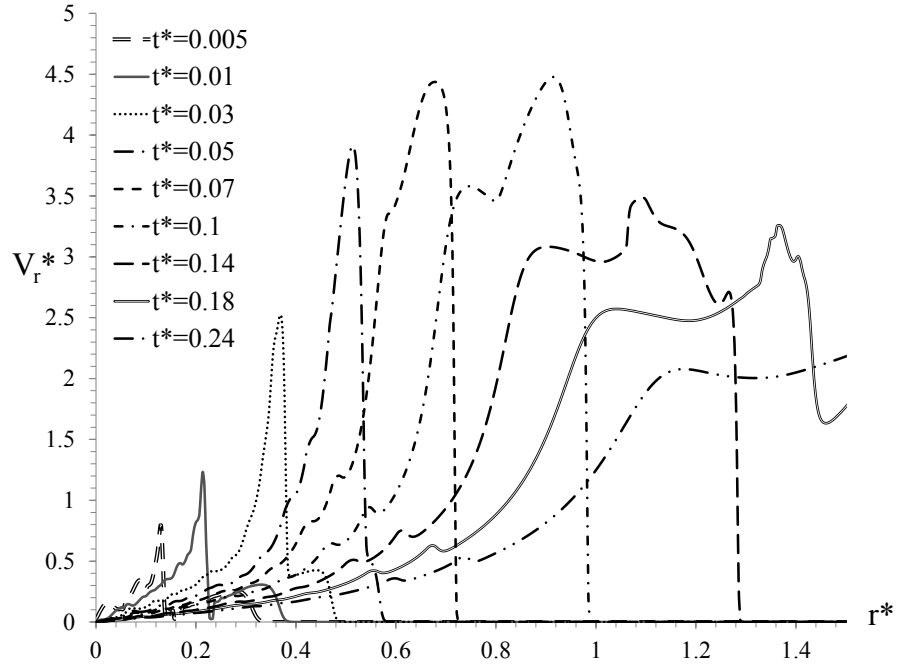


Figure 3-8: Dimensionless radial velocity along  $r$ -axis,  $D=200 \mu\text{m}$ ,  $V_0=500 \text{ m/s}$ , rigid substrate.

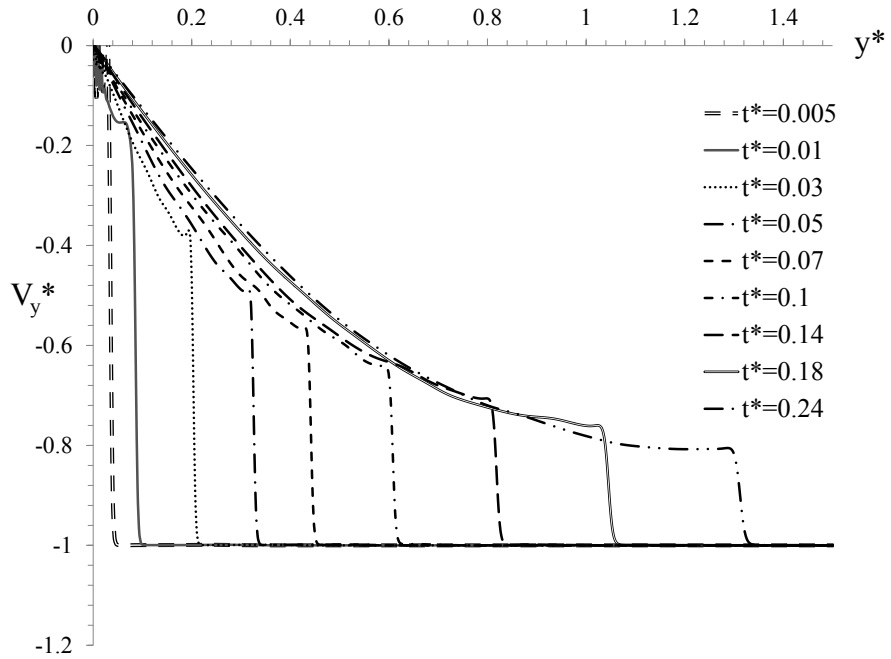


Figure 3-9: Dimensionless vertical velocity along  $y$ -axis,  $D=200 \mu\text{m}$ ,  $V_0=500 \text{ m/s}$ , rigid substrate.

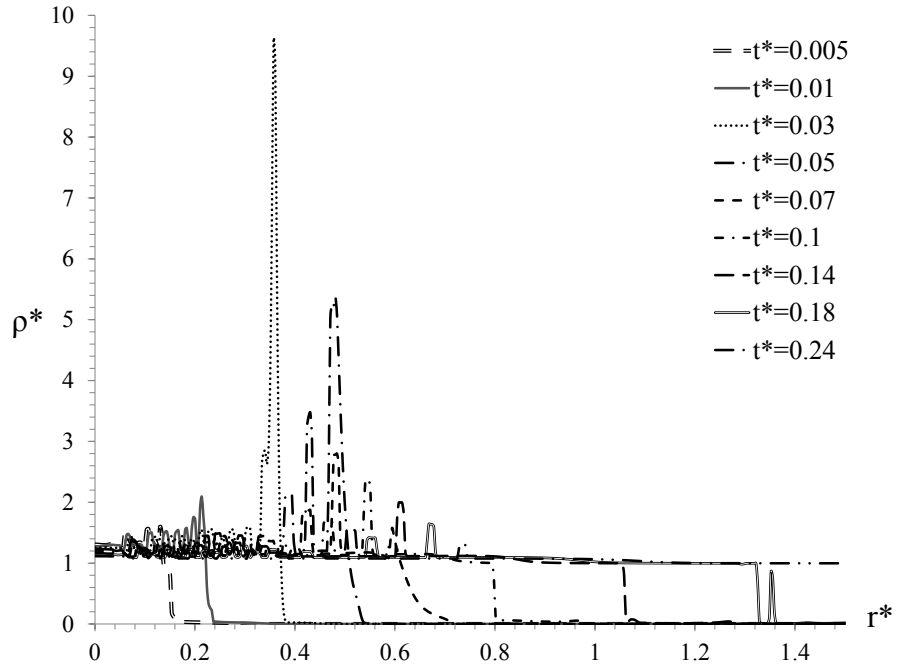


Figure 3-10: Dimensionless density along  $r$ -axis,  $D=200 \mu\text{m}$ ,  $V_0=500 \text{ m/s}$ , rigid substrate.

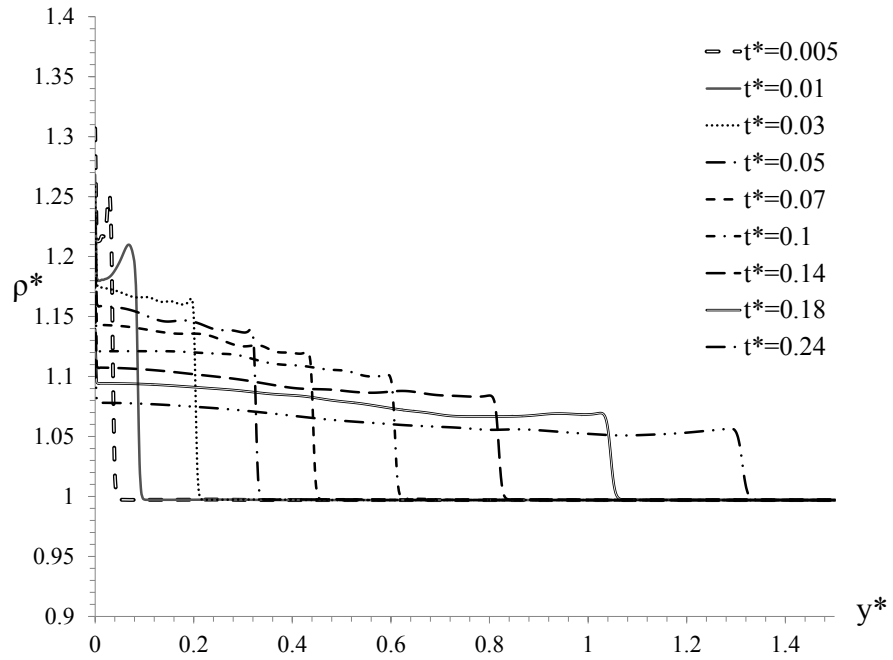


Figure 3-11: Dimensionless density along  $y$ -axis,  $D=200 \mu\text{m}$ ,  $V_0=500 \text{ m/s}$ , rigid substrate.

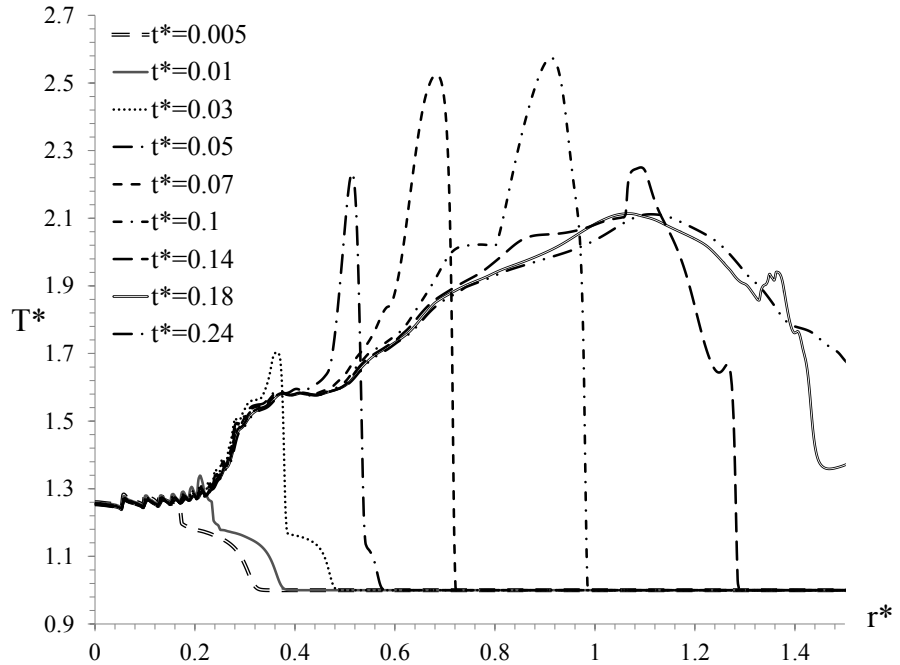


Figure 3-12: Dimensionless temperature along  $r$ -axis,  $D=200 \mu\text{m}$ ,  $V_0=500 \text{ m/s}$ , rigid substrate.

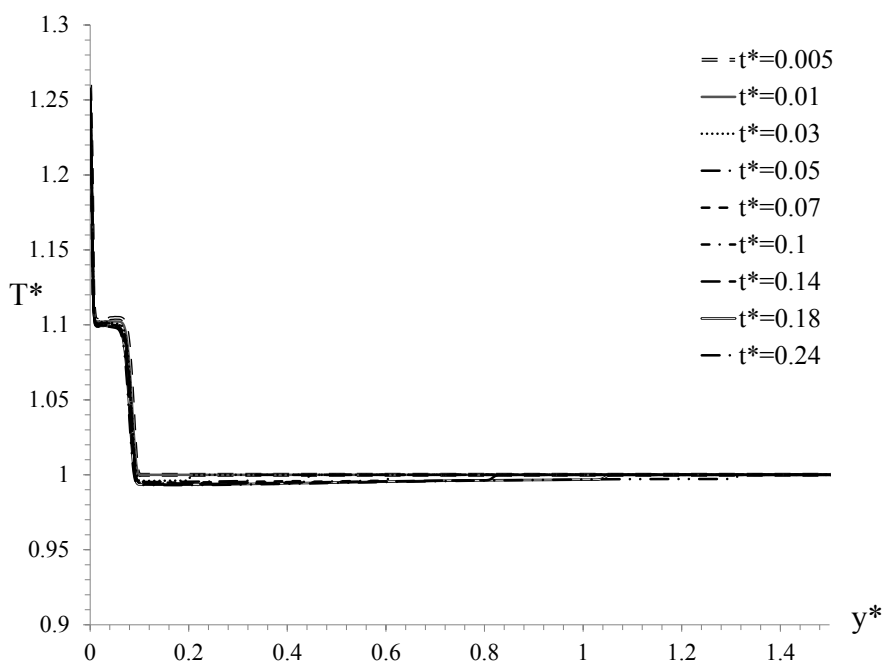
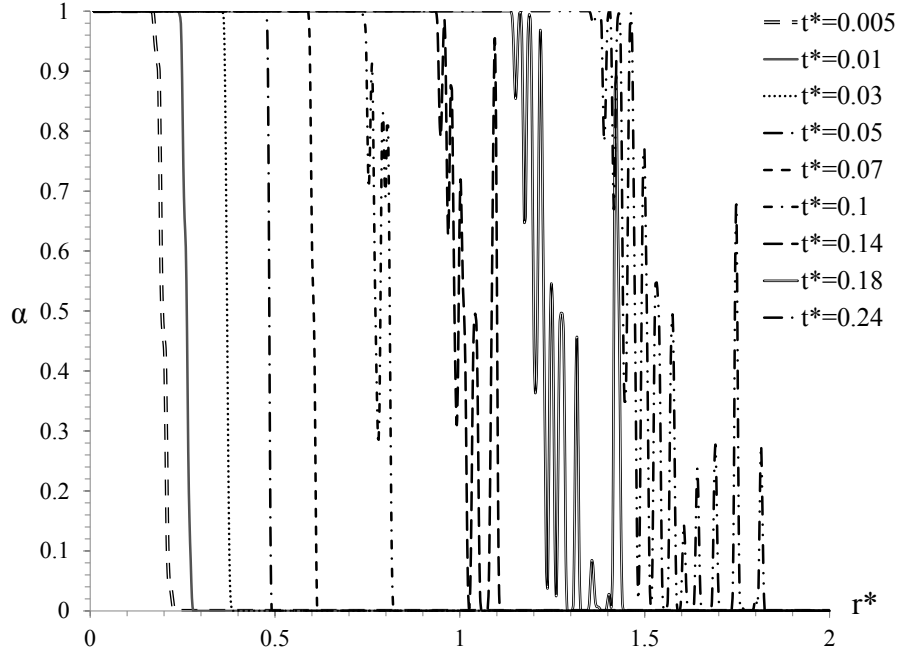


Figure 3-13: Dimensionless temperature along  $y$ -axis,  $D=200 \mu\text{m}$ ,  $V_0=500 \text{ m/s}$ , rigid substrate.



**Figure 3-14: Liquid volume fraction along r-axis,  $D=200 \mu\text{m}$ ,  $V_0=500 \text{ m/s}$ , rigid substrate.**

The density and radial velocity obtained from the present work are presented on top of the values of density and lateral particle velocity reported by Haller [25], in figure 3-15 (a) and (b), respectively. As it was mentioned earlier, there are two fundamental differences between Haller's formulation and the present model. Therefore, the time of the lateral jetting and the location where it occurs are different in the two studies. However, the maximum radial velocity in the fluid obtained from the current model is equal to 2325 m/s, which is in good agreement with Haller's simulation. Furthermore, the maximum pressure observed in the compressed region inside the droplet is equal to  $p^*=3.93$  (2.8 GPa), which is 16% higher than the peak pressure reported by Haller, i.e. close to 2.4 GPa, for the same impact condition. This is to be expected since in his model, Haller utilized the stiffened gas equation of state for water which results in a linear equation, whereas, in Tait's equation of state (eq. (3-10)), the pressure-density relation is a power-law with a component of 7.415.

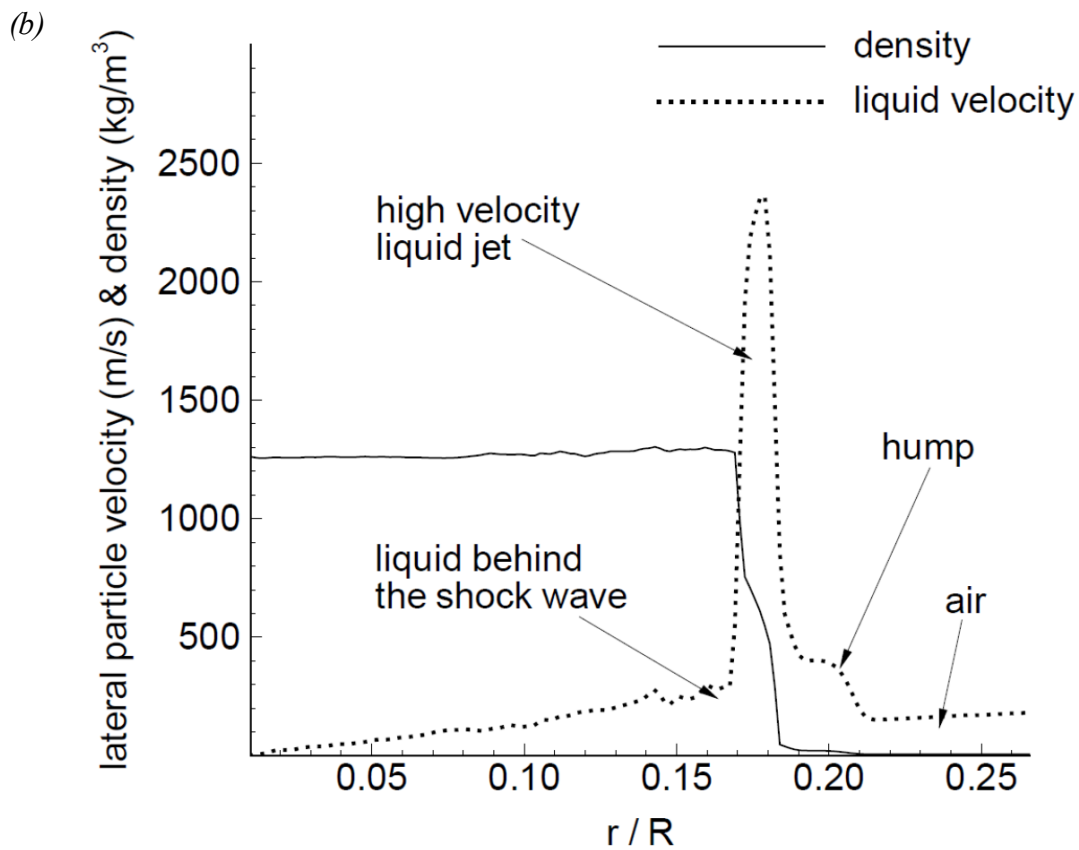
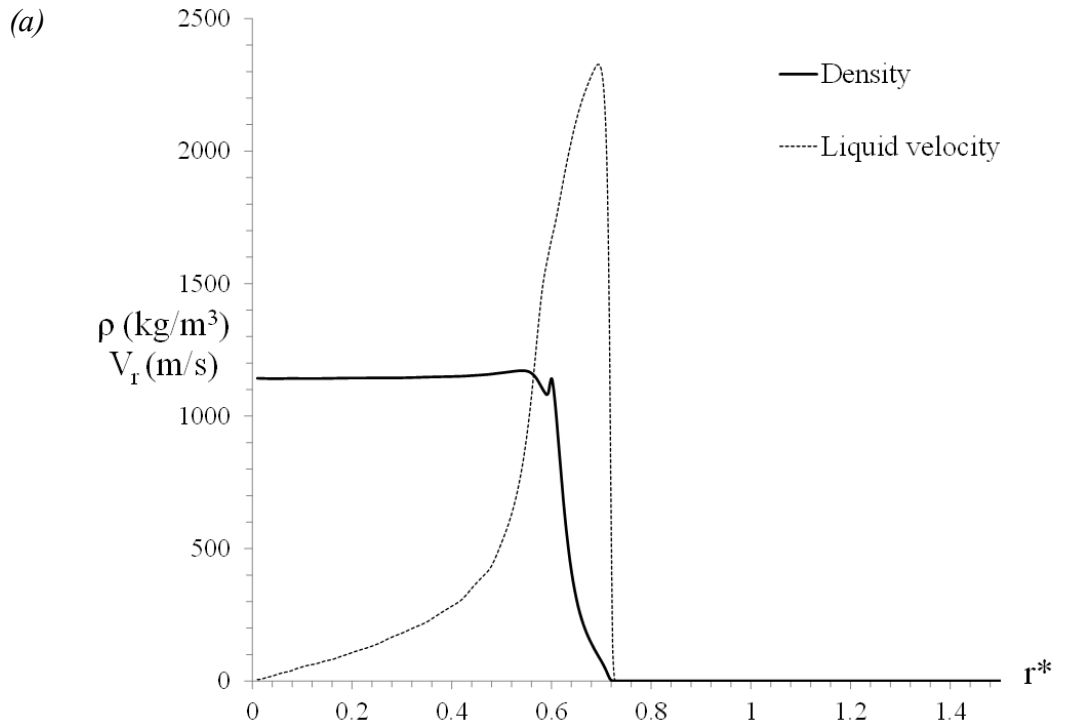


Figure 3-15: Density and radial liquid velocity along  $r$ -axis, (a) present work at  $t^*=0.07$ ,

(b) extracted from Haller [25] at 3.05 ns after impact,  $D=200 \mu\text{m}$ ,  $V_0=500 \text{ m/s}$ .

### 3.2.1 Single droplet impingement at a normal angle

The compressible solver outlined in this chapter, is employed to parametrically study the droplet impingement at various velocities and diameters. In the first case, a typical impact scenario that occurs in LIE problem is considered with a droplet diameter of 500  $\mu\text{m}$  impinged onto a rigid substrate and the velocity is increased from 100 to 500 m/s, in increments of 50 m/s. The maximum dimensionless pressure, exerted on the solid surface, is plotted versus the impact Mach number (Ma), presented in figure 3-16, in comparison with the analytical correlation, equation (3-11), developed by Heymann [19]. The Mach number ( $\text{Ma} = V_0/C$ ) is defined as the ratio of the impingement velocity to the speed of sound in water, i.e. 1430 m/s.

$$p_{\max}^* = 2 + 3 Ma \quad [19] \quad (3-11)$$

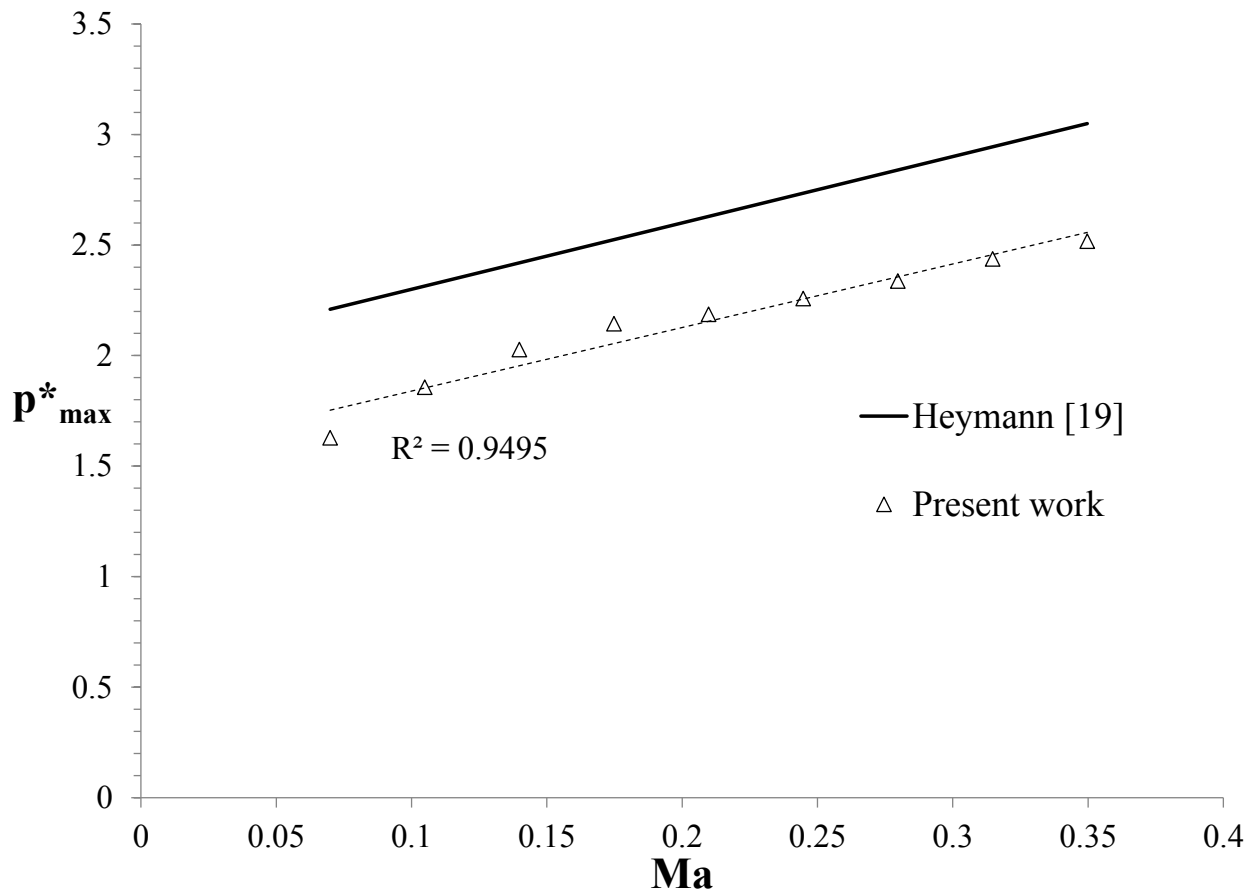


Figure 3-16: Maximum dimensionless pressure versus Ma, comparison with Heymann [19].

The results illustrated in figure 3-16, reveal that the maximum pressure almost increases linearly with the Mach number. A linear equation, obtained from the curve fit applied to the dimensionless pressures modeled in the present work, is as follows,

$$p_{\max}^* = 1.5515 + 2.875 Ma, \text{ for } D = 500 \mu\text{m and } 100 \text{ m/s} \leq V_0 \leq 500 \text{ m/s} \quad (3-12)$$

It should be mentioned that the speed of sound for undisturbed water (1430 m/s) is used to calculate the Mach number for all the impact velocities. In general, the numerical values are lower than the analytical values predicted by Heymann's equation [19]. As it can be seen in the graph, Heymann's correlation overestimates the maximum pressure generated due to the impact. This is to be expected since the appearance of the expansions waves, due to the reflection of the compression waves from the free surface, were not considered in Heymann's model. As it was discussed in the previous section, these expansion waves rapidly reduce the pressure in the liquid region located between the free surface, high pressure front and the solid surface. As a result, the maximum pressure imposed on the substrate would be lower.

Furthermore, Heymann assumed a 2D inviscid flow in his formulation, which results in a cylindrical shape instead of a spherical droplet. As the momentum transfer at the impact point is a function of the geometry of the impinged particle, this simplification leads to an overestimation of the inertia exerted on the surface, hence, the predicted pressure would be higher. In addition, in his analytical model, the viscous and surface tension effects were not considered. Neglecting the viscous dissipation and the surface tension energy in the fluid equations could also contribute to an overestimation of the inertia and generated pressure.

In order to investigate the dependency of maximum generated pressure on the droplet size, the impact velocity is fixed at 350 m/s and the droplet diameter is varied from 300 to 1000  $\mu\text{m}$  in increments of 100  $\mu\text{m}$ . Figure 3-17 presents the variation of the maximum generated pressure versus the droplet size. The analytical correlation proposed by Heymann [19] is used again for comparison. It should be mentioned that Heymann's correlation [19] is only a function of the impact Mach number (or impact velocity) and independent of the droplet diameter. Hence, it results in the same value for all the drop diameters. The numerical simulations reveal that for larger droplets, e.g. 1000  $\mu\text{m}$ , the predicted pressure is close to the analytical value from Heymann's correlation with less than 7% deviation.

However, for smaller droplets, no particular pattern can be observed in the maximum pressure. For instance, a droplet with a diameter of 300  $\mu\text{m}$  generates 4.5% more pressure compared to a 400- $\mu\text{m}$  droplet with the same impingement velocity of 350 m/s. This could be related to the fact that the high pressure envelope is interconnected with the droplet size and the size of the air layer, compressed underneath the impinging droplet, is also a function of the droplet diameter. In addition, the detachment of the high pressure front, which depends on the distance from the impact point to the droplet edge, plays an important role in determining the peak pressure on the surface.

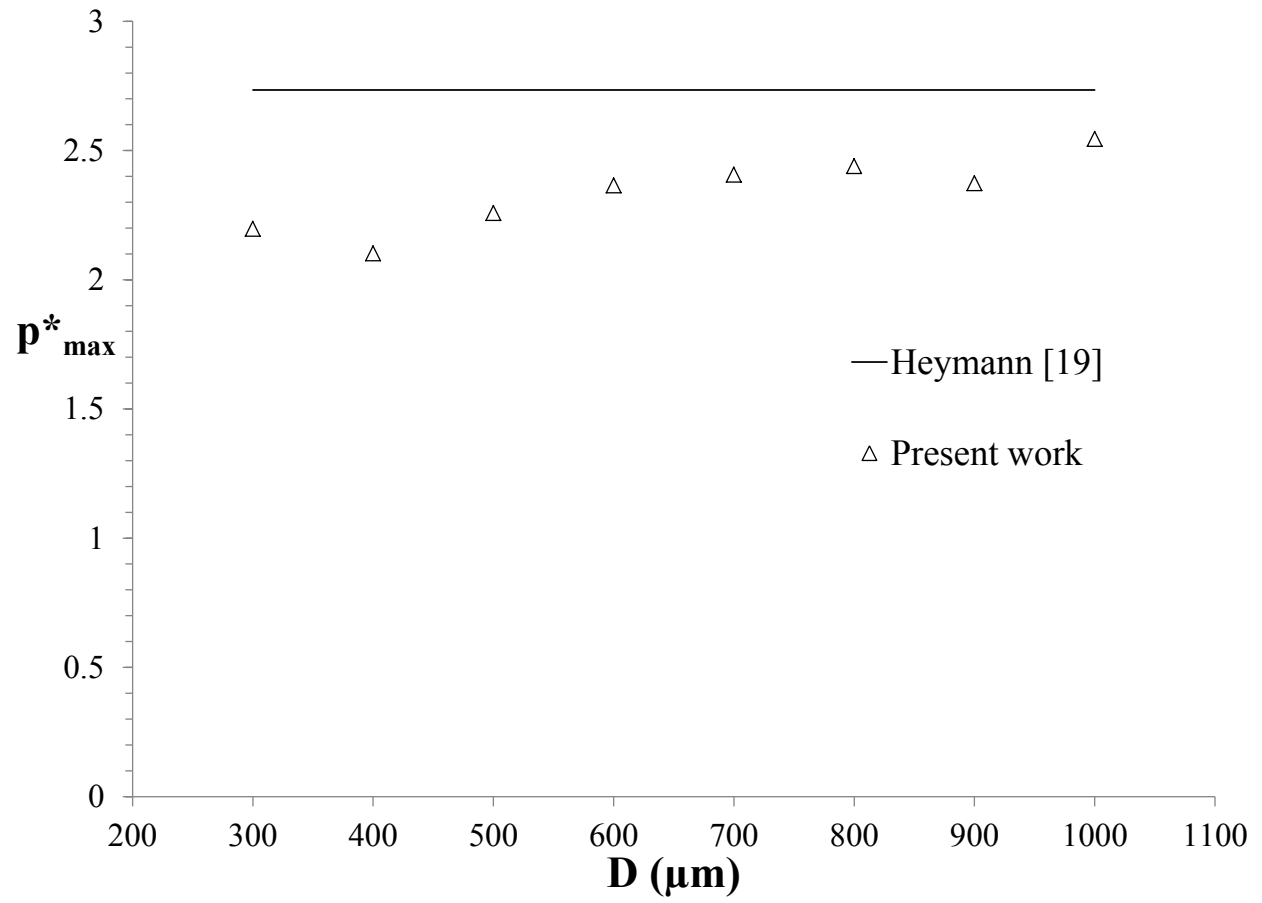


Figure 3-17: Maximum dimensionless pressure versus droplet diameter, comparison with Heymann [19].

### 3.2.2 Single droplet impingement at oblique angles

The effect of the impingement angle on the maximum pressure generated by the impact of a 500- $\mu\text{m}$  droplet at 350 m/s velocity is investigated and presented in figure 3-18. The impact angle varies between 30 to 90 degrees, 90 degrees representing a perpendicular impingement. Figure 3-18 illustrates that the peak pressure upon impact is higher as the impact angle is increased. If one considers the normal component of the impact velocity ( $V_n = V_0 \cdot \sin \theta$ ), the effective momentum transfer during impact will be a strong function of normal velocity,  $V_n$ . As the impact angle increases from 30 to 90 degrees, so does the normal velocity of the impact, hence, this increase results in higher pressures generated upon the impact.

Nevertheless, the pressure values obtained from the 3D numerical simulations indicate that the impact pressure is actually lower than the values predicted by the linear equations (3-11) and (3-12), proposed by Heymann [19] and obtained from the present work, respectively. It should be mentioned that the impact velocity  $V_0$  is replaced by its normal projection ( $V_n$ ) in calculating the Mach number ( $Ma$ ) in equations (3-11) and (3-12) to obtain the maximum  $p^*$ . This is an approximation and does not take into account the momentum transfer on the surface along the tangential direction. To that end, the 3D model simulates the actual impact scenario without any simplifications. Thus, utilization of Heymann's linear equation, by replacing the impact velocity with  $V_n$ , would lead to overestimating the maximum impact pressure by up to 25%, for the impingement angle of 30 degrees.

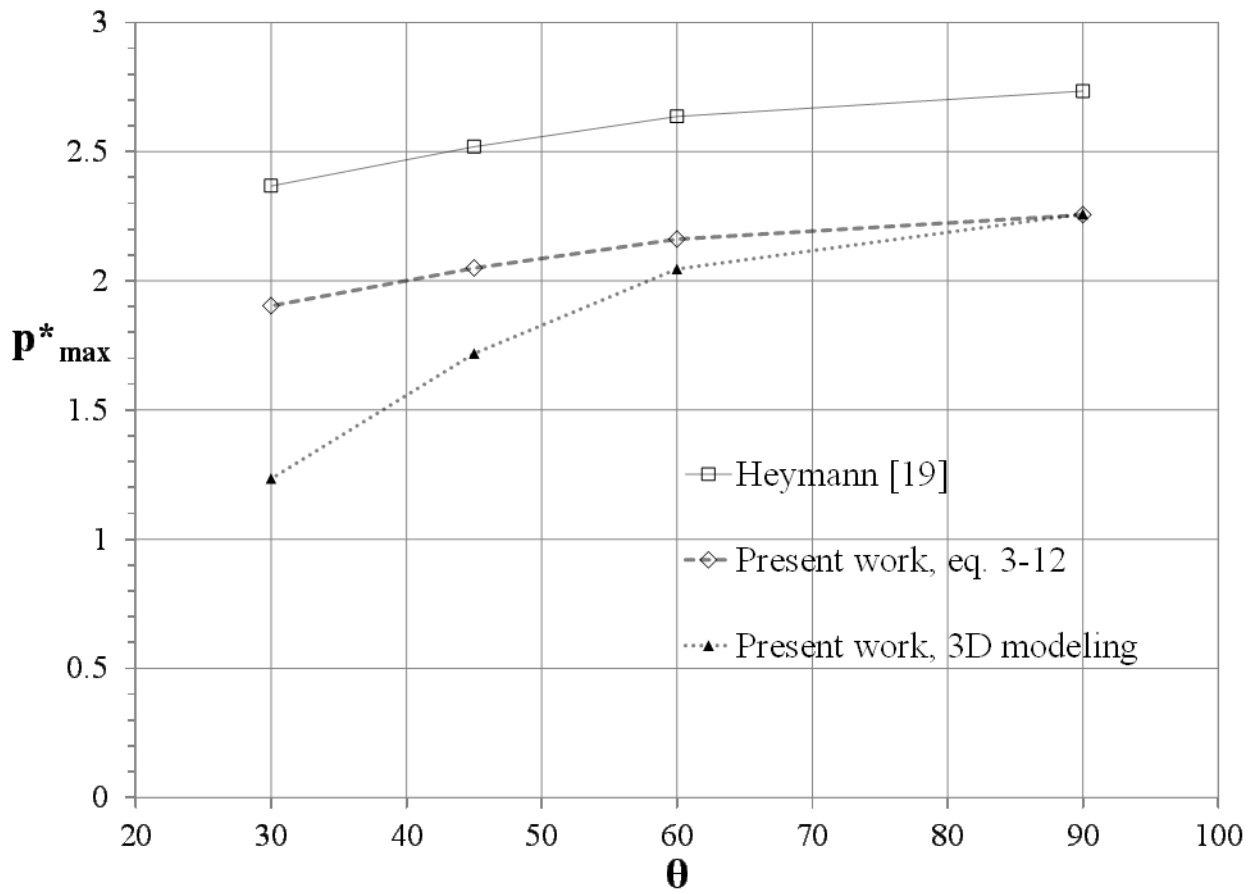
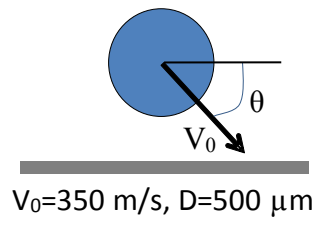


Figure 3-18: Maximum dimensionless pressure versus impingement angle, comparison with Heymann [19].

### 3.2.3 Droplet impact onto liquid films

Finally, a scenario is considered where the previously impinged droplet has spread over the surface and the consequent droplet impact occurs on a thin liquid film. In this regard, the impact of a droplet with a diameter of 500  $\mu\text{m}$  and impingement velocity of 350 m/s onto a liquid film with a thickness of 100  $\mu\text{m}$  ( $h/D=0.2$ ) is considered. The contours of pressure (left) and velocity (right) are presented in figure 3-19 over 8 time steps. In addition, the contours of density (left) and temperature (right) are displayed in figure 3-20.

As it can be seen in figure 3-19 (a), a high pressure region is formed at  $t^*=0.0245$  within the droplet and almost mirrored in the liquid film, however, its envelope is larger inside the film. Figure 3-20 (a) reveals that the density rises in the compressed region and the highest density appears in a narrow region (in red) between the droplet edge and liquid film. The temperature in this area also increases. At  $t^*=0.0385$ , the high pressure front penetrates further down the liquid film, shown in figure 3-19 (b), and the highest velocity and pressure are observed around the droplet edge. The pressure front reaches the solid surface by  $t^*=0.0525$  and a secondary compressed region is formed in the liquid, illustrated in figures 3-19 and 3-20 (c). However, the maximum density is still located at the droplet-film interface.

The compressed region inside the liquid film keeps growing until  $t^*=0.0805$ , when it reaches the initial liquid film surface. At the same moment, the lateral jetting commencement can be observed in figures 3-19 and 3-20 (e). The temperature also rises in the jet and the liquid attached to it. At  $t^*=0.0945$ , the compression waves that impacted the liquid free surface are projected back in the opposite direction inside the liquid as expansion waves. The interaction between the compression and expansion waves results in stripes of high and low pressures that can be clearly seen in figure 3-19 (f)-(h). The contours of volume fraction, presented in figure 3-

21, demonstrate that the high density dots, observed in figure 3-20, are in fact air bubbles that have been trapped between the droplet interface and liquid film upon the impact. Figure 3-22 (b) clearly shows that the eruption of the lateral jet from the edges has already begun. Figures 3-19 and 3-20 (f)-(h) demonstrate that the lateral jet erupted from the droplet periphery in contact with the liquid film is associated with a high velocity and temperature because of the momentum and heat transfer in that region, as discussed in section 3.2.1.

It is worth mentioning that the formation of the lateral jet is delayed upon the impact on a liquid film as opposed to a rigid substrate. This is due to the fact that the liquid film is easily deformed by the impinging droplet and the kinetic energy is transferred from the droplet to the liquid film. As a result, the stagnation region is not developed until the pressure front reaches the solid surface, at  $t^*=0.0385$ . After this time, the radial flow is enhanced as the stagnation region grows in the liquid film and the eruption of the lateral jet can be observed at  $t^*=0.0805$ , shown in figure 3-19 (e).

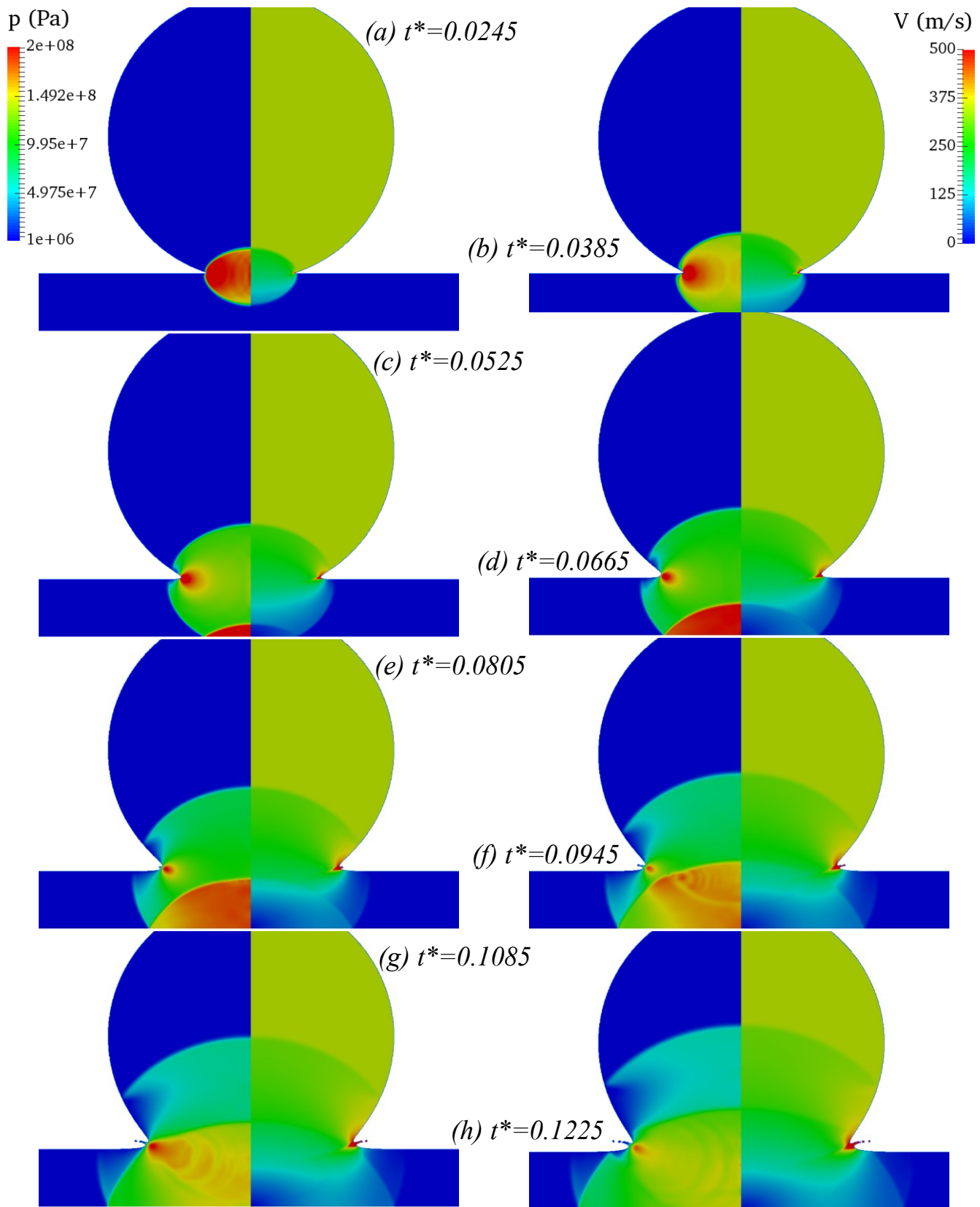


Figure 3-19: Contours of pressure (left) and velocity (right),  $D=500 \mu\text{m}$ ,  $V_0=350 \text{ m/s}$ ,  $h/D=0.2$ .

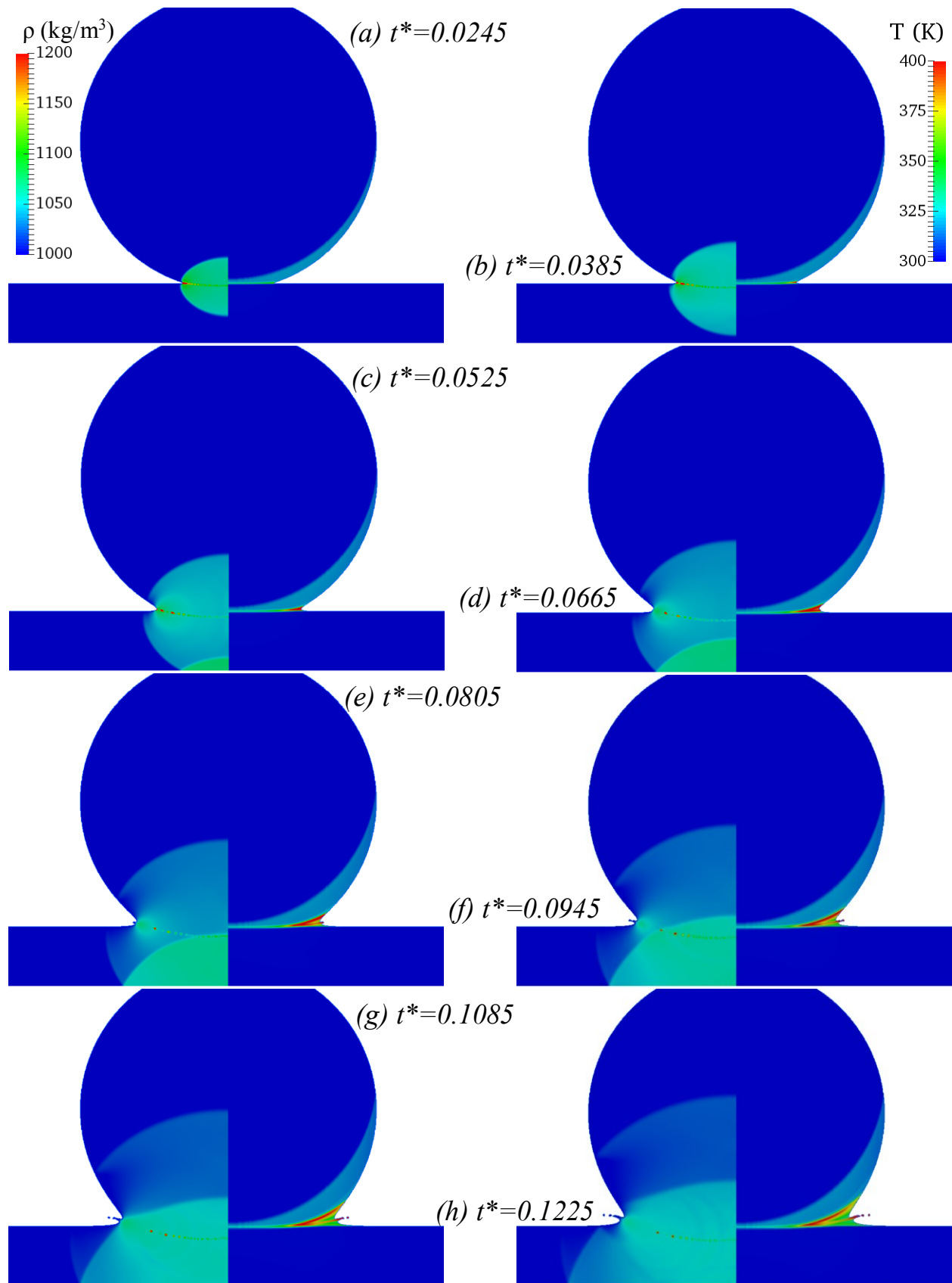
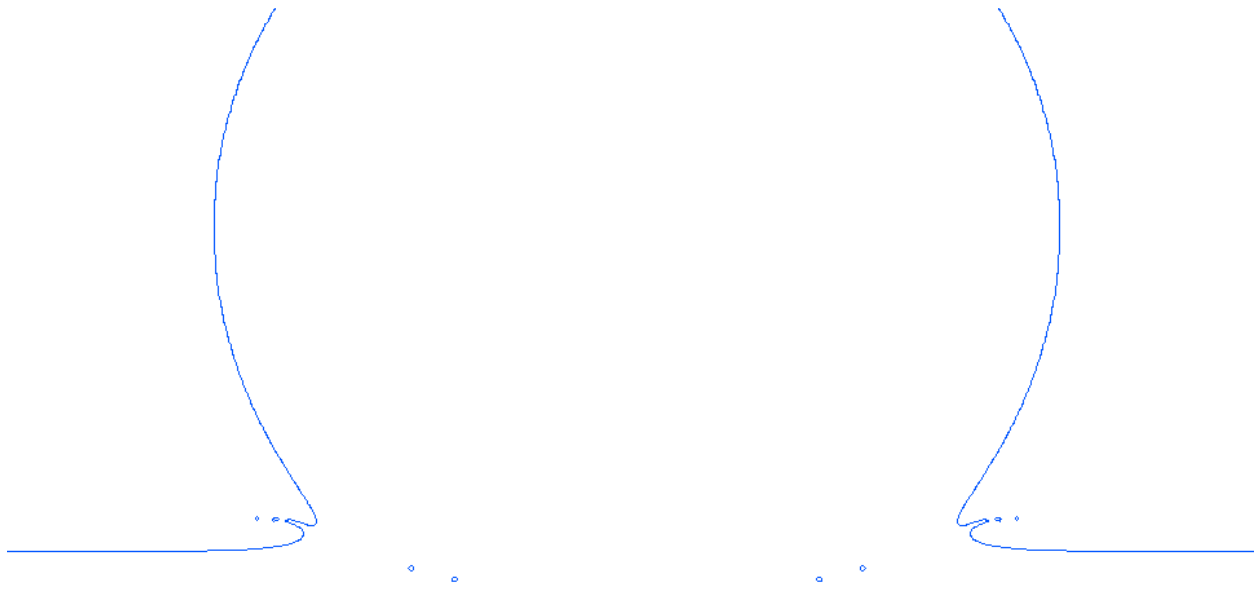
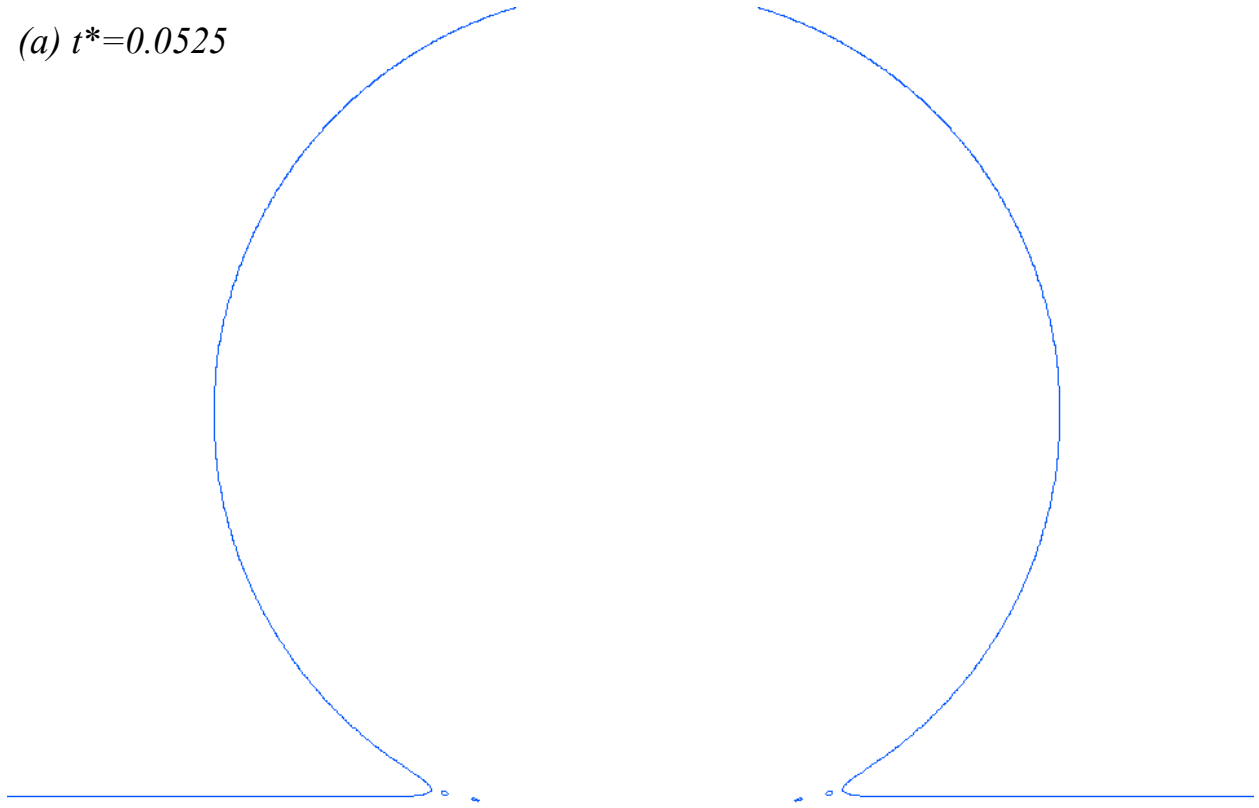


Figure 3-20: Contours of density (left) and temperature (right),  $D=500 \mu\text{m}$ ,  $V_0=350 \text{ m/s}$ ,  $h/D=0.2$ .

(a)  $t^*=0.0525$



(b)  $t^*=0.1225$

Figure 3-21: Contours of liquid volume fraction,  $D=500 \mu\text{m}$ ,  $V_0=350 \text{ m/s}$ ,  $h/D=0.2$ .

As a parametric study, 11 film thickness ratios from 0.02 up to 0.4, corresponding to a thickness of 10  $\mu\text{m}$  to 200  $\mu\text{m}$ , with the same droplet size of 500  $\mu\text{m}$  and impingement velocity of 350 m/s are modeled. Figure 3-22 presents the data points for maximum dimensionless pressure plotted versus the film thickness to initial droplet diameter ratio ( $h/D$ ) in addition to a logarithmic curve fit with the following natural logarithm function,

$$p_{\max}^* = -0.268 \ln(h/D) + 0.0587, \quad \text{for } 0 \leq h/D \leq 0.4 \quad (3-13)$$

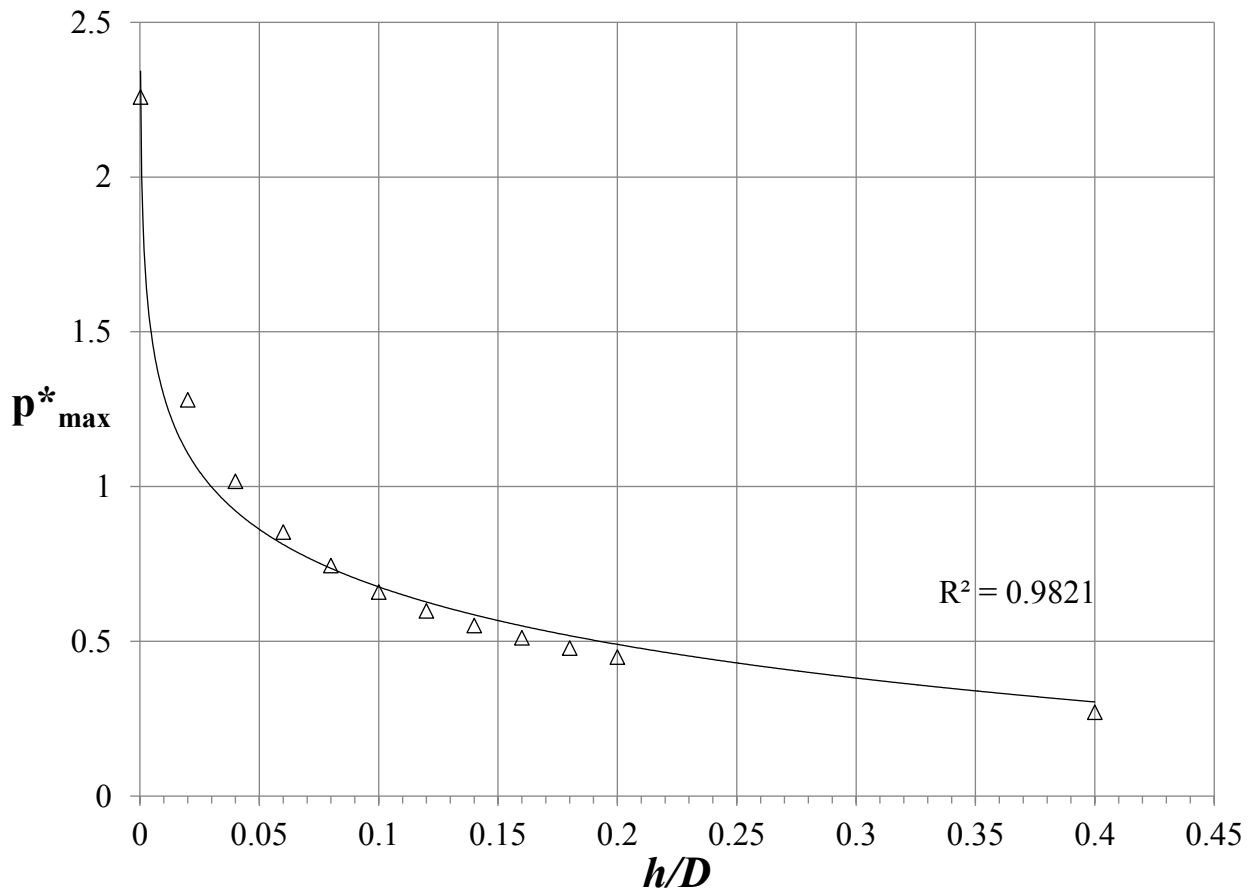


**Figure 3-22: Maximum dimensionless pressure versus film thickness to droplet diameter ratio.**

As it can be seen in figure 3-22, and indicated by equation (3-13), the maximum pressure imposed on the surface diminishes exponentially with respect to the film thickness. For instance, the maximum pressure is equal to the water hammer pressure ( $p^*=1$ ) for  $h/D=0.04$  (20  $\mu\text{m}$ ) and

half of the water hammer pressure ( $p^*=0.5$ ) for  $h/D=0.16$  ( $80\ \mu\text{m}$ ). In other words, the liquid film partially absorbs the impact force and reduces the pressure build-up on the substrate, thus the subsequent stress under the solid surface would decrease substantially.

Figure 3-23 presents the pressure results for various impingement velocities (100-500 m/s) with a droplet size of  $500\ \mu\text{m}$  and film thickness to diameter ratio of  $h/D=0.2$  along with a polynomial curve fit as follows,

$$p_{\max}^* = 7.1425 Ma^2 + 0.0601 Ma + 0.0095, \text{ for } h/D = 0.2 \text{ and } 0.07 \leq Ma \leq 0.35 \quad (3-14)$$

Figure 3-23 and equation (3-14) demonstrate that the maximum pressure exerted on the solid surface upon the impact of a liquid droplet onto a liquid film is a quadratic function of the impingement Mach number.

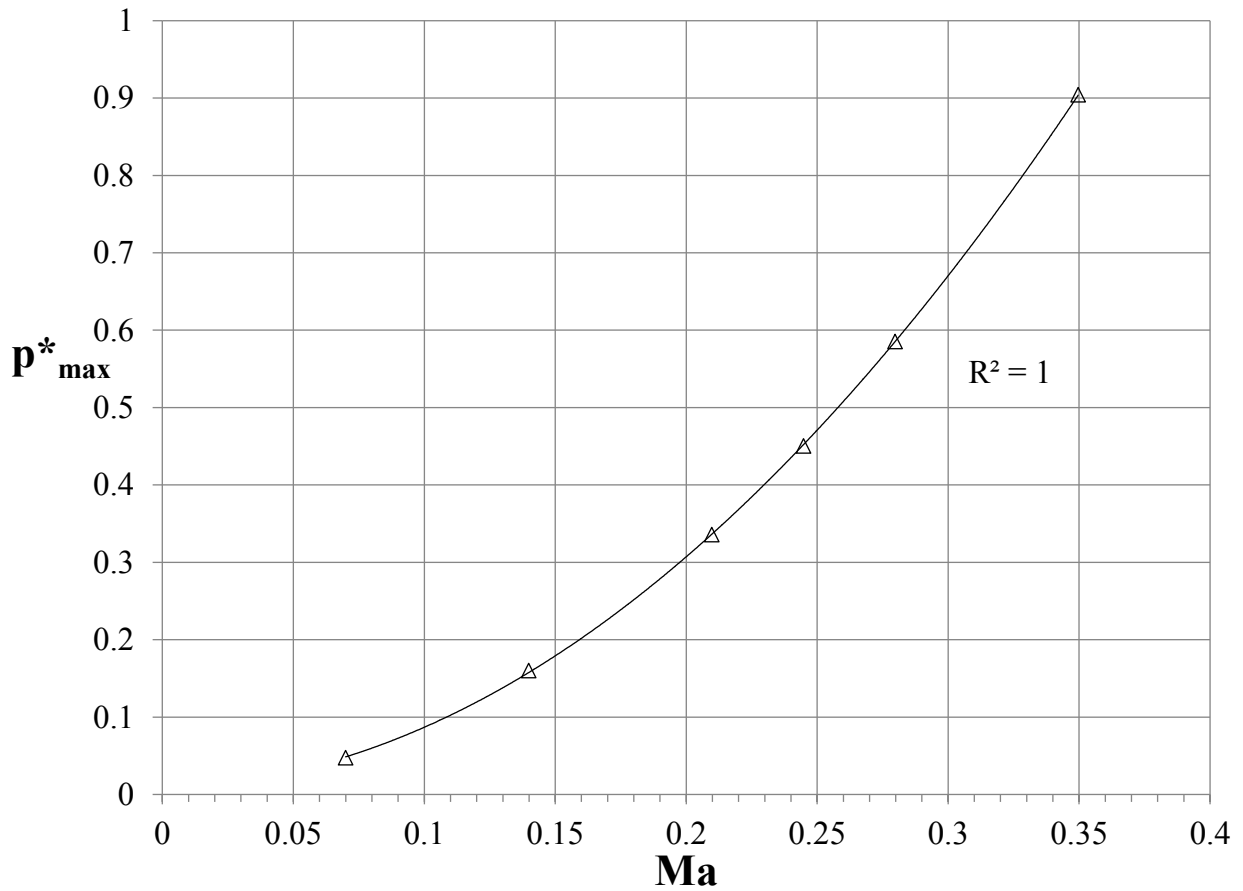


Figure 3-23: Maximum dimensionless pressure versus Mach number,  $h/D=0.2$ ,  $D=500\ \mu\text{m}$ .

### 3.3 Finite Element Model of an elastic solid substrate

In order to model the solid response to the impact force due to the droplet impingement, a typical case for LIE application, i.e. a droplet with a diameter of 500  $\mu\text{m}$  impinged at a velocity of 350 m/s is considered. The spatial pressure history is extracted from the fluid simulation and applied on the solid surface as a boundary condition to obtain the stress field. A flat substrate composed of Ti-6Al-4V material with isotropic behavior is used in the FEM model. Only one quarter of the solid is modeled, due to the symmetry in x-y and x-z planes, and the impact point is located at the center of the substrate. The length, width and height of the computational domain are all equal to 10 mm. Figure 3-24 illustrates the geometry and the grid configuration used for this FEM model. The mesh is refined around the impact point to resolve the stress in the solid more accurately. The total number of nodes for this mesh configuration is 32,360 and the total number of hexahedral elements is 7,220.

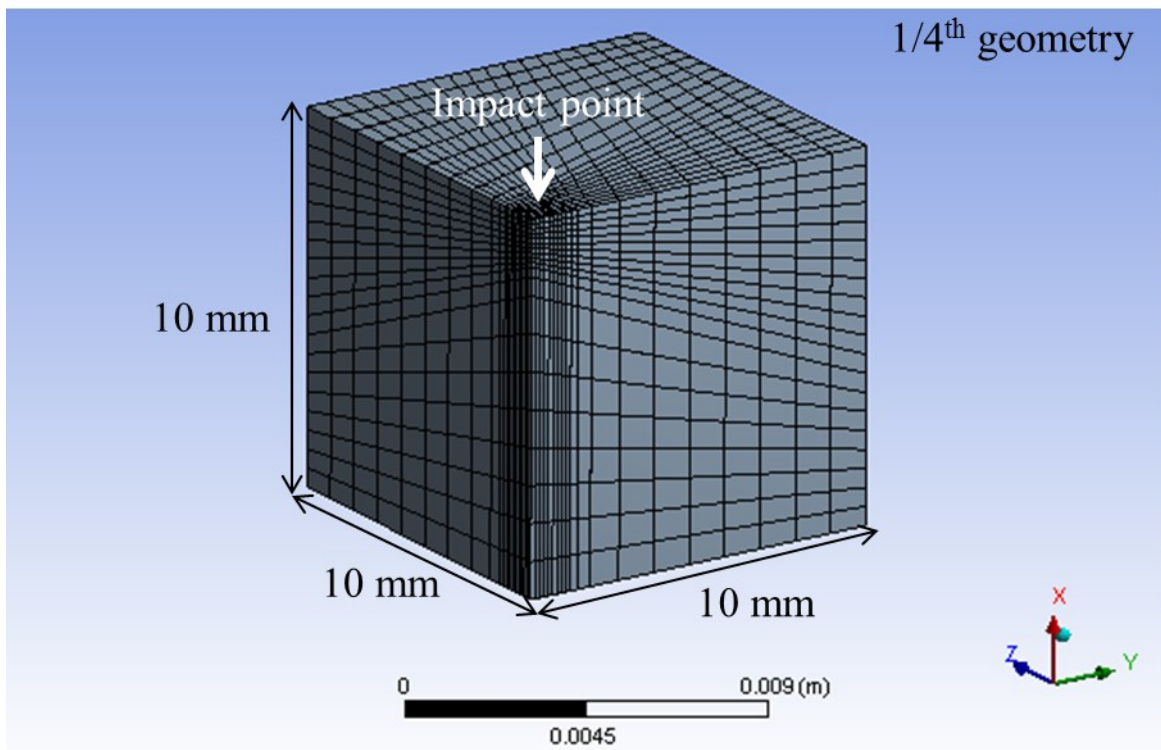


Figure 3-24: FEM model computational domain and mesh.

The equivalent stress (based on von Mises criterion in 3D), normal stress and XY shear stress are monitored at the impact point and their histories are plotted in figure 3-25 (a), in addition to the maximum substrate deformation to the impinged droplet diameter ratio, presented in figure 3-25 (b). As shown in the figure, the stress reaches its peak value right after the impact. The shear stress has the lowest value equal to 0.13 GPa. It should be mentioned that the experimental data indicate that even low values of shear stress could damage the material, if there are micro-cracks initiated inside the solid. The equivalent stress peak is around 0.5 GPa. However, the normal stress reaches a maximum of 0.93 GPa which is greater than the tensile yield strength for Ti-6Al-4V (equal to 0.88 GPa) and very close to tensile ultimate strength (equal to 0.95 GPa).

The contours of X-normal stress, equivalent stress and XY shear stress on the solid surface are presented in figures 3-26, 3-27 and 3-28, respectively. The X component of the normal stresses is presented in figure 3-26 accompanied by its profile along the axis. The negative values for the normal stress are related to the compressive nature of the impact and the maximum stress (0.93 GPa) is located right at the impact point. In figure 3-26 (b),  $X^*=0$  represents the impact point and the stress is plotted along 1 mm from this point. The equivalent stress contour and its magnitude along the X-axis are presented in figure 3-27. It can be seen that the point where the stress is at its peak (0.5 GPa) is located around 125  $\mu\text{m}$  below the impact point. This is considered a high stress concentration point that could possibly lead to micro-crack initiation. The magnitude of the equivalent stress in the solid diminishes farther from this point.

A similar contour is presented for XY shear stress in figure 3-28. It reveals that the region, where high shear stress concentration is observed, is located approximately 500  $\mu\text{m}$  away from the impact point and 100  $\mu\text{m}$  beneath the surface. This region signifies the second potential

location for initiation of micro-cracks. As it was displayed in Figure 1-10, the craters that are formed via consecutive impacts of water droplets have an average radius equal to the droplet diameter. The radial location where the maximum shear stress appears, i.e. 500  $\mu\text{m}$ , could explain the size of those craters, given that the droplets are impinged almost at the same point on the substrate.

Finally, the maximum deflection of the impact point and the displacement of the solid are presented in figure 3-29 (a) and (b), respectively. The negative values imply that the deflection direction is along the imposed pressure direction (negative X). The maximum deformation (minimum displacement) of the impact point is around  $\delta/D=0.007$  (3.5  $\mu\text{m}$ ). This small deformation justifies the initial assumption of a rigid solid by decoupling the fluid and solid equations. As a result, a much higher grid resolution could be applied to the region close to the impingement point in the fluid domain to resolve the flow features better. The output from the compressible fluid solver is then utilized as the boundary condition on the substrate to obtain the transient stresses in the solid domain. This would result in tremendous gain in the total computational time as the FEM model does not require the same grid refinement as the FVM model.

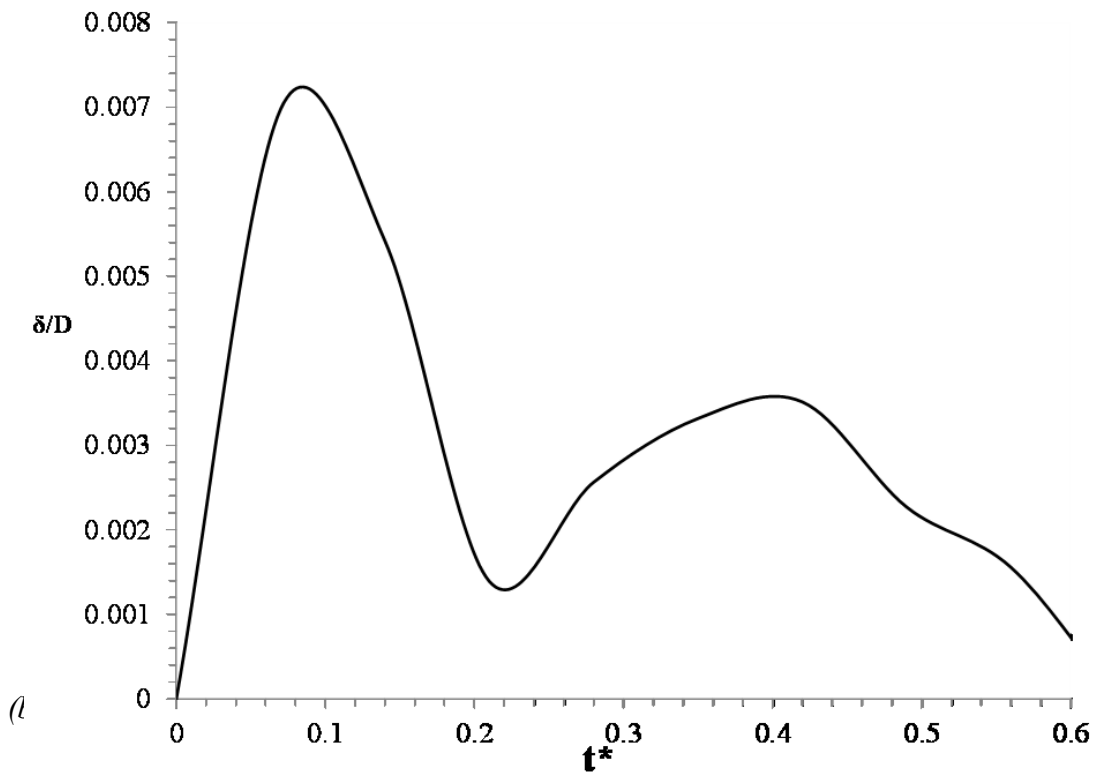
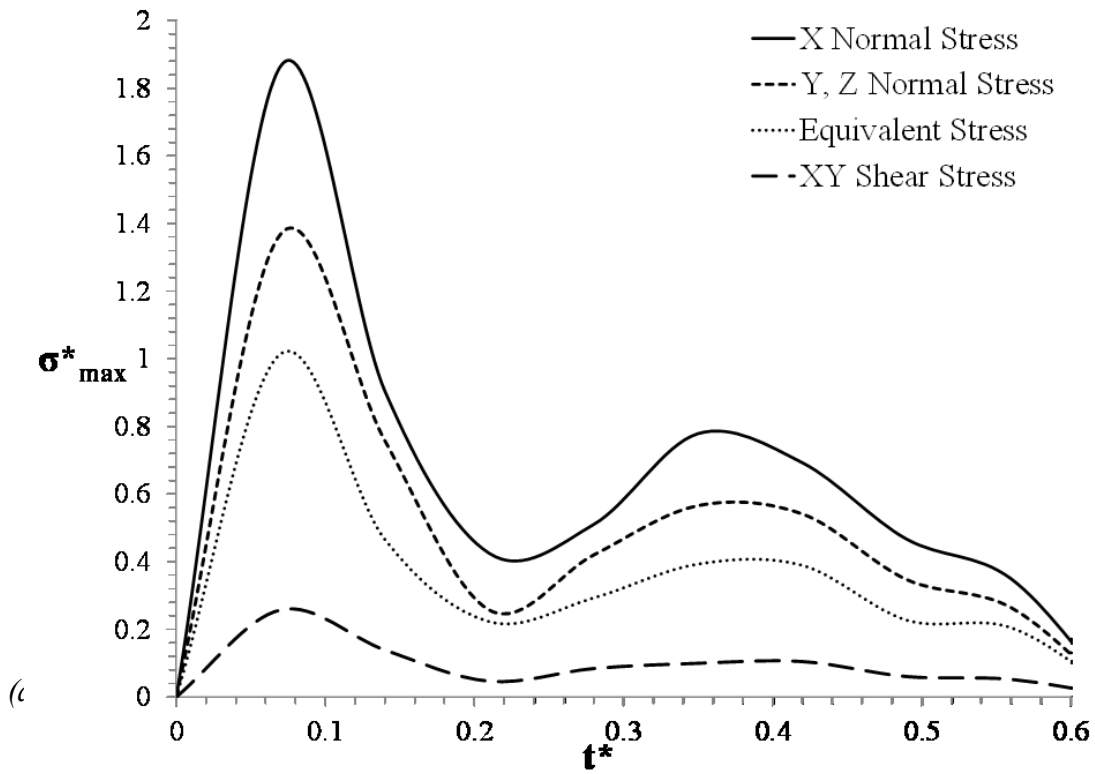


Figure 3-25: (a) Maximum dimensionless stress magnitude comparison, (b) maximum deformation to droplet diameter ratio, at the impact point.

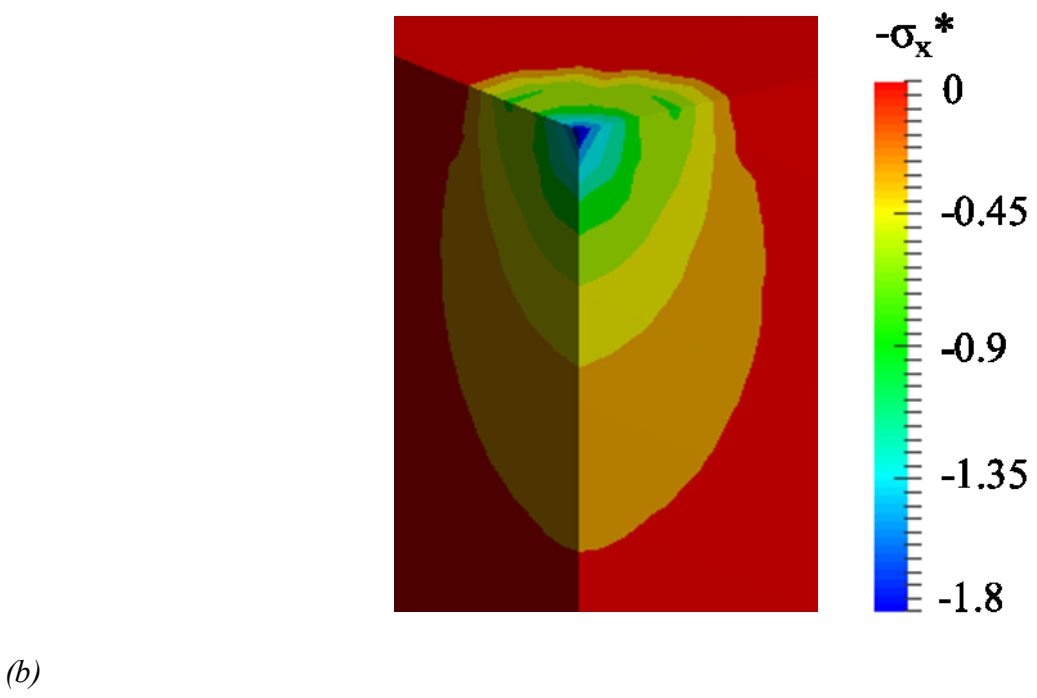
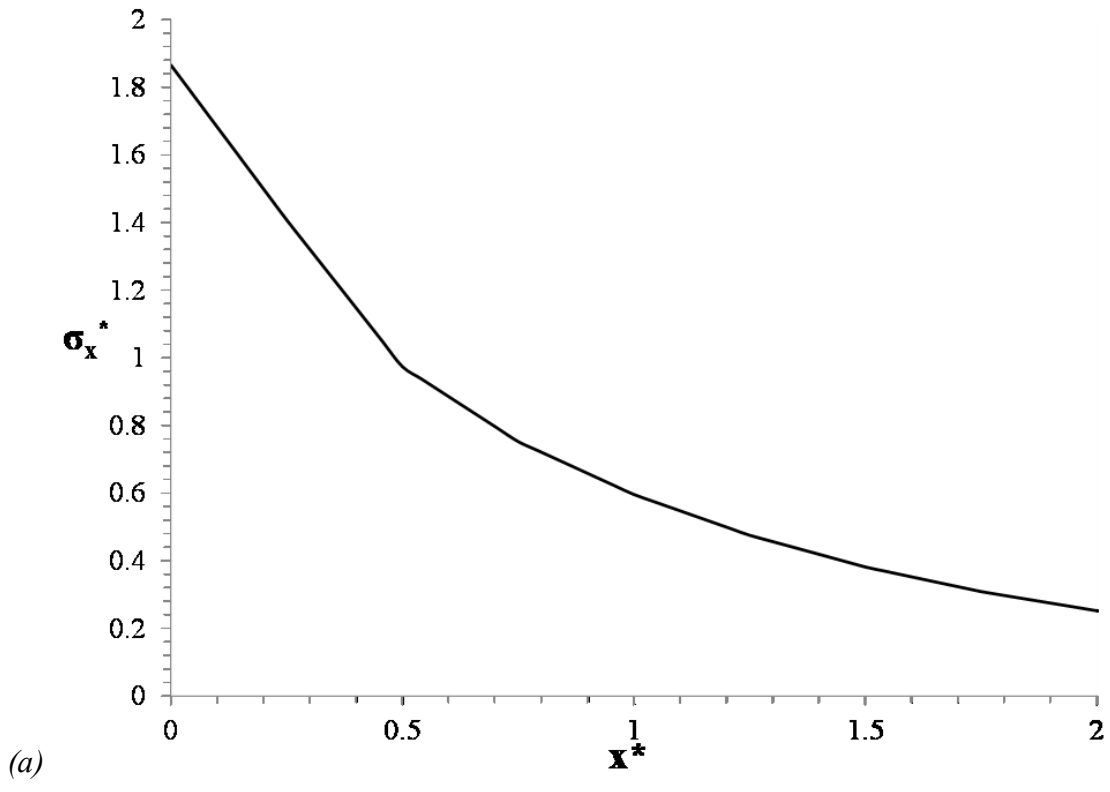


Figure 3-26: X-Normal stress, (a) magnitude along center axis, (b) contour.

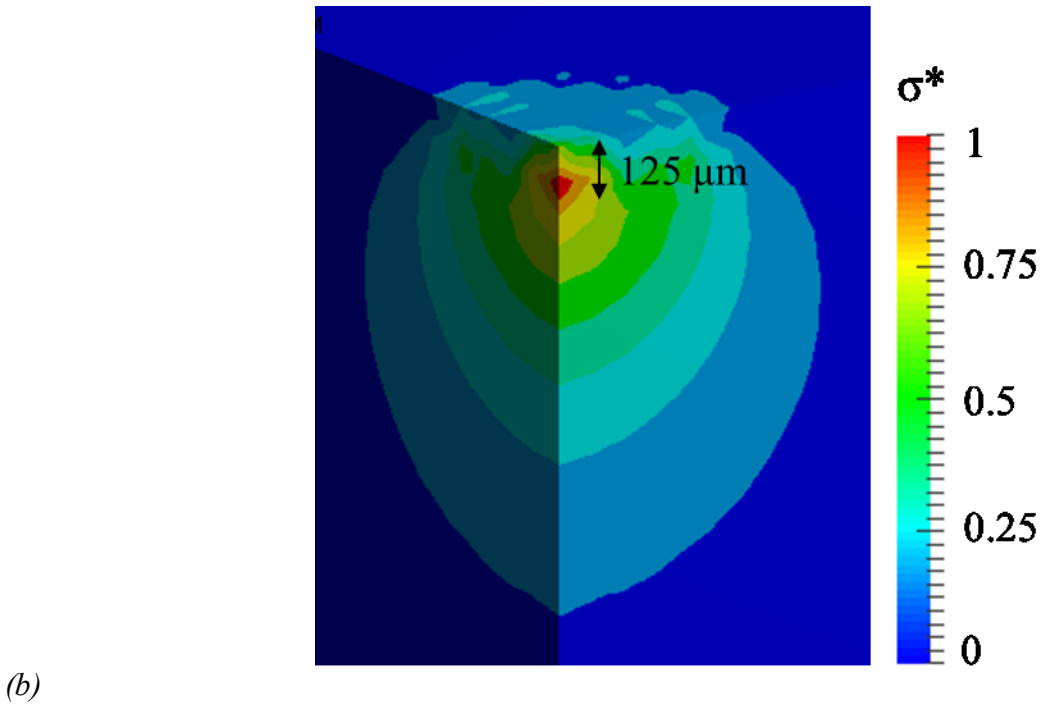
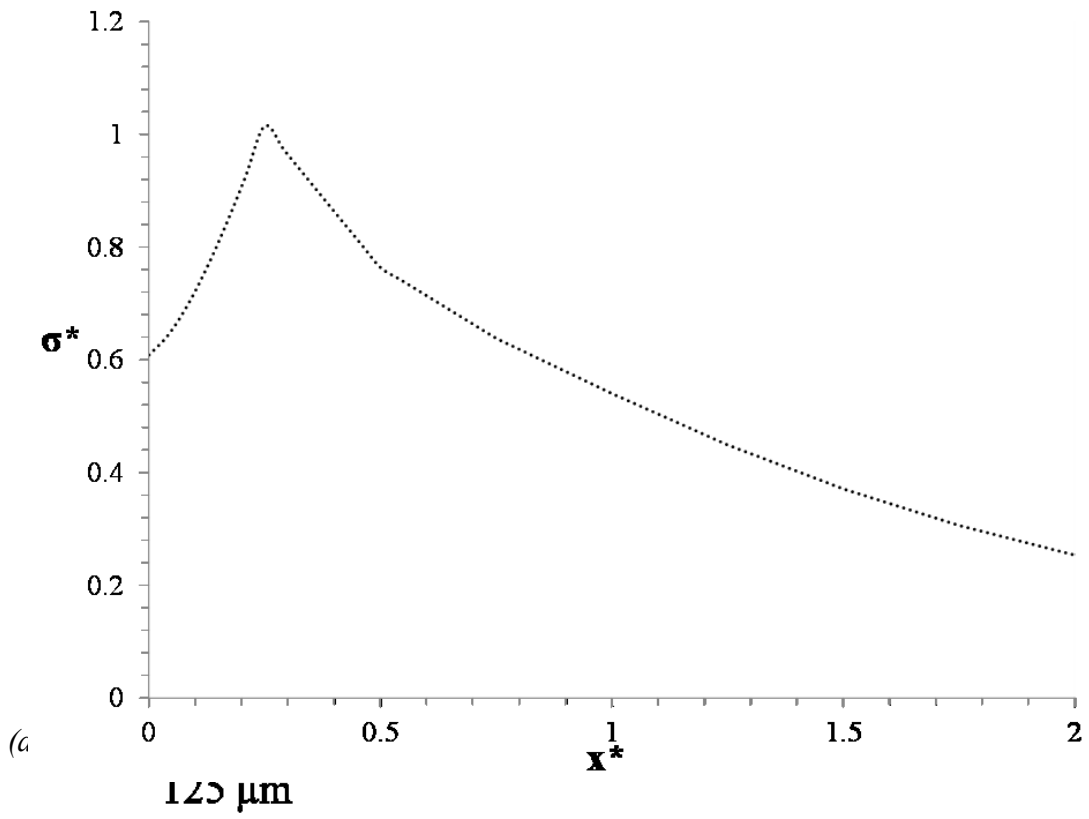
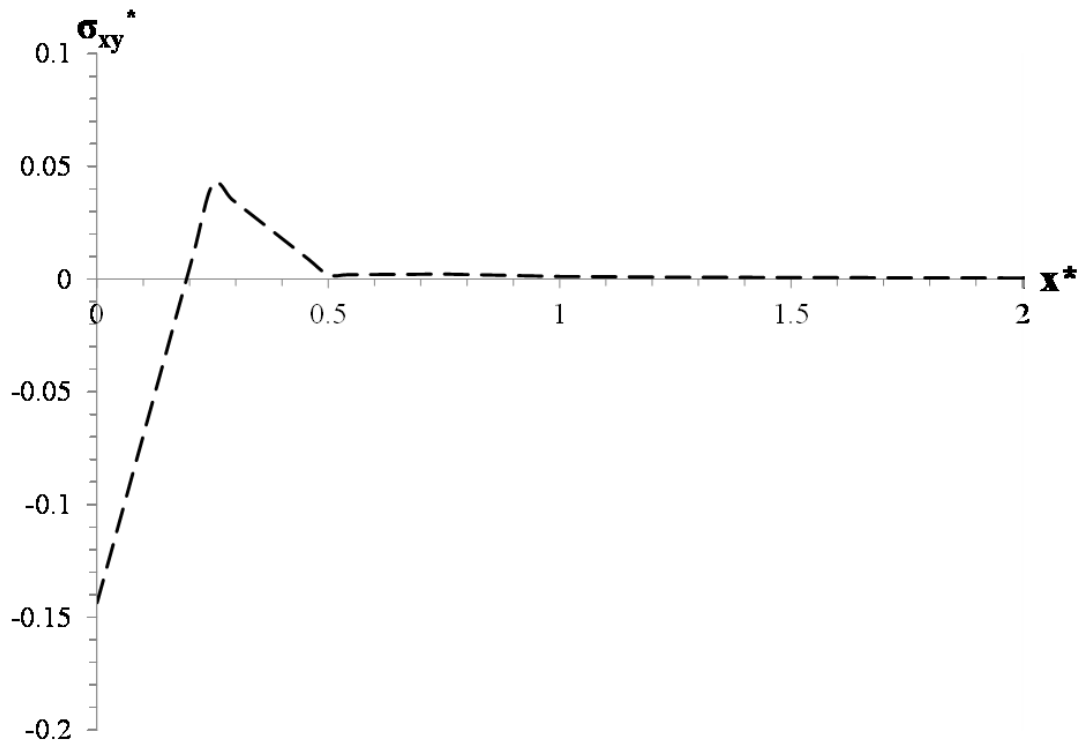
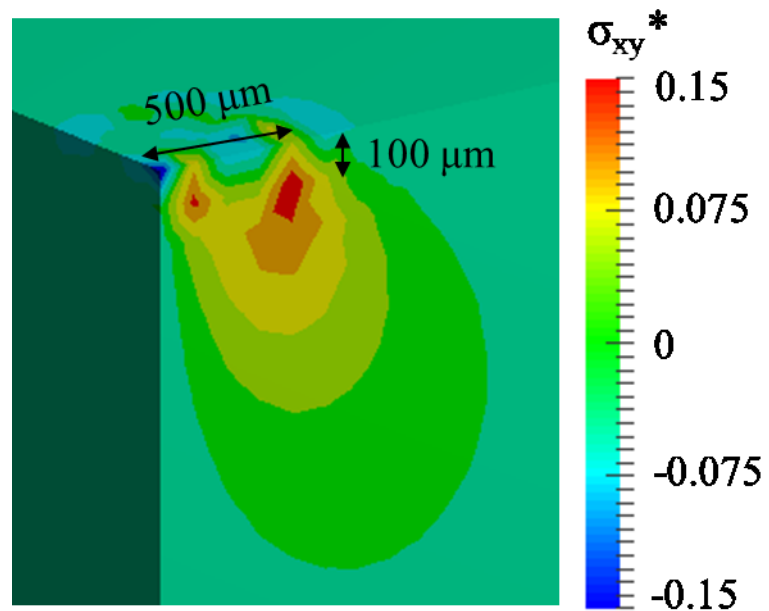


Figure 3-27: Equivalent stress, (a) magnitude along center axis, (b) contour.



(a)



(b)

Figure 3-28: XY shear stress, (a) magnitude along center axis, (b) contour.

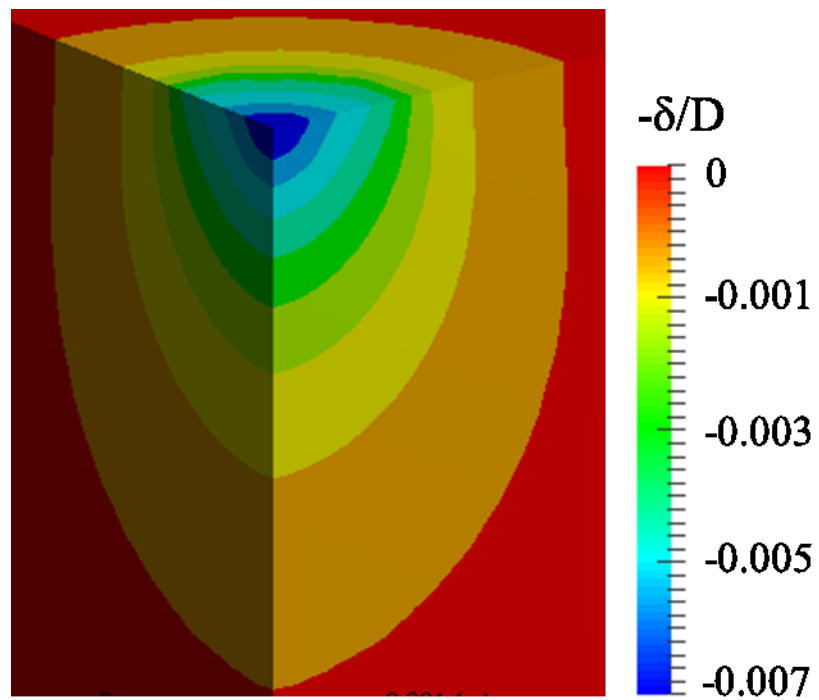
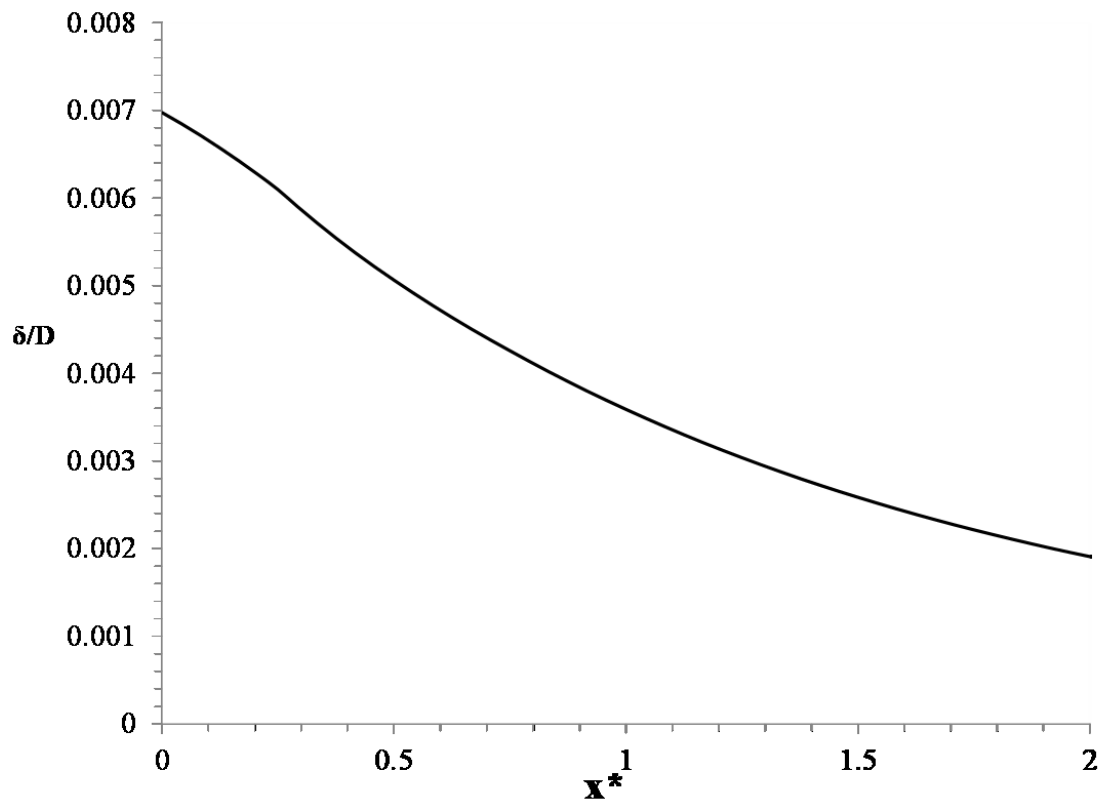


Figure 3-29: Substrate deformation to droplet diameter ratio (a) along center axis, (b) contour.

# 4. Closure

## 4.1 Summary

In summary, a novel 3D FSI model was implemented in the current work using two-way and one-way coupling approaches. In the two-way coupling approach, the fluid and solid equations were solved together, in order to obtain the liquid pressure and solid stress simultaneously. The solid substrate was considered to be elastic when coupled with the incompressible solver at low impingement velocities, i.e. below 100 m/s. For these range of velocities, the transient pressure in the fluid and stress in the solid were captured precisely.

In the one-way coupling approach, fluid and solid equations were decoupled from each other and the solid was considered to be rigid, i.e. negligible substrate deformation. The droplet deformation upon the impact was captured precisely. Next, the obtained pressure was used as a boundary condition and imposed on the elastic substrate to solve the stress field. In this regard, the droplet impact was modeled by an incompressible solver for velocities below 100 m/s.

On the other hand, the impact of the droplet onto a rigid substrate was modeled utilizing a compressible solver for impact velocities between 100 and 500 m/s. The droplet size variations from 200 to 1000  $\mu\text{m}$  were also included in the numerical simulations. The effect of the impact angle on the generated pressure was investigated. Furthermore, the pressure build-up upon the impact of a single droplet onto liquid films with thicknesses from 10 to 200  $\mu\text{m}$  was modeled. Finally, a commercial FEM software, namely ANSYS Workbench, was utilized to showcase the application of the results obtained from the present work in modeling the transient stresses in a Ti-6Al-4V substrate, which is widely used in manufacturing turbine and compressor blades.

## 4.2 Conclusions

The conclusions from the present study are as follows,

1. The solid response to the pressure history is consistent with the pressure distribution at loading and unloading stages of the impact. The peak transient stress appeared shortly after the impact. This is called the loading stage, during which the stress increases rapidly, and is followed by an unloading stage, during which the fluid pressure and solid stress diminish gradually.
2. Investigation of the solid elasticity has shown that the deviation of the maximum pressure on the substrate is less than 6%. Therefore, the solid was assumed to be rigid in order to decouple the fluid and solid equations and solve them in a segregated manner. This assumption resulted in a considerable gain in the computational time.
3. The results have shown that the fluid compressibility plays a major role in modeling the pressure history and the subsequent stress in the solid. In this regard, the comparison carried out between the two models, at an impingement velocity of 100 m/s, revealed that the peak transient stress in the solid predicted by the compressible solver is 45% higher than the one calculated by the incompressible solver. Therefore, using a compressible solver is required to model the impact for velocities above 100 m/s.
4. The variation of maximum generated pressure versus the Mach number was studied and a new linear correlation for the range of the impingement velocities between 100-500 m/s was developed, i.e. equation (3-12). On the other hand, it was shown that the dependence of the impact pressure on the droplet diameter has no particular pattern and it has to be studied on a case-by-case basis. Nonetheless, the deviation from Heymann's correlation [19] for a 1000- $\mu\text{m}$  droplet is less than 7%.

5. The influence of impingement angle was studied for 500- $\mu\text{m}$  droplet impinged at 350 m/s. It was illustrated that the utilization of Heymann's linear equation [19], by replacing the impact velocity with the normal velocity component, results in overestimating the maximum impact pressure by up to 25%, for an impingement angle of 30 degrees.
6. The study of the single droplet impact onto a liquid film has shown that the maximum generated pressure on the solid is reduced exponentially with increasing the film thickness, as the liquid film partially absorbs the impact force. Furthermore, due to reflection of the compression waves on the liquid surface as expansion waves and their cancellation effect, low pressure stripes are observed inside the liquid. Two correlations were obtained, equations (3-13) and (3-14), from a parametric study based on film thickness and impingement velocity, respectively.
7. The results obtained from FEM modeling of isotropic Ti-6Al-4V substrate, under an impact of a 500- $\mu\text{m}$  droplet impinged at 350 m/s, revealed that the X-normal stress magnitude can increase up to the material ultimate strength limit, even though the equivalent stress magnitude stays lower than the yield strength threshold. The maximum normal stress occurred at the solid surface, however, the equivalent stress peak appeared at 125  $\mu\text{m}$  below the surface along the droplet centerline, where initiation of micro-cracks was observed in the experiments. The high magnitude of the compressive stress can become very destructive if the impacts occur repetitively. The magnitude of the peak transient stress is of high importance, as it may reach a critical value and cause severe damages in the solid. The solid deformation, predicted by the numerical modeling, showed a maximum of 3.5  $\mu\text{m}$ . This deformation may lead to the formation of craters on the solid surface and eventually cause material spall-off from the solid.

### **4.3 Challenges and limitations**

The major challenge in the present study was the coupling between the fluid and solid solvers. The one-way coupling was achieved for both incompressible and compressible FSI solvers. However, the two-way coupling approach was only implemented in the incompressible FSI solver. The development of a two-way coupled compressible FSI solver was out of the scope of the current work.

Moreover, the parallelization of the FSI solver is very challenging due to the separate partitioning of the fluid and solid domains and building the communication interface between the two domains. Hence, the FSI solver had to be executed on a single processor, which increased the computational time considerably. In order to mitigate this limitation, the fluid and solid equations were decoupled for high impingement velocities. This method allowed to achieve a very high grid resolution in the fluid domain to capture the details of the impact, while reducing the overall computational cost substantially, without compromising the accuracy of the transient stresses in the solid substrate.

#### 4.4 Future work

The recommendations for future studies based on the present work are as follows,

- the immediate step after this study is to implement the two-way coupling mechanism between the compressible fluid solver and FEM solver, in order to expand the range of applications for this model.
- modeling the single impact of a 200- $\mu\text{m}$  droplet impinged at 350m/s velocity demonstrated a maximum pressure of  $p^*=3.5$  (1.75 GPa), which is higher than all other droplet sizes with the same impact velocity. This could be due to the influence of the pressure front geometry close to the impact point, which is dependent on the initial droplet size. Further analysis with finer grid sizes is required to capture the air entrapment details for this droplet size and study its effect on the pressure history in the compressed region.
- the cavitation due to the vaporization of water at the droplet edge attached to the solid can be numerically modeled by adding the phase change equations to the solver.
- the oblique impacts of single droplets onto liquid films have not been considered and can be studied in the future.
- impact of multiple droplets onto each other or liquid films can be analyzed with the current model.
- the simulations for additional film thickness to droplet diameter ( $h/D$ ) ratios at various impingement velocities can be carried out to extend the range of equation (3-14).
- finally, the output for the pressure spatial history can be used in a fatigue model to determine the material life cycle under various impingement conditions for compressor or turbine blades with different geometries.

# Bibliography

- [1] M. Mahdipoor, D. Kevorkova, P. Jedrzejowski and M. Medraj, "Water droplet erosion mechanism of nearly fully-lamellar gamma," *Materials and Design*, vol. 89, p. 1095–1106, 2016.
- [2] Q. Zhou, N. Li, X. Chen, T. Xu, S. Hui and D. Zhang, "Liquid drop impact on solid surface with application to water drop erosion on turbine blades, Part II: Axisymmetric solution and erosion analysis," *International Journal of Mechanical Sciences*, vol. 50, pp. 1543-1558, 2008.
- [3] E. Honegger, "Test on Erosion caused by Jets," *Brown Boveri Review*, vol. 14, pp. 95-104, 1927.
- [4] H. W. Bargmann, "The Mechanics of Erosion by Liquid and Solid Impact," *International Journal of Solid Structure*, vol. 29, no. 1415, pp. 1685-1698, 1992.
- [5] H. Kirols, M. S. Mahdipoor, D. Kevorkov and M. Medraj, "Water Droplet Impingement Erosion: Testing, Mechanisms and Improved Representation," in *XXIV ICTAM*, Montreal, 2016.
- [6] N. Li, Q. Zhou, X. Chen, T. Xu, S. Hui and D. Zhang, "Liquid drop impact on solid surface with application to water drop erosion on turbine blades, Part I: Nonlinear wave model and solution of one-dimensional impact," *International Journal of Mechanical Sciences*, vol. 50, pp. 1526-1542, 2008.
- [7] G. S. Springer, *Erosion by liquid impact*, Washington DC: Scripta Publishing

Company, Wiley, 1976.

- [8] N. Kamkar, F. Bridier, P. Bocher and P. Jedrzejowski, "Water droplet erosion mechanisms in rolled Ti–6Al–4V," *Wear*, vol. 301, p. 442–448, 2013.
- [9] A. Worthington, "On the forms assumed by drops of liquids falling vertically on a horizontal plate," in *Proceedings of the Royal Society of London*, 1876.
- [10] J. Fukai, Y. Shiiba, T. Yamamoto, O. Miyatake and D. Pouli, "Wetting effects on the spreading of a liquid droplet colliding with a flat surface: experiment and modeling," *Physics of Fluids*, vol. 7, no. 2, pp. 236-247, 1995.
- [11] Chandra S. and C. T. Avedisian, "On the Collision of a Droplet with a Solid Surface," *Proceedings of the Royal Society*, vol. 432, no. 1884, 1991.
- [12] M. Pasandideh-Fard, . Y. M. Qiao, S. Chandra and J. Mostaghimi, "Capillary effects during droplet impact on a solid surface," *Physics of Fluids*, vol. 8, no. 3, 1996.
- [13] I. V. Roisman, R. Rioboo and C. Tropea, "Normal impact of a liquid drop on a dry surface: model for spreading and receding," *Proceedings of the Royal Society*, vol. 458, no. 2022, 2002.
- [14] V. Mehdi-Nejad, J. Mostaghimi and S. Chandra, "Air bubble entrapment under an impacting droplet," *Physics of fluids*, vol. 15, no. 1, pp. 173-183, 2003.
- [15] N. Z. Mehdizadeh, S. Chandra and J. Mostaghimi, "Formation of fingers around the edges of a drop hitting a metal plate with high velocity," *Journal of Fluid Mechanics*, vol. 510, pp. 353-373, 2004.
- [16] T. D. Blake and J. De Conick, "The influence of solid–liquid interactions on dynamic wetting," *Advances in Colloid and Interface Science*, vol. 96, no. 1-3, pp. 21-36, 200.

- [17] J. C. Bird, R. Dhiman, H. M. Kwon and K. Varanasi, "Reducing the contact time of a bouncing drop," *Nature*, vol. 503, p. 385–388, 2013.
- [18] M. Damak, S. R. Mahmoudi, M. N. Hyder and K. Varanasi, "Enhancing droplet deposition through in-situ precipitation," *Nature*, 2016.
- [19] F. J. Heymann, "High-speed impact between a liquid drop and a solid surface," *Journal of Applied Physics*, vol. 40, pp. 5113-22, 1969.
- [20] J. P. Dear and J. E. Field, "High-speed photography of surface geometry effects in liquid/solid impact," *Journal of Applied Physics*, vol. 63, pp. 1015-21, 1988.
- [21] J. E. Field, J. P. Dear and J. E. Ogren, "The Effects of Target Compliance on Liquid Drop Impact," *Journal of Applied Physics*, vol. 65, pp. 533-40, 1989.
- [22] M. C. Rochester and J. H. Brunton, "Erosion by Liquid and Solid Impact," in *International Conference on Erosion by Liquid and Solid Impact (5th)*, Cambridge, 1979.
- [23] M. B. Lesser, "Analytic Solutions of Liquid-Drop Impact Problems," *Proceedings of the Royal Society A*, vol. 377, no. 1770, pp. 289-308, 1981.
- [24] M. B. Lesser and J. E. Field, "The Impact of Compressible Liquids," *Annual Review of Fluid Mechanics*, vol. 15, pp. 97-122, 1983.
- [25] K. Haller, "High-Velocity Impact of a Liquid Droplet on a Rigid Surface: The Effect of Liquid Compressibility," Swiss Federal Institute of Technology, Zurich, 1972.
- [26] H. Shih, "The theoretical investigation and experimental research on the water drop impact destroy of blades in the wet steam turbine stage," Xi'an Jiaotong University, Xi'an, China, 1989.
- [27] S. S. Cook, "Erosion by Water Hammer," *Proceeding of the Royal Society*, vol. 119, pp.

- 481-8, 1928.
- [28] O. G. Engel, "Waterdrop Collisions with Solid Surface," *Journal of Research of the National Bureau of Standards*, vol. 54, 1955.
- [29] R. M. Blowers, "On the Response of an Elastic Solid to Droplet Impact," *International Journal of the Institute of Mathematics and Its Applications*, vol. 5, pp. 167-193, 1969.
- [30] W. F. Adler and D. J. Mihora, "Analysis of Water Drop Impacts on Layered Window Constructions," *Proceedings of the SPIE 2286*, pp. 264-274, 1994.
- [31] K. K. Haller, Y. Ventikos, D. Poulidakos and P. Monkewitz, "Computational Study of High-speed Liquid Droplet Impact," *Journal of Applied Physics*, vol. 92, pp. 2821-8, 2002.
- [32] Y. C. Huang, F. G. Hammitt and W. J. Yang, "Hydrodynamic phenomena during high-speed collision between liquid droplet and rigid plane," *Journal of Fluids Engineering*, vol. 95, pp. 276-294, 1973.
- [33] X. Chen, M. Y. He, I. Spitsberg, N. A. Fleck, J. W. Hutchinson and A. G. Evans, "Mechanisms governing the high temperature erosion of thermal barrier coatings used in gas turbines," *Wear*, vol. 256, pp. 735-746, 2004.
- [34] H. S. Kim, J. S. Kim, H. J. Kang and S. R. Kim, "Stress Wave Propagation in a Coated Elastic half-space due to Water Drop Impact," *Journal of Applied Mechanics*, vol. 68, pp. 346-8, 2001.
- [35] M. K. Lee, W. W. Kim, C. K. Rhee and W. J. Lee, "Ananalysis of stress waves in 12Cr steel, Stellite 6B and TiN by liquid impact loading," *Nuclear Engineering and Design*, vol. 214, pp. 183-193, 2002.
- [36] K. K. Haller, D. Poulidakos, Y. Ventikos and P. Monkewitz, "Shock wave formation in

- droplet impact on a rigid surface: lateral liquid motion and multiple wave structure in the contact line region," *Journal of Fluid Mechanics*, vol. 490, pp. 1-14, 2003.
- [37] R. Li, H. Ninokata and M. Mori, "A numerical study of impact force caused by liquid droplet impingement onto a rigid wall," *Progress in Nuclear Energy*, vol. 53, pp. 881-885, 2011.
- [38] J. U. Brackbill, D. B. Kothe and C. Zemach, "A continuum method for modelling surface tension," *Journal of Computational Physics*, vol. 100, no. 2, p. 335–354, 1992.
- [39] C. Hirt and B. Nichols , "Volume of Fluid (VOF) Method for the Dynamics of Free Boundaries," *Journal of Computational Physics*, vol. 39, no. 1, pp. 201-225, 1981.
- [40] D. L. Youngs, "Time-Dependent Multi-Material Flow with Large Fluid Distortion," *Numerical Methods for Fluid Dynamics*, pp. 273-285, 1982.
- [41] S. Turek and J. Hron, "Proposal for Numerical Benchmarking of Fluid-Structure Interaction between an Elastic Object and Laminar Incompressible Flow," in *Fluid-Structure Interaction*, Springer, 2006.
- [42] P. G. Tait, "Report on some of the physical properties of fresh water and sea water," *Physical Chemistry*, vol. 2, p. 1–17, 1888.

# Appendices

## I. Grid sensitivity analysis

The dependence of the generated pressure on the grid size is investigated. To that end, the impact of a 500- $\mu\text{m}$  droplet at 350 m/s on a rigid substrate was analyzed with three different grid sizes of 1.25, 1 and 0.75  $\mu\text{m}$ . Figure 1 illustrates the dimensionless pressure generated on the substrate, at a time when the maximum pressure appears, obtained from the simulations of the same impact conditions but with three different grid sizes. The peak dimensionless pressures predicted with the grid size of 1.25, 1 and 0.75  $\mu\text{m}$  are 2.2925, 2.2583 and 2.2527, respectively. The difference of the peak pressure values between the simulation with 1 and 0.75  $\mu\text{m}$  grids is less than 0.25%. Therefore, refining the grid size below 1  $\mu\text{m}$  would not affect the accuracy of the generated pressure and this mesh size is selected for simulating the droplet impact.

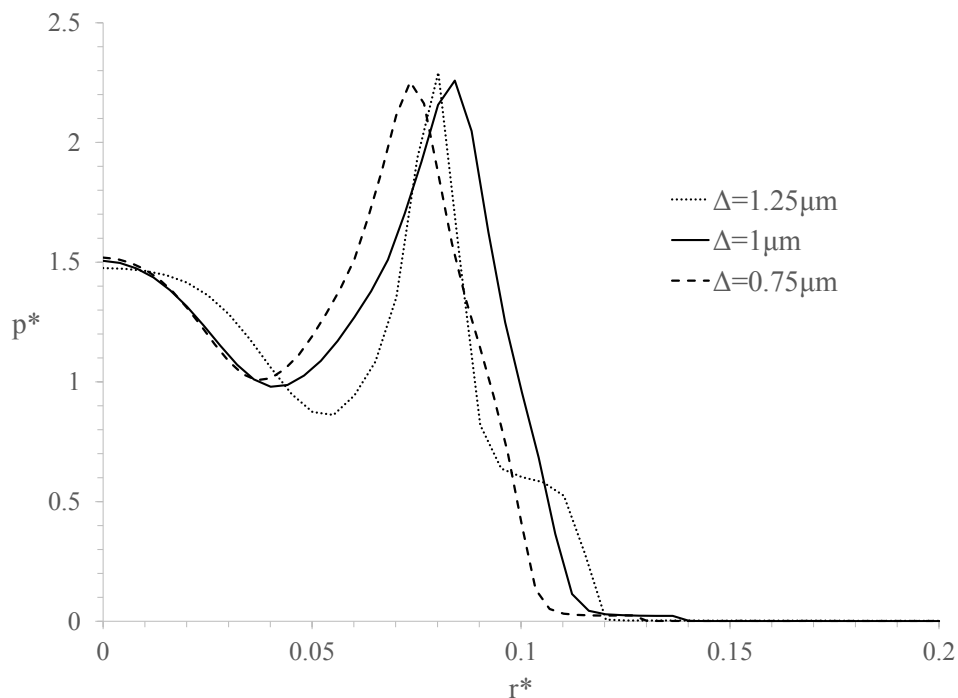


Figure 1: Dimensionless pressure along r-axis modeled with 3 different grid sizes.

## ***II. Droplet impact onto liquid films, extension***

### **Effect of droplet size on generated pressure**

The influence of the droplet size on the maximum pressure generated on the solid substrate have been discussed in section 3.2.1 for normal impacts. In order to examine this effect upon impact on a liquid film, a similar analysis is carried out for the same droplet size of 500  $\mu\text{m}$  impinged at 350 m/s on to liquid films. The film thickness is varied proportionally with respect to the droplet diameter resulting in the same ratio of  $h/D=0.2$ . Figure 2 illustrates the dimensionless maximum pressure versus the droplet diameter between 200 to 1000  $\mu\text{m}$ . As it can be seen from this figure, the pressure variation due to the droplet size is negligible (the standard deviation is less than 1%).

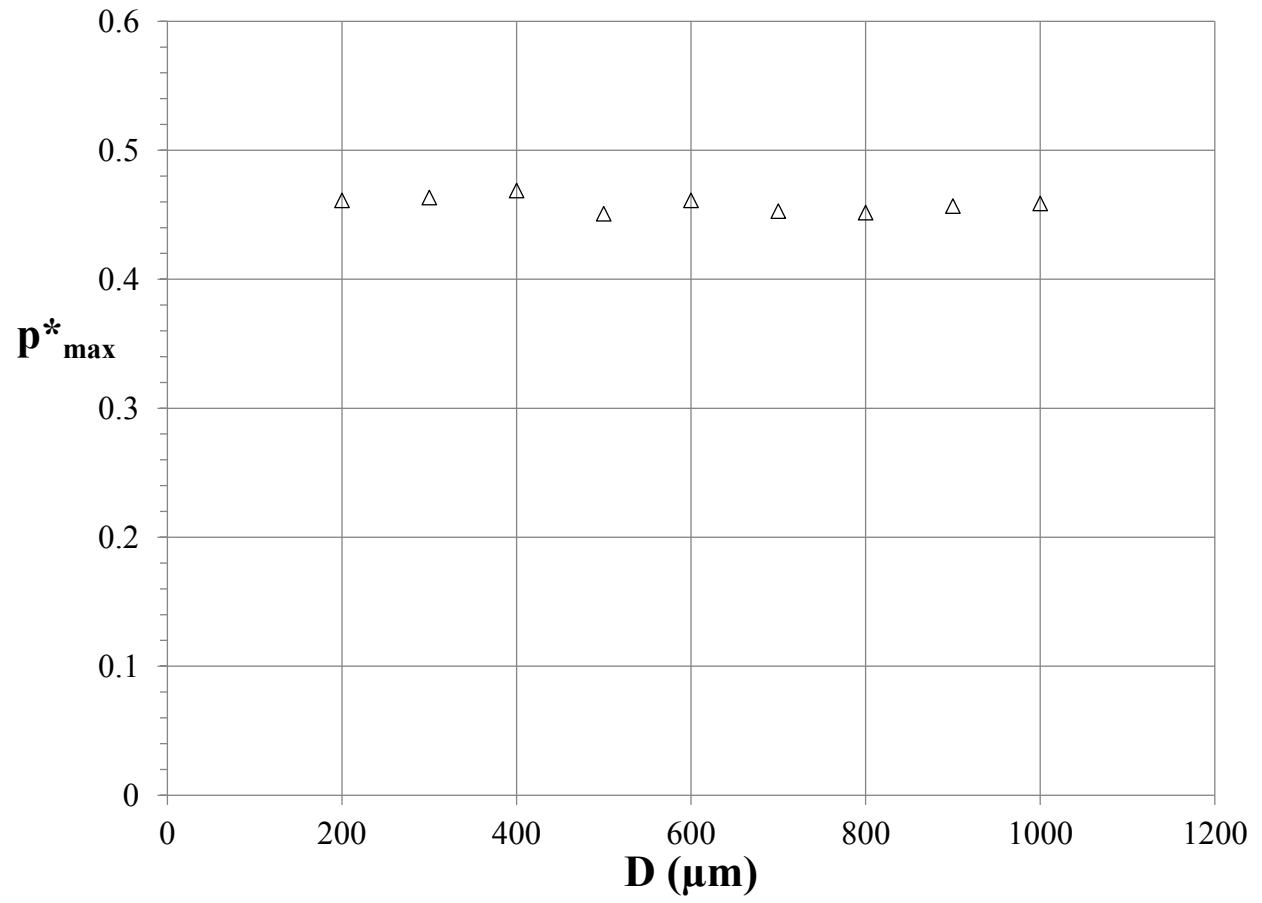


Figure 2: Maximum dimensionless pressure versus droplet diameter,  $h/D=0.2$ ,  $V_0=350$  m/s.

### **Effect of impingement velocity on generated pressure**

The variation of the maximum pressure exerted on the solid surface with the impingement velocity has been discussed for the impact on to a rigid solid and a liquid film in sections 3.2.1 and 3.2.3, respectively. In order to further investigate the dependence of the pressure-Mach number correlation on the film thickness, the impingement of 500- $\mu\text{m}$  droplet at a velocity of 100-500 m/s were repeated, but this time at a film thickness to droplet diameter ratio of  $h/D=0.02$  ( $h=10 \mu\text{m}$ ), instead of  $h/D=0.2$  ( $h=100 \mu\text{m}$ ) presented in section 3.2.3. The maximum dimensionless pressure, calculated over all time steps during the impact, is plotted versus the impingement Mach number in figure 3 along with the corresponding correlation in equation A-1. As it can be inferred from the graph and confirmed by equation (A-1), the variation of the dimensionless pressure is also a quadratic function of the Mach number. Therefore, for the two film thicknesses examined in the present work, namely 10 and 100  $\mu\text{m}$ , a polynomial of degree two can be used to predict the maximum pressure exerted on the solid surface based on the impact Mach number using equations (3-14) and (A-1), respectively. It should be noted that the abovementioned correlations are only valid for a droplet size of 500  $\mu\text{m}$  and a range of Mach numbers between 0.07 and 0.35.

$$p_{\max}^* = 12.473 Ma^2 + 2.4348 Ma - 0.0557, \text{ for } h/D = 0.02 \text{ and } 0.07 \leq Ma \leq 0.35 \quad (\text{A-1})$$

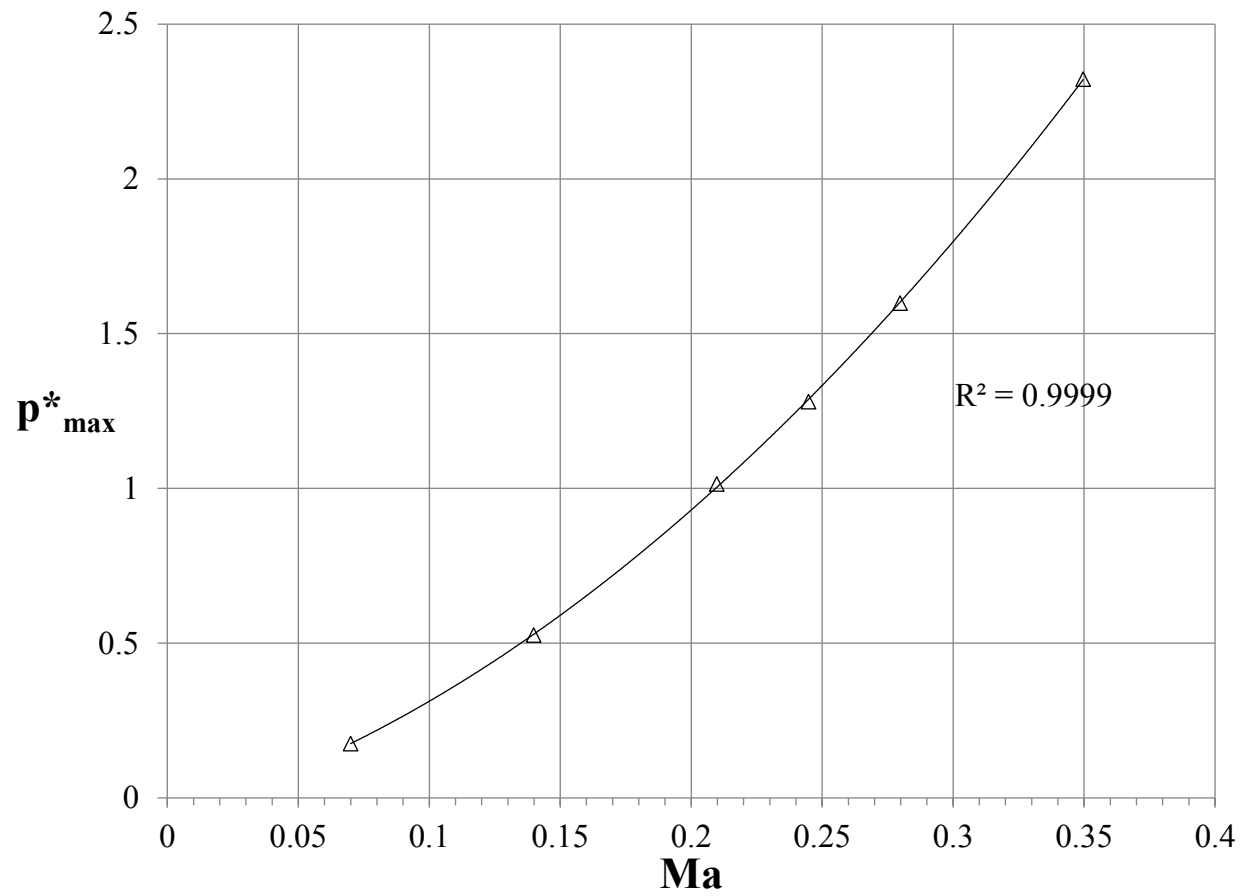


Figure 3: Maximum dimensionless pressure versus Mach number,  $h/D=0.02$ ,  $D=500 \mu\text{m}$ .